PHOTOCHEMISTRY AND PHOTOBIOLOGICAL IMPLICATIONS OF FUNCTIONALIZED FULLERENES IN AQUEOUS SYSTEMS

A Dissertation Presented to
The Academic Faculty

By

Samuel David Snow

In Partial Fulfillment
Of the Requirements for the Degree
Doctorate of Philosophy in Environmental Engineering

Georgia Institute of Technology

August, 2014

Photochemistry and Photobiological Implications of Functionalized Fullerenes in Aqueous Systems

Approved by:

Dr. Jaehong Kim, Advisor
School of Civil and Environmental Engineering
Georgia Institute of Technology

Dr. Seung Soon Jang
School of Materials Science and Engineering
Georgia Institute of Technology

Dr. Ching-Hua Huang
School of Civil and Environmental Engineering
Georgia Institute of Technology

Dr. John Fortner
School of Environmental and Chemical Engineering
Washington University in St. Louis

Dr. Yongshen Chen
School of Civil and Environmental Engineering
Georgia Institute of Technology

Date Approved: May 16th, 2014

Dedication

I would like to dedicate this dissertation to my younger brother, Nathaniel Snow, who suffered a traumatic brain injury in a horrific car accident during the first year of my graduate program, on April 14th, 2010. He is a constant encouragement, a reminder to be joyful always, regardless of situation, and an inspiration to persevere. Above all he is a dear friend and brother, and his life is a precious gift to me and my family.

ACKNOWLEDGEMENTS

I am incredibly grateful for Dr. Jaehong Kim for his friendship, mentorship, and encouragement as my thesis advisor. You always challenged me in the right ways, doing everything to provide every opportunity for me academically and otherwise. I am also very thankful for my committee for their guidance, encouragement, and support.

I am indebted to my family, particularly my parents (Ben and Kathleen), my sister Elya, and my brother Jonathan for their care of Nathaniel and their encouragement to continue pursuing my degree in the midst of tragedy. They always remind me of life outside the pressures of graduate school and are a constant strength and joy in my life.

I would like to thank my loving fiancée, Lily Tyndall, and her family for their prayers, support, and encouragement in this final chapter of my graduate career.

I would like to thank the many friends, who have often been as close as family, throughout my years at Georgia Tech for their support, distractions, and friendships.

I would like to thank Dr. Ellery Ingall for his mentorship and friendship as I began to delve into the realm of scientific research during my undergraduate program.

I would like to thank Dr.s Seung Soon Jang and Ki Chul Kim for their collaboration on the molecular modeling. I would like to thank Dr. Min Cho for his guidance and wisdom for conducting photochemical research and Dr. Jaesang Lee for his assistance with the laser flash photolysis experiments. I am also grateful for Dr. Jim Millett for his assistance with transmission electron microscopy imaging.

I am grateful for funding from the National Science Foundation for this work.

TABLE OF CONTENTS

LIST OF TABLES

LIST OF FIGURES

NOMENCLATURE

$^1O_2$	Singlet oxygen
Å	Angstrom (10^{-10} m)
A1	Mono-functionalized fulleropyrrolidine
A2	Bis-functionalized fulleropyrrolidine
A3	Tris-functionalized fulleropyrrolidine
AB	Acid-base
AFM	Atomic force microscopy
ATCC	American Type Culture Collection
ATR-FTIR	Attenuated total reflectance - Fourier transform infrared
B1	Mono-functionalized fulleropyrrolidinium ion
B2	Bis-functionalized fulleropyrrolidinium ion
B3	Tris-functionalized fulleropyrrolidinium ion
BE	Binding Energy
BET	Back electron transfer
BLB	Black light blue
C1	Phenyl-C_{61}-butyric acid methyl ester
C2	Phenyl-C_{62}-butyric acid methyl ester
C3	Phenyl-C_{63}-butyric acid methyl ester
CCD	Charge coupled device
CT	Concentration × time
DFT	Density Functional Theory
DLS	Dynamic light scattering
DLVO	Derjaguin and Landau, Verwey and Overbeek
DMA	Dimethylaniline
DMSO	Dimetheyl sulfoxide
E. coli	*Escherichia coli*
EDS	Energy-dispersive spectroscopy
EPA	Environmental Protection Agency
FFA	Furfuryl alcohol
FL	Fluorescent lamp
FWHM	Full-width at half maximum
GGA	Generalized gradient approximation
IR	Infrared
ISC	Intersystem crossing
kDa	kilo Dalton
LAMMPS	Large-scale atomic/molecular massively parallel simulator
LFP	Laser flash photolysis
LW	Lifshitz-van der Waals
MALDI-MS	Matrix assisted laser desorption ionization - mass spectrometry
MD	Molecular dynamics
MIC	Minimum inhibitory concentration

nA1	Aggregates of mono-functionalized fulleropyrrolidine
nA2	Aggregates of bis-functionalized fulleropyrrolidine
nA3	Aggregates of tris-functionalized fulleropyrrolidine
nB1	Aggregates of mono-functionalized fulleropyrrolidinium ion
nB2	Aggregates of bis-functionalized fulleropyrrolidinium ion
nB3	Aggregates of tris-functionalized fulleropyrrolidinium ion
NBT^{2+}	Nitro blue tetrazolium
nC1	Aggregates of phenyl-C_{61}-butyric acid methyl ester
nC2	Aggregates of phenyl-C_{62}-butyric acid methyl ester
nC3	Aggregates of phenyl-C_{63}-butyric acid methyl ester
nC_{60}	C_{60} aggregates
NMR	Nuclear magnetic resonance
NOM	Natural organic matter
NPT	Isorthermal-isobaric condition
NVT	The canonical ensemble
$O_2{\cdot}^-$	Superoxide radical anion
OD_{600}	Optical density at 600 nm
OPV	Organic photovoltaics
PALS	Phase analysis light scattering
PBS	Phosphate buffered solution
PCBM	Phenyl-C_{61}-butyric acid methyl ester (also termed as C1)
PMN	Pre-manufacturing notice
PPPM	Particle–particle particle–mesh
QM	Quantum mechanical
QSAR	Quantitative structure-activity relationship
RB	Rose Bengal
ROS	Reactive oxygen species
SOD	Superoxide dismutase
SODIS	Solar disinfection
t-BuOH	tert-butyl alcohol
TEM	Transmission electron microscopy
THF	Tetrahydrofuran
THG	Third harmonic generation
THG	Third harmonic generation
TOC	Total organic carbon
TTA	Triplet-triplet annihilation
UV	Ultraviolet
UV/Vis	Ultraviolet and visible light
VASP	Vienna *ab initio* simulation package
XPS	X-ray photoelectron spectroscopy
XTT	(2,3-bis(2-methoxy-4-nitro-5-sulfophenyl)-2*H*-tetrazolium-5-carboxanilide salt)
ζ	Zeta (as in ζ-potential)

SUMMARY

Fullerenes have been the focus of significant research effort and curiosity for their unique physicochemical and photochemical properties since their discovery almost 30 years ago. C_{60} fullerene in particular has received tremendous attention, due to its prevalence in fullerene production and chemical stability. While ambitious prospective applications for C_{60} have been ubiquitous, the extremely hydrophobic nature of fullerenes and consequent aggregation at the nano scale has hampered many endeavors. Researchers, therefore, have turned their attention to the functionalization of fullerenes to add hydrophilic moieties for applications in aqueous media. It is known that functionalizing the C_{60} cage alters its innate physicochemical and photochemical properties, but how these changes translate to the properties of C_{60} aggregates, often termed nC_{60}, is not well understood. Functionalized fullerenes present an intriguing environmental dichotomy. On the one hand C_{60} has excellent potential as a novel singlet oxygen producing disinfection tool, and on the other the potential toxicological effects of functionalized C_{60} are largely unknown. With thousands of possible functionalities, a mechanistic understanding of the effects of functionalization is essential.

To explore the effects of functionalization on fullerene photochemistry in relevant systems, three types of functional groups were selected and obtained each in series of mono-, bis-, and tris-functionalized forms. Two functionalities contrasted the presence or lack of a quaternary ammonium group and the third was the sterically bulkier phenyl-C_{61} butyic acid methylester, which is commonly used in polymer photovoltaics. The fullerenes were characterized for innate photochemical properties in organic solvents

using UV/Vis, laser flash photolysis, and photochemical degradation experiments. Aqueous aggregates of each derivative were prepared via a sonication method and subjected to the same protocols with additional characterization of their physical and chemical properties by dynamic light scattering, transmission electron microscopy, energy dispersive x-ray spectroscopy, and x-ray photoelectron spectroscopy. All derivatives were found to be similarly photoactive when dispersed molecularly in organic solvents, but only the cationic fullerenes showed significant photoactivity as aqueous aggregates. Differences in aggregate size or crystallinity were unable to explain the differential photoactivity between derivatives, contrary to two established hypotheses. Antimicrobial properties were probed using innate toxicity tests and photoinactivation experiments. Again, only the cationic fullerenes were found to exert photochemical action towards *Escherichia coli* or MS2 bacteriophages. The cationic fullerenes were also innately toxic to *E. coli* due to the presence of quaternary ammonium moieties.

In order to establish a mechanistic understanding of the photochemistry of functionalized C_{60} aggregates, simulations of the molecular dynamics (MD) were employed and compared with empirical evidences. Simulations provided theoretical values for C_{60}-O_2, C_{60}-C_{60}, and C_{60}-H_2O interactions for each derivative. Trends observed in the MD results were compared to photochemical characterizations as described above and Raman spectroscopic measurements of C_{60}'s effect on localized water structure. High resolution transmission electron microscopy was used to provide empirical evidence of the C_{60}-C_{60} interactions. These observations collectively suggest that fullerene aggregate photochemistry is driven by aggregate morphology and by intermolecular interactions between fullerenes, water, and O_2.

1. INTRODUCTION

In recent years fullerenes have attracted great interest and research across many fields, from photovoltaics [1-3] to pharmaceuticals [4-6]. Buckminsterfullerene, or fullerene for short, is a carbon allotrope much like diamond and graphite, but in a spherical shape. Pristine fullerenes are found in a variety shapes and sizes, with the most common and stable molecules having the arrangement of a soccer ball with 60 carbon atoms, or C_{60} [7]. The terms fullerene and C_{60} are often used interchangeably. An individual C_{60} molecule measures approximately 0.7 nm in diameter, making them truly nano materials. Fullerenes have been studied extensively for their unique, non-planar, pi-conjugated electronic configuration.

1.1. Fullerene Photochemical Reactivity

Unique photochemical properties of C_{60} were recognized by the scientific community not long after its proposed existence by Kroto *et al*. in 1985 [7]. While C_{60} does not fluoresce or phosphoresce in the ambient environment, C_{60} in organic solvent in its ground singlet state ($^1C_{60}$) is readily excited to singlet state $^1C_{60}$* very efficiently with quantum yield of nearly 1.0 (100%) upon UV and visible light irradiation [8]. Photo-excitation of C_{60}, with a band gap of 2.3 eV, can be accomplished by photons with wavelength below 550 nm, which are abundant in the solar spectrum. The $^1C_{60}$* can either convert back to the ground state by fluorescence and internal conversion processes or transition into triplet state ($^3C_{60}^*$) through intersystem crossing (ISC), a process

favored due to the non-planarity of the pi conjugated cage. The resulting triplet state $^3C_{60}^*$ is subject to three quenching pathways: 1) triplet quenching by energy transfer to a ground-state triplet oxygen ($^3O_2$) molecule, which results in photochemical generation of singlet oxygen ($^1O_2$); 2) self-quenching through interactions between triplet and ground state C_{60}; and 3) triplet-triplet annihilation between adjacent triplet state C_{60} [9, 10]. In the presence of oxygen, energy transfer to oxygen (*i.e.*, the first quenching mechanism) is dominant with very high yield (*e.g.*, $\Phi(^1O_2)$ at 355 nm = 0.76 in benzene [8]). This is illustrated below:

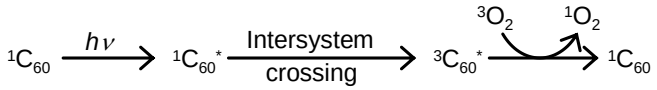

Due to a somewhat unusual electronic configuration, the oxygen molecule in singlet state, $^1O_2$, is higher in energy than triplet state [11]. This non-radical, transient species is highly energetic and exhibits strong, substrate-specific oxidizing power [11, 12]. $^1O_2$ can be generated via: 1) energy transfer by photosensitizing chemicals to oxygen, 2) pulse radiolysis in the presence of an energy mediator such as benzene, 3) microwave discharge, and 4) chemical pathways (*e.g.*, chemical oxidation of hydrogen peroxide) [11, 12]. Since the role of metastable $^1O_2$ in dye-sensitized photo-oxygenation reaction was first suggested by Kautsky et al in 1939 [13], its oxidation potential has been exploited in applications including specific chemical synthesis [14, 15] (*e.g.*, Ene and Diels-Alder reactions) and cancer and tumor therapies [16, 17]. Based on the finding that $^1O_2$ generated by photoactivation of natural organic matter (NOM) plays a critical role in degrading micropollutants in natural aquatic environment [18], $^1O_2$ has been considered as an alternative oxidant for water treatment. Recent studies have suggested that $^1O_2$

produced using photosensitizers efficiently oxidizes various organics and pollutants, such as substituted phenols, malodorous organic sulfides, and benzimidazole fungicides [19-21]. Concurrently, application of $^1O_2$ as a disinfectant has been also reported [22, 23]. Although $^1O_2$ is produced as a protective agent in natural systems, it can cause cell death, particularly in the absence of natural, specific $^1O_2$ quenchers (e.g. β-carotene) [24]. In fact $^1O_2$ has been suggested for use in photodynamic therapy and inactivation for its anti-cancer and antimicrobial effects, respectively. $^1O_2$ is known to preferentially react with vital cell components (e.g. nucleic acids, cell walls, peptides, and phospholipids) [25]. The preferential reactivity of $^1O_2$ makes it ideal for inactivating viruses, which generally have unprotected nucleic acids, and cancer cells which can be targeted to preferentially uptake the photosensitizer. It is vitally important, therefore, to understand the interaction of $^1O_2$ sensitizers and their possible implications and exposure pathways to humans and other organisms.

Strong photocatalytic activity of C_{60} for producing $^1O_2$ is both a major concern for its photooxidative potential and a possible tool for pharmaceutical and disinfection. However, its intrinsic hydrophobicity and extremely low water solubility ($< 10^{-9}$ mg/L) [26] make the direct availability of pristine C_{60} in the aqueous phase impossible. Therefore, enhancing apparent solubility in the aqueous phase, which is critical for many applications, is a serious environmental concern. Enhanced aqueous solubility can be achieved by the following three known pathways: 1) C_{60} can be dispersed as negatively-charged colloidal forms (often referred to as nC_{60}) of sizes ranging from 60 to 400 nm [27, 28]; 2) C_{60} can be suspended in the aqueous phase through association with foreign molecules such as surfactants, polymers, lipids, and carbohydrates [29-31]; and 3)

multiple hydrophilic groups (e.g., hydroxyl, amine, and carboxylic groups) can be added to the surface of the C_{60} cage [32, 33]. Colloidal particles could be important as nanosized catalysts that provide large surface areas for reaction. However, recent studies demonstrated that the unique photochemical properties of C_{60} to produce $^1O_2$ disappear as C_{60} forms aggregates in water [34-36], due to the self-quenching pathways described above. Encapsulating agents are not practical to consider for either environmental scenarios or applications of C_{60} due to the quantity of materials required (and released as pollutants) to encapsulate C_{60} in this way. As functionalized C_{60} is dispersed as an individual molecule in the aqueous phase, photochemical activity for $^1O_2$ production is retained [32, 33]. For these reasons many researchers are turning to functionalized C_{60} for their applications, spurring a greater need for understanding how functionalization affects C_{60}'s physicochemical properties in water.

1.2. Functionalized C_{60}

1.2.1. Functionalization on Photochemistry

Studying the effects of covalently functionalizing fullerenes has been particularly insightful over the past 15 years. Solvent interactions with functional groups, alterations of the pi-conjugated electron configuration of C_{60}, and geometric changes in bond angles due to functional groups are suggested as the primary ways functionalization affects the photophysical properties of fullerenes. An overly simplistic view of solvent interactions, which will be discussed below, is somewhat useful for conceptualization: fullerenes are highly non-polar by nature and are therefore not compatible with polar solvents.

Functionalization of C_{60} with hydrophilic, or polar, groups allows more favorable arrangements for the polar H_2O molecules around the C_{60} derivative. As described above, the degree of aggregation, caused by hydrophobicity, can drastically affect the photocatalytic properties of C_{60} in water. Altering the pi-conjugated system of fullerenes is more intricate in the way it affects C_{60}'s properties. Upon functionalizing C_{60}, there is a disruption of the sp^2 network due to the lifting of a [6,6] double bond (the most favorable site for functionalization), which would blue-shift the ground state absorption spectra [37-39]. The functional group itself, however, often gives additional pi-conjugation to the system via sp^2 hybridized structures (e.g., cyclopropane rings, phenyl rings, carbonyl groups) resulting in the red-shift often observed in functionalized fullerenes [37-40]. A net red-shift in a fullerene's ground-state absorption would tend to increase the quantum yield of $^1O_2$, but the triplet intermediate state is also important for the formation of $^1O_2$. Although the first excited singlet state may be reduced in energy, efficient energy transfer to the triplet state is critical. While the singlet excited state is reduced in energy, the triplet state tends to increase in energy with additions of functional groups due to a local relaxation in the bond geometry around the functional group [38, 39, 41]. This rationale comes from the fact that the ISC process is enhanced by a departure from planarity in sp^2 hybridized systems and leads to a net decrease in $^1O_2$ quantum yield with increasing numbers of addends [38, 40].

1.2.2. Cationic Functionalization

The unique physicochemical properties of C_{60} are severely diminished upon aggregation into aggregates, often termed nC_{60} [28, 35, 36]. Functionalization has helped to overcome the issues of aggregation, primarily with hydrophilic functionalities, at the

cost of an increasingly complex system [42-47]. Functionalization of nC_{60} post aggregation, through irradiation [48, 49] or ozonation [50] has also proved to re-enable photochemical pathways in nC_{60}, raising questions concerning the implications, fate, and transport of nC_{60} through natural and engineered environmental systems. It should also be noted that sonication, a common method to disperse C_{60} as aggregates, also has potential for functionalizing C_{60}'s cage via radical formation, particularly in the case of high intensity sonication probes [51]. It is well documented that nC_{60} from various preparation techniques have somewhat variable photophysical properties [28, 52-55]. Although nC_{60} was initially observed to be cytotoxic [55-57], later reports revealed that residual tetrahydrofuran (THF) peroxides from a solvent exchange procedure were responsible for the toxic response [58-62]. Additionally, many studies have shown nC_{60} to be relatively non-photoactive [35, 36, 63], while some researchers utilizing a sensitive $^1O_2$ probe and high intensity, probe sonication found slight photoactivity in nC_{60} preparations [53, 64]. The photoactivity of fullerenes, especially the sensitization of $^1O_2$ or other reactive oxygen species, is of primary interest to biological and environmental systems; therefore, understanding the role of functionalization and aggregation state on the photochemistry of fullerene aggregates is vital.

Many studies have shown cationic functionalized fullerenes to be particularly important given their enhanced aqueous solubility and resultant photoactivity in biological or aqueous media [43, 45-47, 65-67]. These studies, however, either dealt with derivatives that were highly water soluble with negligible aggregation [43, 65], a surfactant for micelle formation [68], or with the use of dimethyl sulfoxide (DMSO) to prevent aggregation [45, 47, 66, 67]. While these scenarios were indeed very important to

study, they may not be as realistic for environmental considerations as mildly functionalized fullerenes as colloidal aggregates. Only recently have aggregates of positively charged fullerenes been well characterized and studied for their photochemical properties [63]. In order to assess the implications of aggregates of fullerene derivatives in the environment, it is imperative to understand the relationship between the structure of the derivative and the (photo)biological properties of the resulting aggregation. The need for structure-activity relationships to guide investigation and policy decision making has recently been emphasized by several groups, taking initial steps forward [53, 57, 63, 64, 69].

1.3. Aqueous Aggregation of Fullerenes

The subjects of aggregation process and associated surface oxidation and their influence on the fate and photoactivity of C_{60} in aqueous media are receiving much attention from the environmental science community. It is necessary to understand the fundamentals of C_{60}-water interactions and the quenching of excited states in aggregates, because C_{60} applied or released to biological or environmental systems will require the formation of aggregates, given their aqueous natures.

1.3.1. C_{60} Hydration Theory

The nature of H_2O-fullerene interactions is more complex than the simplification that assumes hydrophobic materials repel water and therefore aggregate to each other. While this view appears to be valid at first look, the actual mechanism for action lies in the Lewis acid-base (AB) interaction, or hydrophobic interactions [70], which are

contained in extended Derjaguin and Landau, Verwey and Overbeek (DLVO) theory models [71]. In fact, the so-called hydrophobic materials are actually known to attract water through this acid-base hydrophobic attraction mechanism [71, 72]. While the classic DLVO theory has been applied to the stability of C_{60} aggregates by Chen and Elimelech [73] which proved to be predictive of the colloidal stability based on their surface potentials, the actual interaction of C_{60}-C_{60} in an aqueous system are very likely driven by the AB forces. A study on the octanol-water partitioning of C_{60} estimated the solubility of pure, individually solvated C_{60} to be extremely low (*ie*., 7.96 ng/L) [74], yet it is well known that as colloidal aggregates on the nanoscale, nC_{60} concentrations of mg/L or higher can easily be obtained. The formation of nanoscale aggregates implicates the Lifshitz-van der Waals (LW) attractive forces as a mechanism to aggregate the individual C_{60} molecules in solution; additionally, a study on size fractionated samples of nC_{60} by Chae *et al*., found that smaller sized aggregates had more negative surface potentials and more oxidized surfaces [75]. Their study also measured attachment efficiencies of the fractionated aggregates to a silica surface and noted that their observed trends in attachment efficiencies for the various aggregates and corresponding surface potentials could not be explained by classical DLVO theory; they hypothesized that the differences in affinities lied within the difference hydrophilicity and hydrophobicity of the aggregates and the surface [75], but their observations would likely be explained by the extended DLVO theory that includes AB interactions. Several other studies on the transformation of nC_{60} by various treatments have shown similar results of decreased aggregate size and increased photoactivity when the absolute surface potential was increased by the addition of oxides or halides to the surface of aggregates [48, 49, 76-81].

Researchers have turned their attention to molecular dynamics (MD) as a theoretical basis for understanding the C_{60} hydration phenomenon. The theoretical approach complimented by a suite of physical measurements of oxygen or water associated with C_{60} has proved to be instrumental for conceptualizing the interactions of C_{60} and water. An early study involved calculating an optimized structure for C_{60} clusters that have been postulated to be the building blocks of larger aggregates; the researchers found structures of approximately 33 C_{60} molecules to be energetically favorable and supported the notion of the hydration phenomenon having a role in cluster formation with Raman and optical spectroscopy [82]. Another publication provided spectroscopic data in the form of Raman, FTIR, and small angle neutron scattering (SANS) on an nC_{60} solution to compliment a geometrically optimized model of a single C_{60} in water, which the authors showed to be in the form of $C_{60}(H_2O)_{60}$ [83]. As computing capabilities continue to improve, more and deeper studies on the molecular dynamics of C_{60}-H_2O have been conducted, delineating the clathrate-like structure of sequential water layers around the C_{60} cage [84-88]. These studies on hydration dynamics found that due to the 'hydrophobic effect' of AB interactions of water surrounding the apolar surface H_2O molecules assembled highly ordered cages around the C_{60} in concentric spheres, starting from *ca*. 6.5 Å from the C_{60}'s center of mass [84-86, 88]. Experimental studies have given much credence to the simulations, providing evidence of water interactions with C_{60} through Raman, FTIR, and x-ray photoelectron- spectroscopy (XPS), contact angle and atomic force microscopy (AFM) measurements, and simple physical characterization of first-order thermal transitions for nC_{60} solutions [78, 82, 83, 89-91]. These evidences of a strongly bound hydration layer have many implications regarding aggregate

formation and energy transfer mechanisms, as these hydration layers are known to influence many aspects of colloidal and biological interactions [92, 93]. As will be discussed in following sections, our initial results may also provide evidence of these surface phenomena playing a role in the photochemistry of aqueous aggregates [63].

1.3.2. Environmental Implication Perspective

As of November 2010 the U.S. EPA has granted approval for a company called *Nano-C, Inc.* to commercially produce fullerenes and PCBM (Phenyl-C61-Butyric acid Methyl ester), a specific fullerene derivative used in organic photovoltaics (OPV). This approval marks an important step forward for fullerene materials from the requirement of having the conditional approval of a Pre-Manufacturing Notice (PMN). Although pure fullerenes and PCBM have approval, there are thousands of potential novel derivatives that may be studied in fields ranging from OPV to pharmaceuticals that are still subject to the EPA's PMN process. As commercial production drives down the costs of obtaining pure C_{60}, the rate of new fullerene derivatives being created will only increase along with the need for corresponding materials data. With endless possibilities of fullerene structures, each with unique chemical properties, it is unreasonable to scrutinize each derivative individually for photophysical and toxicological properties. A method of predicting a derivative's properties based on its structure, therefore, is ideal for the effective regulation of fullerene derivative production and application. This predicament has been encountered in several other classes of organic molecules, namely endocrine disruptors [94], pesticides [95], and substituted phenols [96]. Although a quantitative structure-activity relationship (QSAR) studies have often been used to tackle these problems historically [97], such a strategy is not yet feasible for fullerene derivatives due

to scarcity of data and materials. Pristine C_{60} has been the object of a modest amount of environmental implications studies [98], but there is a lack of these data on fullerene derivatives.

Given the complexity of how C_{60} functionalization affects its $^1O_2$ production capacity, as described above, there are several concepts that must be assimilated in order to understand the potential implications of novel fullerene derivatives in the environment. First, the extent and characteristics of aggregation, dependent on the hydrophilic nature of the functionalization, will directly affect the $^1O_2$ production efficiency of C_{60} derivatives. Second, the alterations of the fullerene's pi-conjugated structure depend both on the type and amount of functional groups attached in determining the ground state absorption peak shift; red shifted derivatives will have enhanced absorption in the visible spectrum and therefore an increased $^1O_2$ quantum yield. Third, the triplet excited state energy of C_{60} increases with the number of addends, which will directly decrease the $^1O_2$ quantum yield through a less favorable energy from $^1C_{60}$* to $^3C_{60}$*. Given these three mechanisms a relationship between $^1O_2$ production and nature of functionalization must be established in order to understand the risks of various derivatives. For example, if a particular derivative has been stabilized in aqueous media and retains excellent photocatalytic efficiency in the visible spectra, there is great concern for the implications. In particular, a stabilized colloid in the nano scale may not be effectively removed by conventional water treatment processes and the fate of such a material would be uncertain. In addition to the concern of the physicochemical properties imbued by the functionalization, recent groups have incorporated quaternary ammonium groups, which are known to have biocidal properties [99], onto the C_{60} cage [45, 100], raising even further concerns of

potentially harmful functionalities becoming available via the incorporation onto fullerene cages. The vast range of possible fullerene derivatives is both menacing in terms of risk assessment and exciting in terms of potential applications; it is, therefore, critical that great effort is spent on ensuring public safety through regulation of materials without hindering further advancements in the field.

1.3.3. Environmental Application Perspective

There is great need for the development of novel materials (e.g., polymer composites) that, in response to visible light, efficiently inactivate viruses (such as norovirus, a common virus that causes gastrointestinal disease) and spore forming bacteria (such as Bacillus anthrax, a bioterrorism agent) that survive in dry conditions. Such materials would be highly useful for advancing solar disinfection (SODIS) and antimicrobial/biocidal coating technology. Fullerenes have recently been proposed by several groups as effective antimicrobial agents, via photocatalytic production of $^1O_2$ and subsequent microbial inactivation [45, 100-102]. In contrast with the ubiquitous TiO_2 photocatalyst [103], functionalized fullerenes have the advantage of being able to be covalently anchored to a host material and to respond to visible light. Covalent attachment of photocatalysts is a key step in overcoming many hurdles in their application as disinfectants, opening many possibilities for further development. In general photocatalysts for disinfection should be recoverable/reusable, completely conserved (no leaching into the environment), responsive to visible light, and able to retain their catalytic properties over repeated use. Fullerene derivatives are very attractive as photocatalysts because they can potentially exhibit these essential characteristics when covalently anchored into polymers. The possibilities for application of these fullerene-

polymer composites are extensive. With countless types of functional groups possible, there is a great opportunity to optimize fullerene derivatives for these specialized applications.

1.3.4. Outstanding Questions

The photocatalytic properties of fullerenes are known to be altered by the nature and number of functionalities; the type of addend can affect the fullerene's visible absorption spectra [37], while the number of adducts has been shown to decrease the $^1O_2$ production efficiency [40]. Parallel to the case of environmental implications of fullerene derivatives, effectively applying them requires the ability to understand and predict how their physicochemical properties affect their photocatalytic and antimicrobial properties. Answering the following questions will provide the information necessary to achieve the goals of both applications and environmental implications of novel fullerene derivatives:

- How do the type and number of functionalities affect the photophysical and chemical properties of fullerenes?
- How do the photophysical and chemical properties of functionalized fullerenes affect their aqueous hydration, stability, and photosensitizing capacity?
- How can we predict the photocatalytic properties of novel fullerene derivatives based on their functionalities?
- How do the aggregation and hydration states of aqueous fullerene aggregates affect their energy transfer processes with molecular oxygen?
- Which fullerene derivatives are best suited for use in environmental applications, specifically for the treatment and disinfection of water?

1.4. Hypotheses

Concerns and questions surrounding the application of fullerene derivatives in the environment outlined above could be addressed by conducting a thorough QSAR-like study on a selected range of fullerene derivatives. To address these questions, the following hypotheses must be tested.

1. Functional groups that add to C_{60}'s pi-conjugated electronic system will result in a red-shift in its ground state absorption peak. Red shifted derivatives will exhibit enhanced visible light absorption and consequently enhanced photosensitizing efficiency under visible irradiation.
2. Each successive addend to the C_{60} cage will increase the energy of the triplet intermediate state of C_{60}, thereby decreasing the $^1O_2$ quantum yield.
3. Addition of hydrophilic groups to the fullerene cage will cumulatively increase the magnitude of the zeta potential of the derivative, resulting in less aggregation in the aqueous phase. Larger fullerene aggregates will have decreased $^1O_2$ quantum yield due to self-quenching pathways.
4. Fullerenes with the highest $^1O_2$ efficiency will achieve the fastest microbial inactivation rates. Additionally, fullerenes with positively charged quaternary ammonium groups will have further accelerated microbial kill rates.
5. Modeling of the nature of molecular interaction with the C_{60} cage (H_2O-C_{60} or C_{60}-C_{60}) will be predictive of changes in hydration and aggregation dynamics which will,

in turn, be predictive of the aggregates photochemical and physical interactions with other constituents in an aqueous system.

2. RESEARCH OBJECTIVES

A QSAR-like study was performed for a series of fullerene derivatives to establish the first steps towards developing a tool for predicting how functionalization of C_{60} affects their properties of interest and concern for environmental applications and implications. Fullerene derivatives were characterized for physicochemical characteristics as well as antibacterial/biocidal activity, towards establishing structure-activity relationships. Molecular modeling, in conjunction with key experimental evidences, was also performed for delineating the dynamic molecular interactions at the interfaces of fullerene aggregates. Primarily, the objectives were the following:

1) To thoroughly characterize the photophysical and chemical properties of the set of fullerene derivatives.
2) To assess the antimicrobial and photocatalytic potential of the fullerenes.
3) To elucidate the mechanisms behind the presence or absence of photoactivity among functionalized fullerenes by generating models of the dynamic molecular interactions based on C_{60} functionalization.

A series of select, water soluble fullerene derivatives were obtained through The Chemical Research Solutions LLC, a commercial custom synthesis company. These materials, outlined in section **4.1**, provide a clear comparison between the numbers and types of adducts to the fullerene cage. Characterization (objective 1) were carried out using instruments outlined in section **4.2**.

3. SIGNIFICANCE

There are few studies correlating fullerene functionalities to their properties and even fewer that examine the environmental applications and implications of fullerenes. Unique properties of C_{60}, including 1) exceptional photocatalytic activity for $^1O_2$ production; 2) ability to utilize visible light for photoexcitation; 3) chemical stability and 4) ability to be functionalized, make it very interesting for many applications, including water treatment, and a potential concern for its environmental implications. Many questions remain to be answered, however, before the application and regulation of fullerene derivatives can be successful. Conducting a QSAR-like study and establishing a foundation for predicting the properties of fullerene derivatives based on their functionalities is a significant advancement for novel fullerene technology. In particular this thesis provides the foundational information necessary to utilize fullerenes in antimicrobial surface technologies. Additionally, the phenomena responsible for the formation of aggregates that quench C_{60}'s photoactivity as are not well understood. The results presented herein also provide key insights to the body of literature around the physical characteristics of aqueous C_{60} aggregates, and how their photophysical, photochemical, and biological properties depend on functionalization. These results have been shared with the scientific community via several peer reviewed journal articles.

4. APPROACH AND METHODOLOGY

Using strategically selected fullerene derivatives, outlined in section **4.1**, various analytical methods and techniques are employed to develop quantitative comparisons of the derivatives. The concern of fullerenes as photosensitizers in the environment, and for use in many applications, relies primarily on three factors: their ability to be excited by visible and UV light; their quantum efficiency of being excited to a triplet, excited state and to transfer energy (and electrons in the presence of electron donors) to oxygen to produce reactive oxygen species (ROS); and their surface properties which affect their interaction with target agents such as virus and spore-forming bacteria. These properties have been probed with a variety of techniques.

4.1. Materials

Deionized/distilled water (resistivity > 18.2 MΩ) from a Millipore ultrapure system (Millipore Co.) was used in preparation of all solutions and reagents. All chemicals used were analytical, reagent-grade and used as received, as specified for their given uses.

4.1.1. Fullerene Materials

Three functionalities of fullerene derivatives, seen in Figure 1, have been selected from literature as insightful derivations for comparison. All fullerene materials were used as received, with no further purification. Fullerene derivatives are abbreviated using the following nomenclature scheme: derivatives **A1**, **A2** and **A3** are mono-, bis- and tris-

fullereropyrrolidines, respectively [104]; under the same convention, **B** refers to the fulleropyrrolidinium ions [47] and **C** refers to phenyl-C_{61}-butyric acid methyl ester (PCBM) [105]. Sublimed C_{60} (99.9%) was obtained from MER Corp., Tuscon, AZ. **C1** (99%) was obtained from SES research, Houston, TX. **C2** (99.5%) and **C3** (>95%) were obtained from Aldrich, St. Louis, MO. **A** and **B** (>95%) were obtained from The Chemistry Research Solution LCC, Bristol PA. The purity of **A**, **B** and **C3** were guaranteed to be above 95% by the providers, with impurities consisting of the same derivative with more or less addends (*e.g.*, **B2** contains trace amounts of **B1** and **B3**). The derivatives have been specifically selected from literature as either being the most promising derivatives for their properties or for being logical structures for comparisons. Derivatives **A** and **B** set up a series that allow the effects of cationic quaternary ammonium functionalities to be elucidated. The parallel between fullerenes **A** and **B** in will exemplify the physicochemical differences of the presence of a quaternary ammonium group. Derivative **C**, or PCBM, is already an industrially important material that warrants greater attention, particularly for its bis- and tris-functionalized forms that have not received as much attention.

4.1.2. Preparation of Aggregates

Aqueous aggregates of the fullerene materials were prepared via sonication. Briefly, 9 mg of C_{60} or derivatives were added to 10 mL of toluene and sonicated in a bath sonicator (Fisher Scientific FS30) for 6 hrs in a sealed jar at ca. 60 °C. Ultrapure water (90 mL) was then added and the mixture was sonicated for 24 hrs. **B** derivatives were added directly to water, due to their insolubility in toluene. Finally, the mixtures were un-sealed and sonicated for an additional 24 hrs, allowing the toluene to evaporate.

Aggregate solutions were then filtered with 0.45 µm Whatman nitrocellulose filters. Filtered solutions were then concentrated using a rotary evaporator (Rotavapor R-200, Buchi corp.) and stored in the dark. Final aggregate concentrations were measured using a Total Organic Carbon (TOC) analyzer (TOC-V ws, Shimadzu corp.) and ranged from 10 to 230 μM.

Size fractionation of the **B2** and **B3** aggregates was accomplished using a series of polyethersulfone (PES, Millipore Co.) membranes with varying pore sizes: 0.45 μm, 0.22 μm, 300 kDa, and 30 kDa. The stock aggregate solutions were filtered through the PES membranes using a cartridge filter pressurized with N_2 gas. Resultant aggregate concentrations were calculated using a UV/Vis spectrophotometer (Agilent 8453, Agilent Co.). Aggregate sizes were measured using Dynamic Light Scattering (DLS) on a Zetasizer NanoZS90 (Malvern Instruments, Worcestershire, OK).

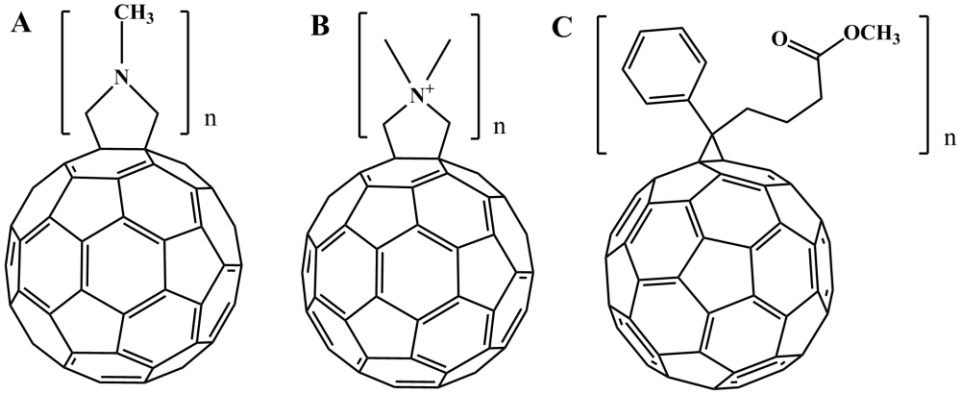

Figure 1: Fullerene derivatives, A) methylpyrrolidine, n = 1, 2 or 3 ; B) quaternary pyrrolidine, n = 1, 2 or 3 ; and C) phenyl-C6(n)-butyric acid methyl ester, n = 1, 2 or 3

4.2. Characterization

4.2.1. Purity and Identity Confirmation

Verification of the molecular forms of the derivatives has been accomplished using matrix assisted laser desorption-ionization mass spectrometry (MALDI-MS) and nuclear magnetic resonance (NMR) spectroscopy, as seen in Figure 38, Figure 39, and Figure 40 of the Appendix. The MALDI-MS experiments were performed directly with aggregate solutions on a mass spectrometer equipped with a 200 Hz laser (Applied Biosystems 4700 proteomics analyzer). The H-NMR spectra were collected using deuterated toluene for the **A** derivatives and deuterated DMSO for **B** in a Varian Mercury Vx 300 analyzer. Clear peaks in the MALDI-MS plots at expected molecular weights confirmed the parent molecules. The H-NMR spectra for the **A** and **B** derivatives further confirmed their molecular identities by consistent peak splitting patterns indicative of the structures of the functionalities. Observations of the elemental composition of samples during XPS and transmission electron microscopy (TEM) imaging provided further confirmation of the purity of samples, checking for trace metals in particular.

4.2.2. Physicochemical Characterization

Aqueous fullerene aggregates were measured for size and zeta potential using DLS and Phase Analysis Light Scattering (PALS) techniques, respectively. Aggregate suspensions were measured in triplicate with a low end detection limit of ca. 5 nm. The fullerene aggregates were assigned a refractive index of 2.2 [106]. TEM imaging coupled with Energy-Dispersive Spectroscopy (EDS) and electron diffraction patterns were used to confirm aggregate size, composition and crystallinity. A Philips 120 TEM was used at the MVA Scientific Consultants Inc. High resolution TEM (HR-TEM) images were collected using a Hitachi 7700 TEM. For imaging, TEM grids were prepared on carbon-

coated copper grids with square mesh. A Thermo K-alpha XPS and a Thermo Scientific Nicolet 6700 Fourier-transform infrared (FTIR) spectrometer in attenuated total reflectance (ATR) mode were used to further assess the degree to which the aggregate formation methods functionalized the aggregates. Aggregates were prepared then dried for XPS analysis or for inclusion into KBr pellets for FTIR analysis. Pristine powder for the fullerenes was used for comparison with the powdered aggregates. Differential scanning calorimetry (DSC) and Raman spectroscopy were used to probe the nature of water's interaction with the fullerenes on aqueous samples of fullerene aggregates.

4.3. Photochemical Experiments

4.3.1. $^1O_2$ Production

Photochemical activities of the fullerene materials were measured in both organic and aqueous (as aggregates) phases. Experiments were performed using a 50 mL cylindrical quartz reactor with a magnetic stirrer. Two experimental light conditions were used: Black Light Blue (BLB) lamps with wavelengths from 350-400 nm and Fluorescent Lamps (FL) with a UV cutoff filter for wavelengths > 400 nm. Irradiation intensities for BLB and FL conditions were probed with a potassium ferrioxalate actinometric method [107] and found to be 4.70×10^{-6} Einstein$\cdot L^{-1}s^{-1}$ ($\Phi = 1.26$) and 4.31×10^{-7} Einstein$\cdot L^{-1}s^{-1}$ ($\Phi = 1.11$), respectively [108]. For aqueous phase experiments, the reaction solution contained 40 mL total of 5 μM of fullerene aggregates, 10 mM phosphate buffer at pH 7.1 and 0.85 mM furfuyl alcohol (FFA) as a $^1O_2$ probe with a reaction rate of k (FFA + $^1O_2$) 1.2×108 $M^{-1}s^{-1}$ [109]. Organic phase reactions consisted of 5 µM of fullerenes

(fully dispersed) in toluene for C_{60}, **A** and **C** with 0.85 mM FFA. Due to **B**'s insolubility in toluene and differential $^1O_2$ lifetimes in solvents, FFA experiments were not performed for **B** in the organic phase. A positive control for $^1O_2$ production was conducted with the well-known $^1O_2$ sensitizer, Rose Bengal (Figure 41 in the Appendix). Negative controls were conducted under dark conditions and with L-histidine, a well-known $^1O_2$ quencher.

4.3.2. Laser Flash Photolysis

Nanosecond transient absorption spectra of triplet states of C_{60} derivatives were measured using laser flash photolysis (LFP). The LFP experiments were carried out under air-equilibrated conditions. The third harmonic generation (THG, 355 nm) of a Q-switched Nd:YAG laser (Continuum, Surelite II, pulse width of 4.5 ns, full width at half maximum, fwhm) was applied as the excitation light. A Xenon lamp (ILC Technology, PS 300-1) was focused on the experimental suspensions as the probe light to monitor the transient formation and subsequent decay. The temporal profiles were recorded using a monochromator (Dong-Woo Optron, Monora 500i) equipped with a photomultiplier (Zolix Instruments Co., CR 131) and a digital oscilloscope (Tektronix, TDS-784D). The transient absorption spectra were measured by an intensified charged-coupled device (CCD) with a gate time of 1.6 ns and a 10 ns time delay (Ando Technology, iStar).

The sub-picosecond transient absorption spectra of triplet states of functionalized C_{60} were obtained with a pump-probe transient absorption spectroscopy system (Ultrafast Systems, Helios). The pump light was generated using a regenerative Ti:sapphire laser amplifier system (Coherent, Libra-F, 1 kHz) with a diode-pumped Q-switched laser (Coherent, Evolution). The seed pulse was generated by a Ti:sapphire laser (Coherent, Vitesse). The pulse (355 nm) produced from an optical parametric amplifier (Coherent,

TOPAS) was used as the excitation pulse. The pump pulse passes through a mechanical chopper synchronized to one-half of the laser repetition rate, resulting in a pair of the spectra with and without the pump, from which absorption change induced by the pump pulse was projected.

4.4. Antimicrobial Activity

Bacteria and virus inactivation experiments were performed in the bulk, aqueous phase for fullerenes as aqueous aggregates. Antibacterial and bactericidal properties of functionalized fullerenes were evaluated based on three complimentary approaches: 1) minimum inhibitory concentration (MIC) tests, 2) viral inactivation kinetics tests in solution, and 3) bacterial inactivation tests in solution. Test species included gram-negative *Escherichia coli* (*E. coli*) and MS2 bacteriophage. These methods have been regularly used to evaluate disinfection kinetics and mechanisms by various disinfectants and selected nanomaterials [63, 102, 110-114].

4.4.1. Photoinactivation Setup

The photo-reactor used for experiments consisted of three 6-watt fluorescent lamps (FLs) with a UV cutoff filter (400 nm) or three 4-watt Black Light Blue (BLB) lamps oriented directly above a magnetically stirred reaction vessel. Emission spectra are provided in Figure 42 in the Appendix. Incident intensities measured at 365 nm using a UVX Radiometer (UVP, LLC) were 38.0 μW/cm^2 and 1.17 mW/cm^2 for the FL (without the UV cutoff filter) and BLB lamps, respectively. A blue light sensor (PMA 2121, Solar

Light Co.) was also used for the FLs, with an average value of 482 μW/cm^2. Sunlight experiments were performed on the Georgia Institute of Technology's campus in Atlanta, Georgia (33°46'25" N, 84°23'38" W) using a reaction vessel on a magnetic stirrer under open sunlight on the 4th and 12th of September, 2013. On both days experiments were conducted between 1:00 and 1:30 pm EST, the ambient temperature was measured at 36 ºC, the blue light intensity averaged *ca*. 2.8 mW/cm^2 and the UVA intensity averaged *ca*. 1.0 mW/cm^2. The maximum UVA intensity reached a high mark of 1.20 and 1.01 mW/cm^2 on the 4th and 12th, respectively. Production of $^1O_2$ production was measured using furfuryl alcohol (FFA), a $^1O_2$-selective probe compound (k (FFA + $^1O_2$) = 1.2 × 10^8 M^{-1}s^{-1}).[109, 115] Production of superoxide radical anions ($O_2{\cdot}^-$) was measured using nitro blue tetrazolium (NBT^{2+}) [35] and XTT (2,3-bis(2-methoxy-4-nitro-5-sulfophenyl)-2*H*-tetrazolium-5-carboxanilide salt) [116] with or without dimethylaniline (DMA) [117] as an electron donor. $O_2{\cdot}^-$ anions were produced at varying concentrations via KO_2 dissolution to calibrate the XTT and NBT^{2+} methods [35].

4.4.2. Antimicrobial Experimentation

All microbial agents were obtained from the American Type Culture Collection (ATCC). Photoinactivation experiments were conducted with *E. coli* and MS2 bacteriophages according to methods reported previously [43, 48, 50, 65]. All reagents and materials were either used directly from sterile packaging or autoclaved at 121ºC for 20 min prior to use. Briefly, the *E. coli* photoinactivation experiments were performed using the ATCC 8739 strain inoculated in 30 mL of nutrient broth (BD inc., Difco^{TM}) and incubated at 37 ºC for 18 h in a shaking incubator. The inoculation resulted in a

stationary-phase culture with ca. 2.0×10^8 cfu/mL. The cultured E. coli were diluted into the reactor solution with phosphate buffered saline (PBS) solution, resulting in 10 mL total volume consisting of fullerene aggregates, PBS, and ca. 2.0×10^6 cfu/mL *E. coli*. The bottom half of a 60 mm diameter sterile petri dish with a magnetic stirrer was used as the reaction vessel and placed in the photoreactor with UVA light as detailed below. Aliquots of the reactor solution were sampled periodically, diluted, and spread onto nutrient agar plates and counted after incubation for 18 h at 37ºC.

The MS2 photoinactivation experiments were setup in a similar fashion to the *E. coli* reactors, following recently used protocols [43, 65]. The ATCC C3000 *E. coli* strain was used as the host bacteria for the bacteriophages and was grown for four hours on tryptic soy broth to reach the exponential growth phase. MS2 stocks at ca. 10^{11} pfu/mL, which had been centrifuged to separate virus particles from cell debris, were spiked into the reactor solution containing PBS and fullerene derivatives to achieve a 10 mL volume with 10^8 pfu/mL, and placed light irradiation as described below. Sample aliquots were withdrawn at time intervals, added to a soft agar nutrient solution with *E. coli* C3000, poured onto prepared agar plates, and incubated for 18 h at 37ºC. Plaques of MS2 formed where the *E. coli* were infected by the viral agents and were counted to observe the inactivation of MS2 as a function of irradiation time. Natural Organic Matter (NOM) from the Suwannee River (International Humic Substance Society, RO isolation) was used to simulate environmental conditions.

Innate antimicrobial properties of the fullerene derivatives were assayed using a minimum inhibitory concentration (MIC) test, following the methods typically used for fullerene aggregates.[48, 56] A modified Minimal Davis media was prepared and used as

a growth media for *E. coli* DH5α. Solutions of varying fullerene concentrations were prepared in multi-well plates with Minimal Davis media and DH5α. The plates were then incubated for 18 h at 37 ºC. Growth inhibition was determined by optical density, OD_{600}, of the wells, where the lack of growth indicated bacterial inhibition.

4.5. Molecular Dynamics Simulations

Molecular dynamics (MD) simulations have become a standard method to investigate time-evolved physical motions of atoms and molecules in a system of interacting molecules. MD simulations of a single fullerene or of multiple fullerenes in aqueous solutions have been performed by researchers to obtain fundamental understanding of the solvent-induced behaviors of fullerene(s) [84, 118, 119]. In this study, the MD simulations were utilized to understand the physical movements and thermodynamic interactions on one or two fullerenes, including C_{60} and the **A** and **B** series, hydrated by 1,000 water molecules. The preparation procedure of the initial systems for the MD simulations is described in the following subsection. The MD simulations allow for analysis of the nature of hydration around the fullerene cage. The time-evolved trajectory of an O_2 molecule added into each system containing a fullerene/fullerene derivative hydrated by 1,000 water molecules was also investigated by the MD simulations to investigate the interactions of an O_2 molecule with the fullerenes. In all cases the MD simulations were performed under the canonical ensemble (NVT) condition at 298 K for 1 ns followed by the isothermal-isobaric (NPT) condition at 298 K and 1 atm for 1 ns to equilibrate the systems. Additional MD simulations were performed

in the NPT ensemble at 298 K and 1 atm for 1 ns to characterize physical and thermodynamic properties, including time evolved motions and thermodynamic interactions, the radial distribution functions (RDFs) of water molecules, and the mean squared displacements (MSDs) of water molecules within specific shells around the fullerenes. All MD simulations were performed through the large-scale atomic/molecular massively parallel simulator (LAMMPS) code combined with reliable atomic charges and force field parameters [120, 121]. Nose-Hoover thermo- and baro-stats were used to control the temperature and pressure in the NVT and NPT ensembles. The quantum mechanical (QM) method of the Jaguar software package (version 4.0, Shrodinger Inc.) with the B3LYP level of theory and 6-31+G(d,p) basis set was introduced to geometrically optimize a fullerene and its derivatives and then reliably predict their atomic charges. Charge-based coulombic interactions were handled using the particle–particle particle–mesh (PPPM) solver. DREIDING-type force field parameters, which have been improved by force field parameterization process described in the subsection 4.5.2, allow for reliable modeling of all possible interactions in the systems containing fullerenes with 1,000 water molecules (and an O_2 molecule) [122]. While it is difficult to make direct, physical measurements to verify these molecular simulations, the trends observed with sequentially functionalized fullerenes are expected to provide valuable information that are supported by the physical tests that are performed.

4.5.1. Preparation of the Initial Fullerene-Water Systems

The fullerene-water systems were initially prepared by adding one or two fullerenes and 1,000 water molecules into a cubic cell having a size of 30 Å × 30 Å × 30

Å. All the atoms in the systems were subsequently geometrically optimized using the improved DREIDING-type force field parameters (see section 4.5.2) in the Cerius2 software package (Molecular Simulations Inc., San Diego, CA). The cell size and shape were fixed during the geometry optimization. Figure 2 shows C_{60} with 1,000 water molecules after the geometry optimizations.

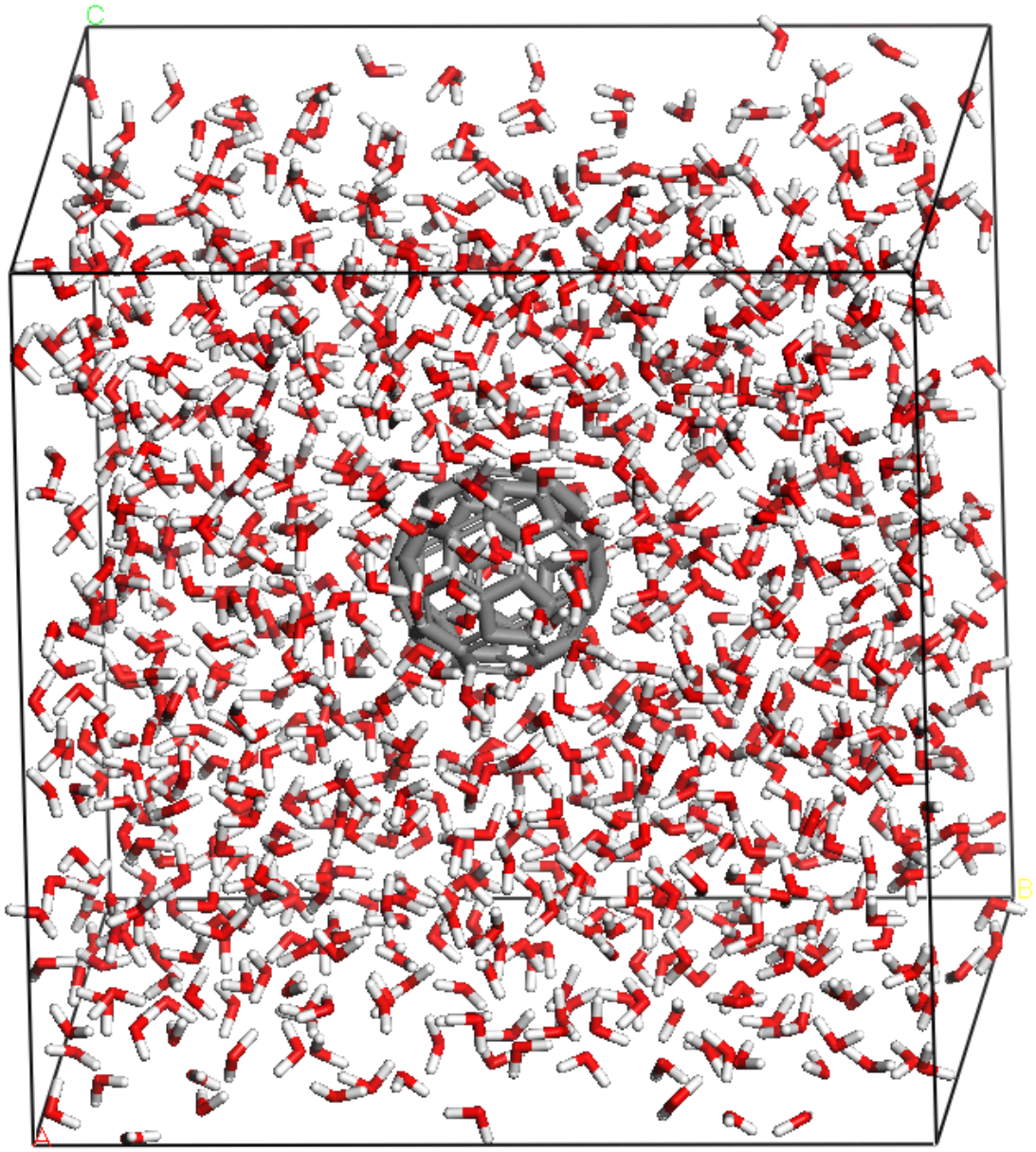

Figure 2: Geometrically Optimized system of 1,000 water molecules arranged around a single C_{60} molecule.

4.5.2. Force Field Parameterization

In general, the MD simulations in many studies are performed on the basis of the bonded and non-bonded interactions defined by the well-known DREIDING force field parameters. However, the pre-equipped force field parameters do not always accurately describe the non-bonded dispersion interactions in simulation systems, prompting many efforts to improve the force field parameters [123-125]. Here, these adaptations are employed to reliably describe the potential energy surfaces between a fullerene and a water molecule or between a fullerene and an oxygen molecule. A set of Morse potential parameters (D, R_e, a) was obtained by fitting to the potential energy surfaces of the two pairs (fullerene-water and fullerene-O_2) which were predicted by the QM calculations followed by the dispersion corrections. The Morse potential is defined by $V(r) = D\left(1 - e^{-a(R-R_e)}\right)^2$, where D is the well depth, R_e is the equilibrium bond distance, R is the distance between atoms, and a controls the 'width' of the potential. Two possible binding positions, namely positions on top of either hexagonal or pentagonal ring, were considered for predicting the potential energy surfaces of the two pairs.

All of our QM calculations were performed with the Perdew–Burke–Ernzerhof generalized gradient approximation (GGA) functional using the Vienna *ab initio* simulation package (VASP) [126-129]. The core electrons of each atom were described by the projector augmented wave method [130]. We used a conjugate gradient method for the geometry optimizations of the two pairs in a fixed cubic cell having a size of 30 Å × 30 Å × 30 Å. Such a large cubic cell was used to exclude the interaction effect between adjacent periodic images. A cutoff energy of 600 eV was used in all calculations.

Geometries were relaxed until the forces on all atoms were less than 0.005 eV/Å. All calculations were performed using a 2 × 2 × 2 Monkhorst-Pack mesh of *k*-points.

Figure 3 shows the comparison between the QM-based potential energy curves and the fitted force field based potential energy curves. For all four cases in the figure, the potential energy surfaces generated using the fitted force field are in a great agreement with those generated from the QM method. The fitted force field parameters are listed in Table 1. The improved DREIDING-type force parameters were therefore used in the MD simulations.

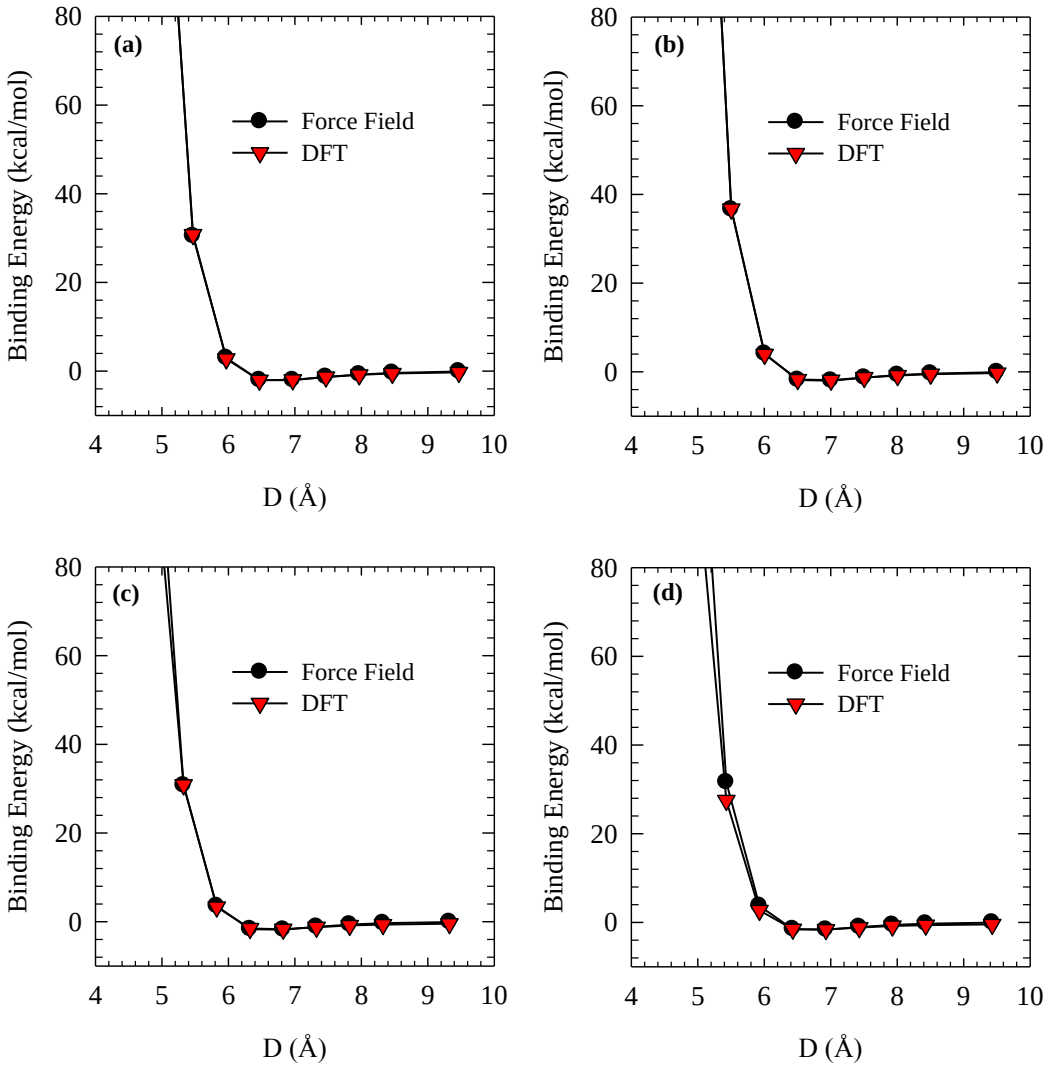

Figure 3: Comparison between the QM-based potential energy curves and the fitted force field based potential energy curves for H_2O on the (a) hexagonal and (b) pentagonal rings; and for O_2 on the (c) hexagonal and (d) pentagonal rings of C_{60}.

Table 1: Fitted force field parameters.

Atom pairs	*D*	R_e	*a*
$C(C_{60}) – O(H_2O)$	0.105677	4.299	1.314
$C(C_{60}) – H(H_2O)$	1.407436	1.858	2.142
$C(C_{60}) – O(O_2)$	0.118400	3.703	1.465

5. AGGREGATE FORMATION AND CHARACTERIZATION

This chapter describes the effects of aggregation on the physical, photochemical, and chemical properties on the fullerene derivatives, compared with their pre-aggregated states. This chapter provides experimental evidence that tests hypotheses one through three outlined in section 1.4.

5.1. Functionalization Affecting Photochemistry of Fullerenes

5.1.1. UV/Vis Absorption in Organic Solvent

The visible absorption spectra for C_{60}, **A**, and **C** in toluene are plotted in Figure 4 to compare relative absorption across the visible regions. Consistent with previous reports, mono-functionalized **A1** and **C1** exhibited red-shifted peaks resembling C_{60}'s characteristic 410 nm peak [104, 105]. The broad absorption band of C_{60} centered around 540 nm, which has been shown to correspond to forbidden singlet-singlet transitions [131], was blue-shifted and enhanced with each addition to the cage. This transition has been reported to be enhanced by interaction of $^3O_2$, implicating $^1O_2$ sensitization [131, 132]. Accordingly, it would be expected that these derivatives could have faster $^1O_2$ sensitization rates than C_{60} in the natural environment where broad-spectrum visible light dominates. Absorption in the visible range was enhanced with increasing functionalization due to extended conjugation of the pi electron system [133], such that **A3** > **A2** > **A1** > C_{60} and **C3** > **C2** > **C1** > C_{60}. Visible absorption of **A** was enhanced over **C**, such that **A1** > **C1**, **A2** > **C2** and **A3** > **C3**. The difference between **A** and **C**,

given the same number of addends, is somewhat unexpected given that the structure of the **C** addend contains more pi-conjugation (*i.e.*, the phenyl ring on C's addend) than **A**. This difference, however, may be explained by the diminishing effects of adding to a highly conjugated chromophore and the strain induced by the three-membered ring between the addend of **C** and the C_{60} cage compared with the five-membered ring in **A** [133, 134].

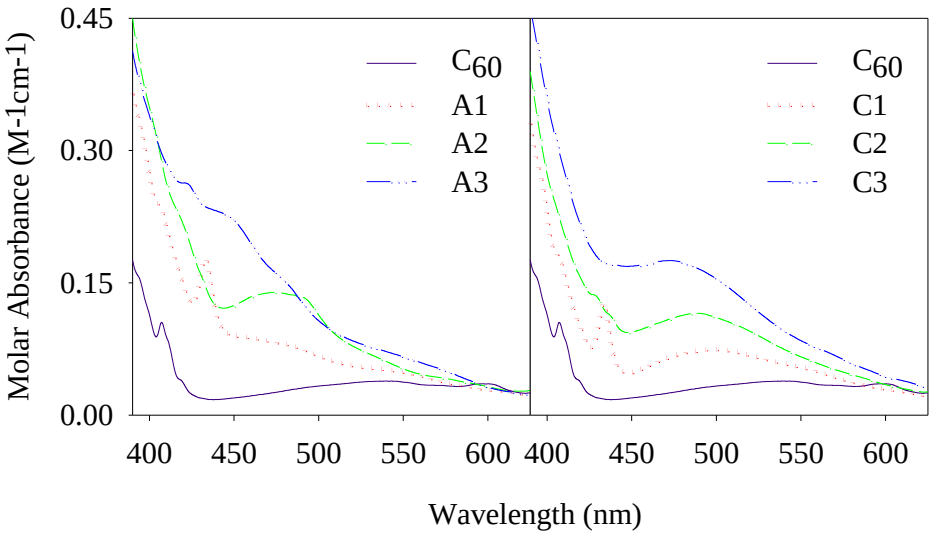

Figure 4: Visible absorption spectra for C_{60}, A and C derivatives in toluene.

5.1.2. Singlet Oxgyen Production in the Organic Phase.

Probing $^1O_2$ production, Figure 5 shows the FFA degradation curves for **A** and **C** in toluene under FL (a) and BLB (b) irradiation. Under visible light illumination, the derivatives showed enhanced $^1O_2$ production over pure C_{60}, which was consistent with the visible light absorption trends mentioned above, **C3** > **C2** > **C1** > C_{60}. The trend is

reversed under UVA irradiation, where there is less difference in absorption between derivatives. This reversal in kinetics between light conditions provides some evidence for less efficient ISC with higher triplet excited state and lower singlet excited state energy levels. **A** closely matched **C** in these FFA degradation patterns with the exception of not having distinguishable differences in kinetics under visible irradiation, which can be attributed to more overlaps in their visible spectra (*e.g.*, **A2** ≥ **A3** at 405 and 490 nm). Contrary to what is expected based on their visible absorption spectra, **C** exhibited enhanced $^1O_2$ production over **A** with visible light. This apparent contradiction implicates other factors, possibly more important than ground state absorption, that affect $^1O_2$ production (*i.e.*, the type of bond a functional group forms with the C_{60} cage may affect the $^3C_{60}{}^*$ lifetime). The apparent difference in reaction orders in the visible light cases can likely be attributed to the concentration of FFA used compared to the rate of $^1O_2$ production, such that rapid production yields a second order rate dependent on both [FFA] and [$^1O_2$] and slower production allows for a pseudo-first order case when a steady state $^1O_2$ concentration can be established [109].

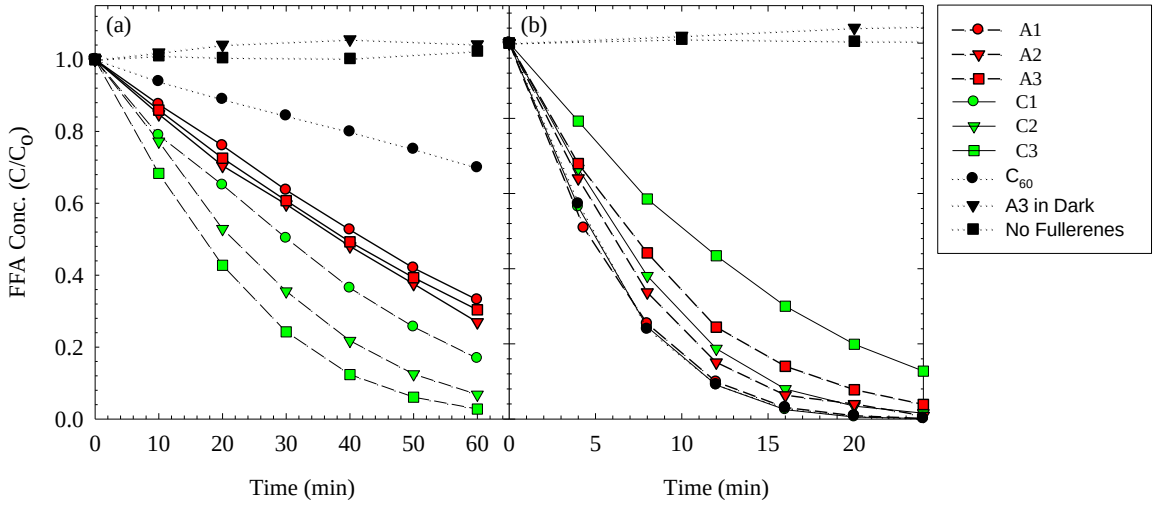

Figure 5: FFA degradation by C_{60}, **A** and **C** in toluene under (a) fluorescent lamps with cutoff filter (400-650 nm) and (b) black light blue lamps (350-400 nm).

5.2. Aggregate Photoactivity

5.2.1. Photochemical Characterization

Aqueous aggregates were formed at the nano-scale for all derivatives and were stable (unchanging in size) as prepared over several months, with the exception of **B1** which continued to agglomerate into larger particles after preparation. UV/Vis spectra taken at 5 µM are plotted in Figure 6. It is known that the UV/Vis spectra of fullerenes change significantly upon aggregation, resulting in broadened and shifted peaks, depending on preparation methods and size of the aggregates [52]. C_{60}, along with the **A** and **C** series exhibited enhanced absorption in the visible range, and notably, C_{60}'s broad absorption peak centered about 500 nm is no longer lower than the corresponding peaks of the derivatives. The characteristic vibronic signal for C_{60} at 410 nm and 430 nm for **A1** and **C1** in toluene (Figure 4) disappears for the aggregates, due to fullerene-fullerene

interactions within the aggregates [132]. Interestingly, aggregates of **B** had significantly lower absorption in the UVA-visible range, despite being structurally very similar to **A**.

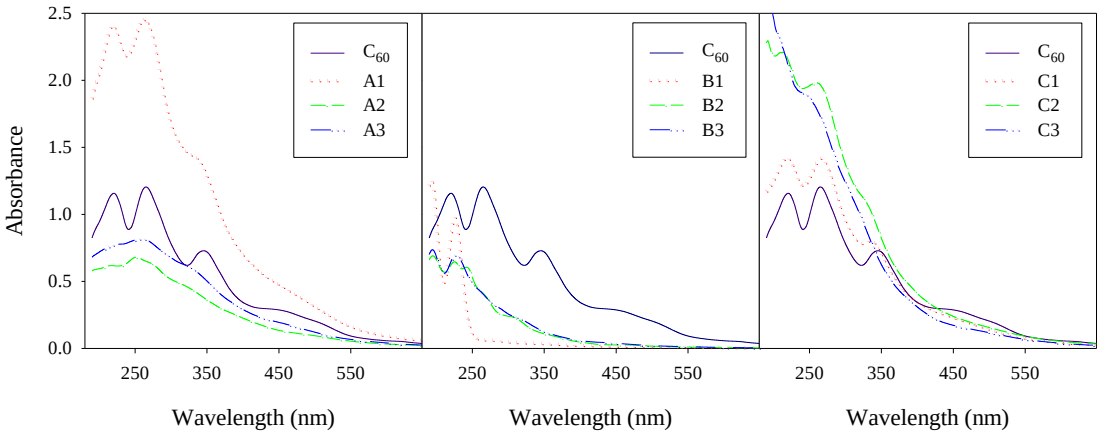

Figure 6: UV/Vis spectra for A, B and C as aqueous aggregates at 5 µM.

5.2.2. Aqueous Aggregate Photoactivity

FFA degradation experiments were performed using all aqueous aggregate samples with UVA radiation, yet only **B2** and **B3** exhibited significant $^1O_2$ production over the course of the photo-illumination , as seen in Figure 7 (data not shown for **A** and **C**, showing no degradation). Control experiments under dark conditions and with specific radical quenchers confirmed that FFA degradation was ascribed to the photochemical production of $^1O_2$. FFA degradation kinetics of **B2** and **B3** were not significantly different, as might be expected from their nearly identical UVA absorption spectra. The UV/Vis absorption spectra, however, do not fully explain the dearth of $^1O_2$ production in aggregates of other derivatives; in fact, the **B** series aggregates have lower absorption than **A**, **C** and C_{60} at wavelengths above 350 nm. The presence of a broad absorption

band from 400-600 nm in C_{60} and the **A** and **C** derivatives likely indicates C_{60}-C_{60} interactions [52]. The lack of this band in the **B** series suggests a difference in aggregation state, possibly with less molecule-molecule interactions within the aggregate. It is known that C_{60} aggregates are not effective for photosensitized $^1O_2$ production (compared to its molecularly dissolved counterpart), likely due to surface area limitations and self-quenching mechanisms, and it has been suggested that more soluble derivatives that either do not aggregate significantly or do not form crystalline aggregates are more capable of sensitizing $^1O_2$ in the aqueous phase [35, 36].

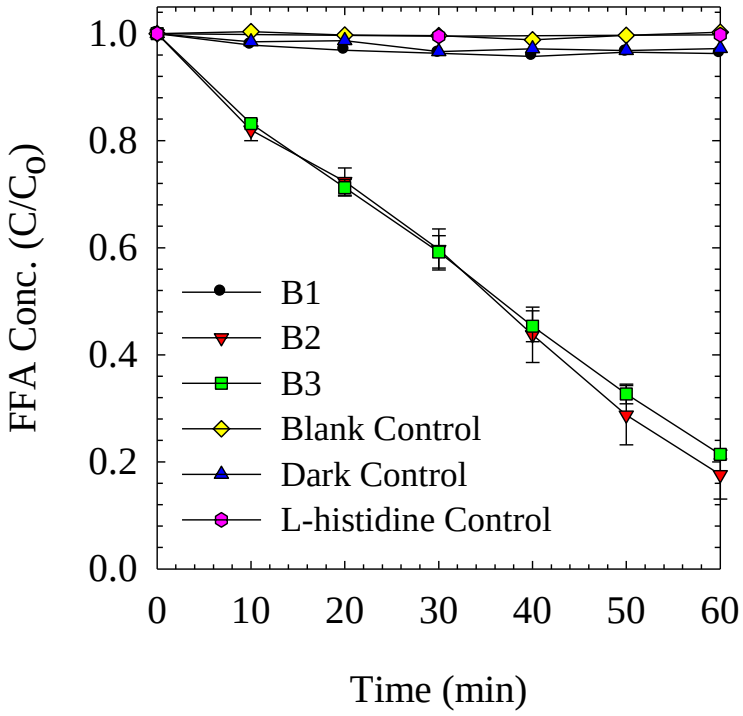

Figure 7: FFA degradation by the B series in the aqueous phase under BLB irradiation.

The presence of photoactivity in **B2** and **B3** aggregates and the lack thereof in other derivatives was confirmed using LFP experiments. Figure 8 compares the population of the triplet excited states of **B2** and **A1**, as examples of photoactive and non-photoactive derivatives, respectively. After the initial excitation pulse, a clear triplet state can be seen being populated at 650 nm for **B2**, with a corresponding decay of the singlet excited state observed at 510 nm. In contrast, **A1**'s triplet state, (probed at 700 nm due to a shifted triplet energy state) was rapidly quenched with a lifetime on the order of picoseconds. The singlet state of **A1**, probed at 550 nm formed and decayed on the same timescale as the triplet state (Figure 43). Probing **B2**'s triplet state 500 ns after the excitation pulse, Figure 9(a), revealed that its lifetime in an oxygen purged environment was long-lived compared to triplet **A1**. When monitored in the presence of O_2, however, **B2**'s triplet state was quenched within nanoseconds (Figure 9(b)). These results suggest that the lack of photoactivity in most of the derivatives can be attributed to a rapidly quenched triplet state, and that **B2** and **B3** aggregates do not undergo self-quenching pathways to the extent of other derivatives with the same number of addends. Previous studies showed that aggregated C_{60} has a triplet state that decays within picoseconds, compared with lifetimes of 50 to 150 μs when molecularly dispersed with surfactants or in benzene [10, 36].

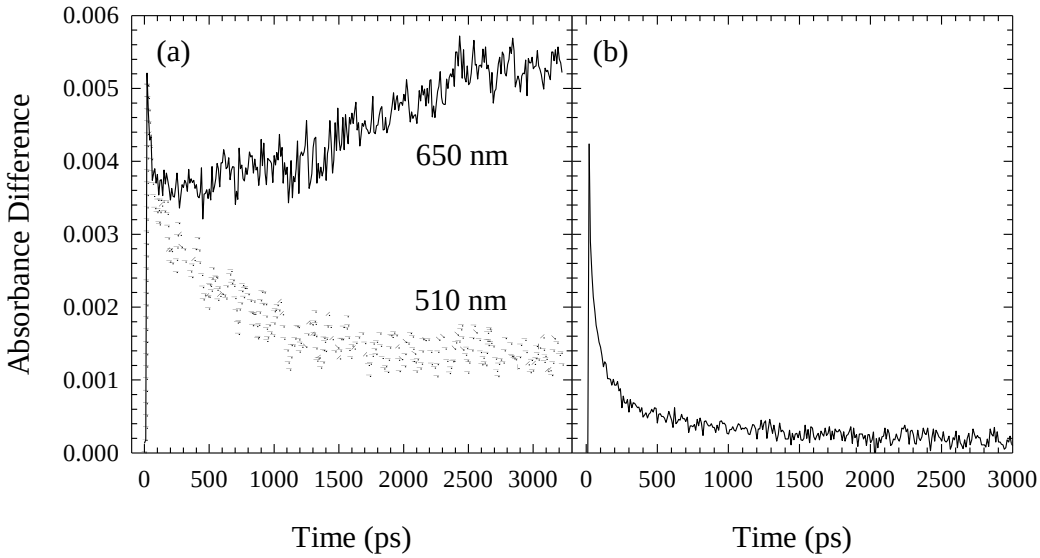

Figure 8: Absorption differences displaying triplet excited state populations probed with LFP for (a) **B2** at 650 nm (with the singlet population probed at 510 nm) and (b) **A1** at 700 nm.

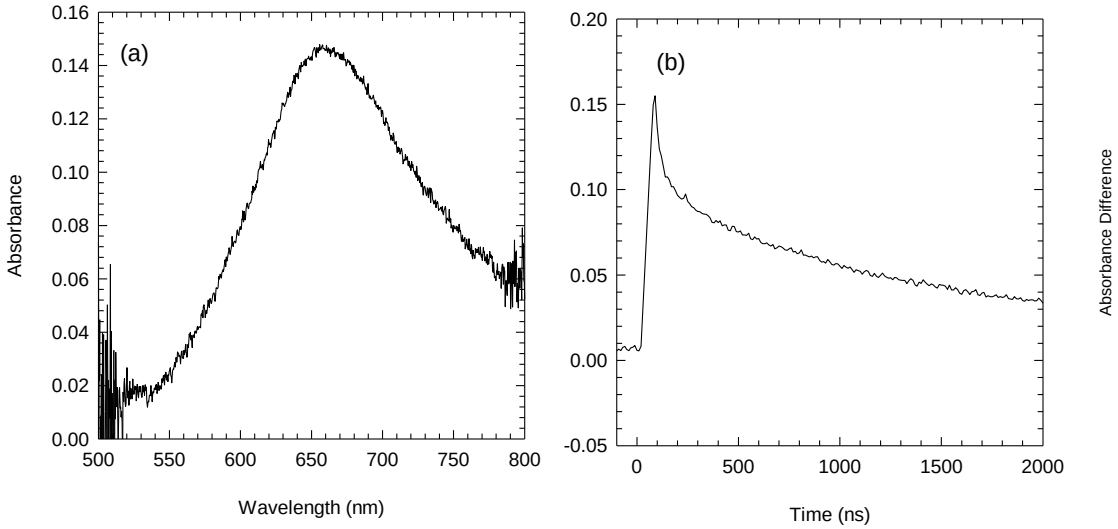

Figure 9: Nanosecond laser spectroscopy for **B2**: (a) triplet state absorbance 500 ns after laser excitation and (b) triplet state absorption difference at 650 nm in the presence of O_2.

5.3. Physical Characterization

5.3.1. Aggregate Size and Zeta Potential

Aggregates of each derivative were characterized and compared for size and ζ-potential. DLS analysis, as reported in Table 2 and Figure 10, found the aggregates to be highly polydisperse and to vary in size and ζ-potential. Less stable aggregates (with low absolute ζ-potential values under ca. 30 mV) increased in size with decreasing ζ-potential, as expected from colloidal physics. ζ-potentials of the aggregates had an expected correlation to the number of addends for the **B** series. With increasing addends for **B**, the zeta potential becomes more positive, starting at a negative value for **B1** (-16.9 mV). The negative ζ-potential of **B1**, indicates that one cationic charge does not stabilize C_{60} in water enough to counteract the hydroxylation, epoxidation and subsequent hydration that are suggested to be responsible for the negative surface charge [78, 135-137]. It is important to note that the size of aggregates did not matter for $^1O_2$ production in our study, as **B2** and **B3** degraded FFA at very similar rates, despite the significant difference in size. Additionally the **A** and **C** derivatives were not photoactive in the experimental timeframe, despite being similar or smaller in size than any of **B**. These findings contrast the often hypothesized surface-area limitation explanation for fullerene aggregates not producing significant amounts of $^1O_2$.

Table 2: Aggregate zeta potentials and sizes[a]

Sample	*ζ-Potential(mV)*	*d (nm)*	*w (nm)*	*PDI*
C60	-46.0	122.5	47.01	0.155
A1	-43.0	117.0	62.90	0.192
A2	-47.5	127.7	32.48	0.229
A3	-48.3	114.1	35.09	0.133
B1	-16.9	260.5	34.65	0.325
B2	+13.1	711.1	49.57	0.513
B3	+27.4	145.9	36.66	0.213
C1	-52.3	112.3	29.19	0.173
C2	-42.3	107.7	31.42	0.189
C3	-34.9	99.7	26.35	0.238

[a]All values are calculated from three or more repetitions. ζ is the zeta potential, *d* is the Z-Average diameter, *w* is the peak width and *PDI* is the polydispersity index.

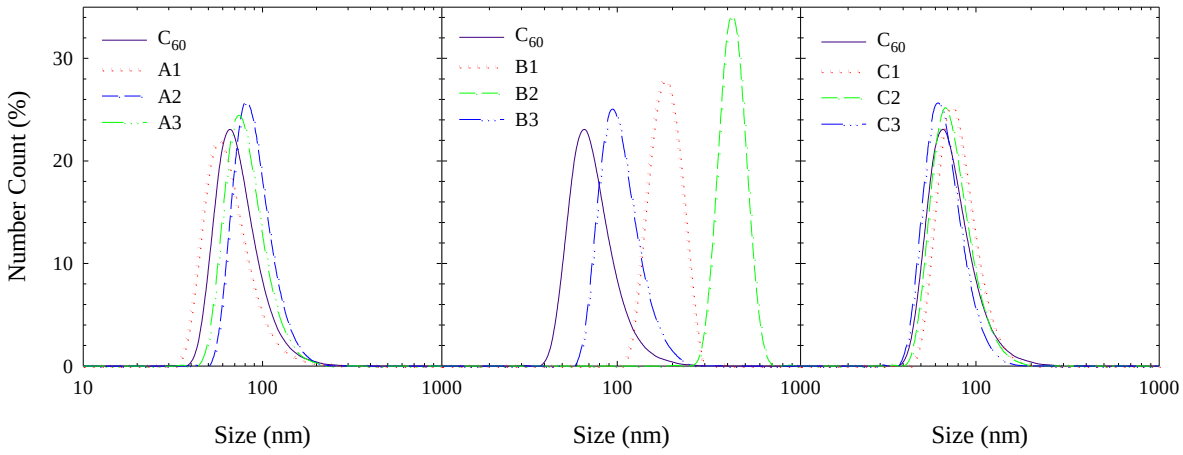

Figure 10: Aggregate size distributions for **A**, **B** and **C**.

5.3.2. Aggregate Crystallinity

TEM imaging confirmed the DLS size measurements, finding aggregates to be variable in size and shape, matching expected dimensions from DLS. Further, electron diffraction patterns were used to probe the crystallinity of the aggregates. Representative

TEM images with corresponding diffraction patterns are shown in Figure 11. Based on past hypotheses on the photoactivity of fullerene aggregates, it is expected that photoactivity of aggregates is mitigated by their crystalline nature, due to self-quenching mechanisms (*e.g.*, triplet-triplet annihilation) [28, 35, 36, 65, 138]. In line with the crystallinity hypotheses, C_{60}, **B1** and the **A** series were all found to have crystalline diffraction patterns, and **B2** and **B3**, which were definitively photoactive, were not crystalline. None of the **C** derivatives, however, were crystalline, suggesting that crystallinity does not fully explain the dearth of photoactivity in aggregates (diffraction patterns not shown). These data on the photoactivity and physical characteristics of the aggregates of fullerene derivatives puts many prior assumptions about the relationships between aggregation and $^1O_2$ production in question.

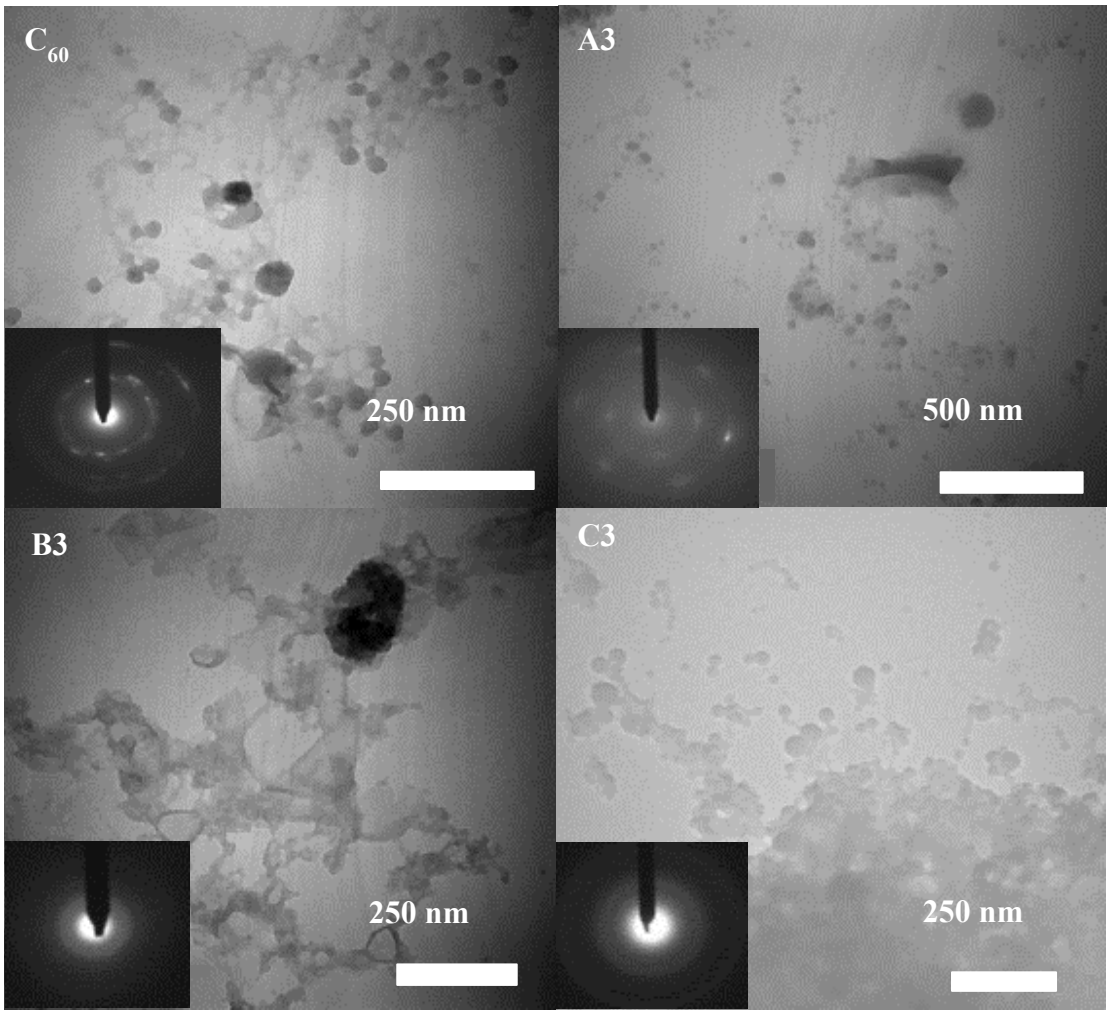

Figure 11: TEM and associated electron diffraction images for C_{60}, **A3**, **B3** and **C3**. Well-defined diffraction rings around the electron beam in C_{60} and **A3** indicate an ordered, crystalline structure.

5.4. Chemical Characterization

5.4.1. XPS Characterization

5.4.1.1. XPS Surveys

Aggregates of the **A** and **B** derivatives were dried and collected as a powder for XPS analysis. The chemical compositions of the aggregate powders were assayed to test for contaminations and to determine the amount of surface oxidation on the aggregates. Full elemental scans were performed and are recorded in Figure 44 in the Appendix. Chemical identities of peaks were defined and calculated for atomic percentages by the Advantage software package accompanying the instrument; these data are tabulated in

Table 3. Some silica contamination in the **A** series is immediately apparent and is likely responsible for the excessive oxygen content of n**A2**. It is noteworthy, however, that the Si-O ratios appear to be closer to a 1:1 ratio than what may be expected from contamination from glass or other minerals which would tend to have Si-O ratios of 1:2 or lower. If Si is assumed to have a 1:1 ratio with O, then all fullerenes are rather consistent in having compositions of 1 to 4% O as pristine fullerenes compared to the aggregates which had *ca*. 7 to 16% O. Nitrogen is seen in several samples, as would be expected by their functionalization. Iodine is also observed in **B3** as expected for the **B** derivatives. Sodium and Fluorine appear anomalously in n**A2** and both **B3** samples, respectively, also indicating contamination that could be from the use of glass containers.

Table 3: Elemental compositions from XPS scans as atomic percentages and carbon oxidation percentages of total carbon for pure fullerene powder and aggregated fullerenes.

Sample	O%	C%	Si%	N%	Na%	I%	F%	C-C%	O-C%	C=O%
C_{60}	1.02	98.98	0	0	0	0	0	93.09	6.91	0
nC_{60}	12.95	87.05	0	0	0	0	0	40.91	31.9	27.18
A1	9.16	83.02	7.04	0.78	0	0	0	96.61	3.39	0
nA1	7.10	92.90	0	0	0	0	0	48.47	38.98	12.55
A2	4.34	88.15	3.66	3.85	0	0	0	94.99	5.01	0
nA2	47.39	23.14	27.33	NA	2.14	0	0	61.39	28.4	10.22
A3	4.98	88.17	3.32	3.52	0	0	0	90.44	6.39	3.17
nA3	11.37	84.94	0	3.69	0	0	0	50.85	33.02	16.13
B2	3.72	96.12	0	0	0	0	0	82.87	17.13	0
nB2	16.71	83.29	0	0	0	0	0	60.12	28.44	11.44
B3	2.40	93.29	0	0	0	1.55	2.40	82.58	17.42	0
nB3	16.29	79.61	0	0	0	0	4.10	73.53	20.01	6.46

5.4.1.2. XPS C1s Scans

In addition to the coarse survey scans, the C1s peak occurring at approximately 285 eV was closely examined for the presence of chemical shifts due to oxygen functionalization of the carbon cages. C1s scans and their resolved peaks, by Gaussian-Lorentzian computations with a fixed fwhm, are shown in Figure 12 and Figure 13. The peak at 284.5 eV is attributed to C-C bonds which are prevalent in the fullerene cage. Peaks shifted by 1-2 eV higher in energy can be generally labeled as C-O bonds, while peaks in the 288 to 291 range can be assigned as di-oxygenated bonds (*e.g.*, C=O or O-C-O groups) [78, 139, 140]. The broad signal spanning about four eV beginning six eV higher than the C-C peak corresponds to the π- π^* shakeup from the presence of significant aromaticity in the fullerenes [141, 142]. Notably, the n**B2** peaks are shifted higher in energy, which is attributed to a charging effect that was also observed in the O1s peak as described in the following section. The percentages of total carbon oxidized by one or two oxygen bonds are listed in

Table 3 with the total elemental compositions. In general, the quantities of oxidation observed for the pristine versus aggregated fullerenes are consistent with reports in the literature [73, 78, 79, 139, 140]. The significant presence of oxygen functionalization suggests that the aggregation method employed chemically alters the fullerenes as they aggregate. This oxidation is likely part of the reason for the negative charge on the non-ionic fullerene aggregates. It is also worth noting that other methods of aggregate preparation have yielded much lower oxygen functionalization, particularly for cases prepared with stirring only or in dark conditions [73, 90].

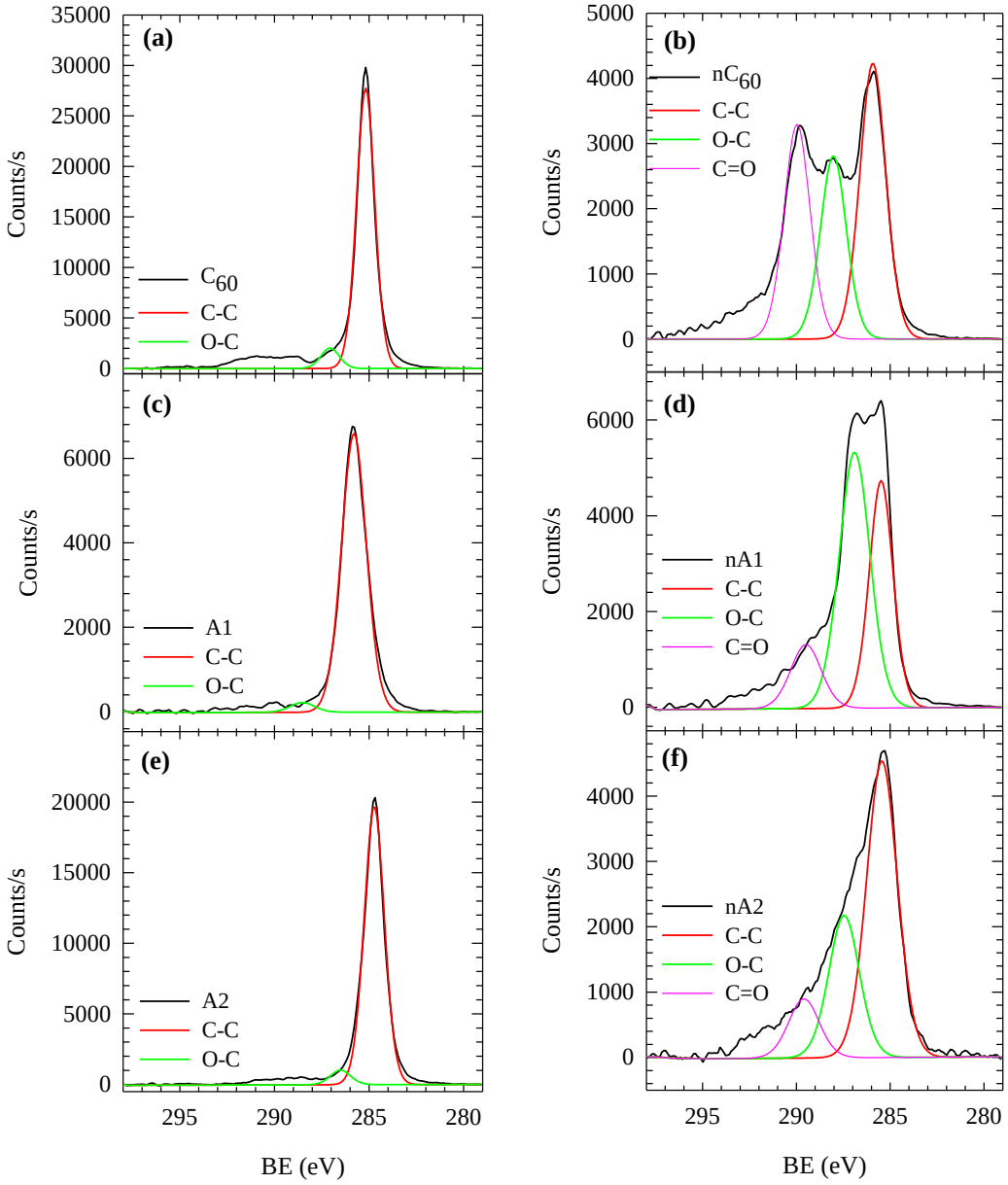

Figure 12: C1s scans with fitted peaks for (a) C_{60}, (b) nC_{60}, (c) **A1**, (d) n**A1**, (e) **A2**, and (f) n**A2**.

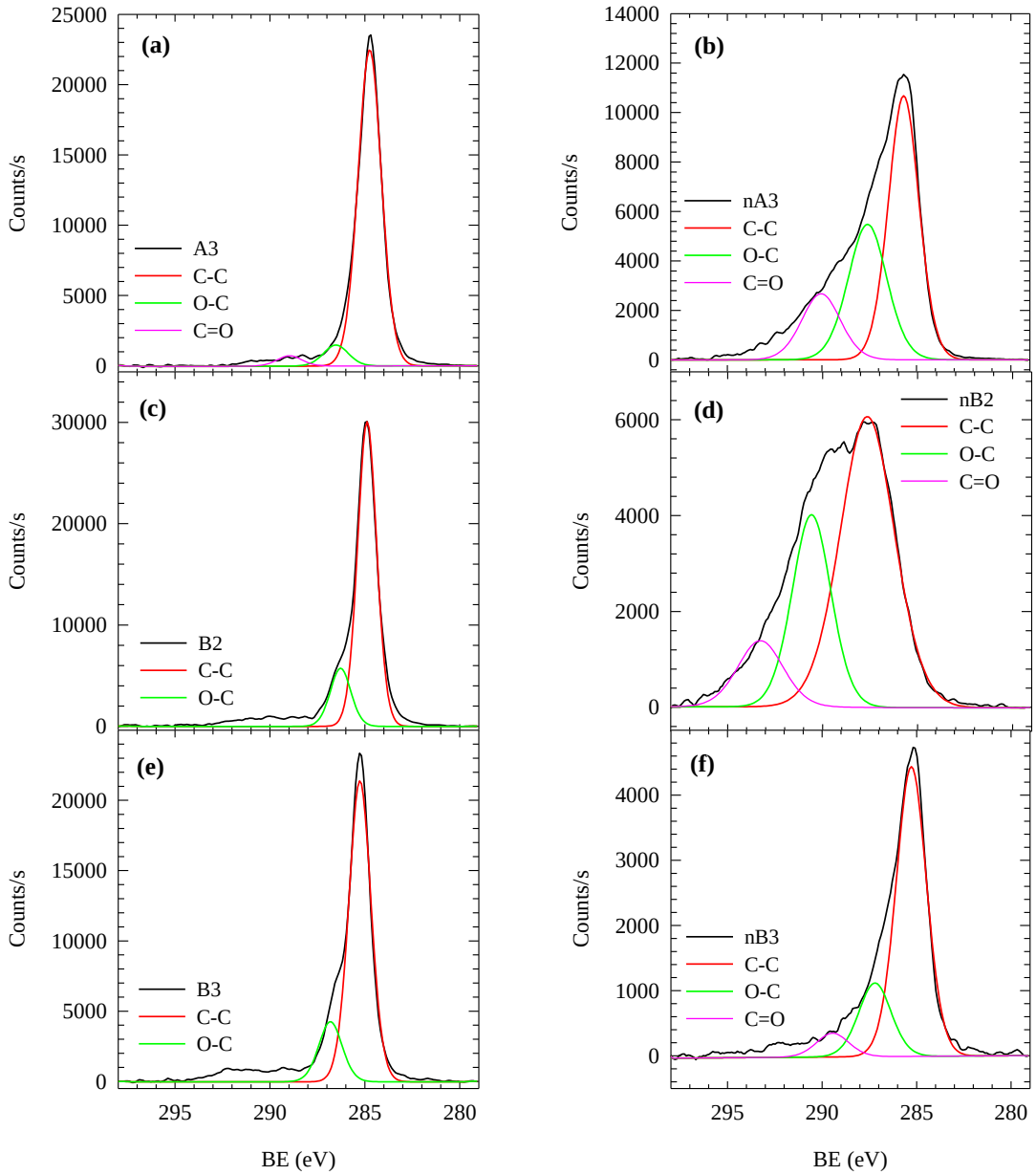

Figure 13: C1s scans with fitted peaks for (a) A3, (b) nA3, (c) **B2**, (d) n**B2**, (e) **B3**, and (f) n**B3**.

5.4.1.3. XPS O1s Scans

To complement the C1s scans and the elemental analysis from the survey scans, O1s scans were also performed with high resolution to examine any chemical shifts present. The O1s scans are presented in Figure 14, but individual peaks were not resolved, due to the complicated nature of O1s peaks and the many overlapping signals. The n**B2** signal is clearly shifted higher in energy compared to other O1s signals, as an artifact of a charging phenomenon discussed in the context of the C1s peaks. A strong signal is observed from the n**A2** scan, which is attributed to the presence of significant Si-O contamination. Overall, the fullerenes exhibited higher O1s peaks after aggregation, with particular increase in signal in the binding energy (BE) range of 1-2 eV above the peak of the pristine fullerenes. The peak in the pristine fullerenes is centered at *ca*. 532 eV which aligns well with organic C-O bonds, and the increase in signal in the 533-534 range is indicative of organic C=O bonds [142], supporting the analysis from the C1s peaks. This increase and shifting in BE for the O1s peak has been reported previously for nC_{60}, particularly for cases of nC_{60} formation under light and oxic conditions [90]. While the presence of C-O and C=O functional groups have been evidenced for the aggregated fullerenes, contamination from adsorbed O_2 or CO_2 may have contributed to the peaks, which would help explain the O1s signals for the pristine cases. Another explanation for the oxidation of the pristine fullerenes, however, could be oxidation of the fullerite powder by ambient ozone, as recently suggested by Murdianti *et al*. [135]. Another important note is the ratio of O to C in the aggregate scans. While a high percentage of carbon atoms experience shifts in BE for their C1s electrons, it is not likely that a full 26 % of carbon is oxidized in the n**B3** case. It is doubtful even that the apparent 16 % oxygen

observed in n**B3** all comes from functionalized carbon, because the fullerenes retain a significant portion of their photochemical character that arises from their highly π-conjugated chromosphere. It is possible, then, that water molecules are trapped within the aggregates during the aggregation process, increasing the O1s signal.

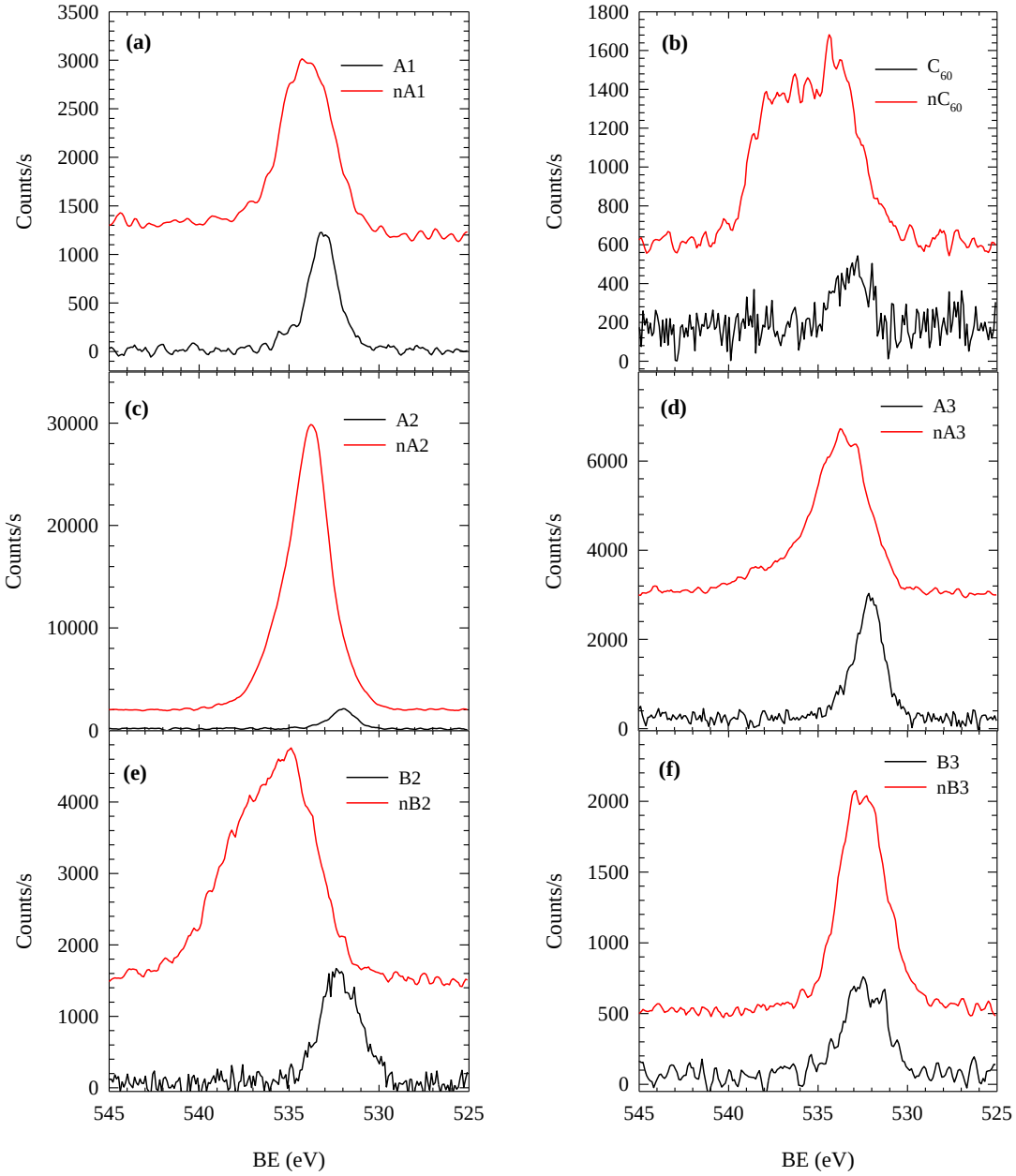

Figure 14: O1s peaks for (a) C_{60}, (b) **A1** (c) **A2**, (d) **A3**, (e) **B2**, and (f) **B3**

5.4.2. FTIR Characterization

To further probe and confirm the findings of the XPS analysis of the fullerenes and their respective aggregates, ATR-FTIR was used. The spectra for C_{60}, the **A**, and **B** fullerenes and their aggregates are shown in Figure 15. The observed peaks in the spectra generally match well with reports in the literature. Pristine C_{60} exhibits expected peaks at 1,430 and 1,180 cm^{-1}, consistent with known C-C vibrational peaks [78, 82, 90, 139, 143]. Upon aggregation, several new peaks are present for nC_{60}: a broad band centered at 1,000 cm^{-1} is indicative of a mixture of C-O bonds [78, 82, 139]. A peak at 1,710 cm^{-1} indicates the presence of carbonyl (C=O) bonds. Further, there is a minor peak centered at 2,900 cm^{-1}, which indicates C-H bonds likely formed when O groups were added to C=C bonds [78, 82], and a broad signal between 3,200 and 3,600, consistent with O-H stretching from water or alcohol groups [78, 82, 139]. These changes in FTIR spectra appear to be consistent across the various functionalized fullerenes. Each case shows an increase in and broadening of signal around the 1,000 and 1710 cm^{-1} regions. One notable feature is n**A2**'s large signal centered at *ca*. 1150 cm^{-1}, which is known to be a Si-O stretching band [144], as expected from the noted Si-O contamination observed in the XPS analyses. C-H stretching bands are observed for all **A** and **B** derivatives as pristine fullerenes, as expected given the presence of C-H groups in their structure. Interestingly, these bands are barely observed in the aggregates of the **B** derivatives, possibly indicating that these H groups are substituted during the functionalization process during aggregation. Overall these results confirm the suspected oxidation of the fullerene aggregates observed in the XPS analyses. The significant increase of signal in the 3,200 to 3,600 cm^{-1} range also points to the possibility of trapped H_2O molecules within the aggregates. Given that all

fullerenes appear to undergo similar functionalization by various oxygen groups during the aggregation process, it can be inferred that the nature of aggregate formation is not responsible for the discrepancy in photoactivities between the **B** derivatives and all others compared. While it is known that intense UV irradiation or ozonation effectively oxidize nC_{60}, resulting in more hydrophilic suspensions that are photoactive in water [48, 79], the present results suggest that other mechanisms drive the photoactivity (or lack thereof) in the derivatives studied here.

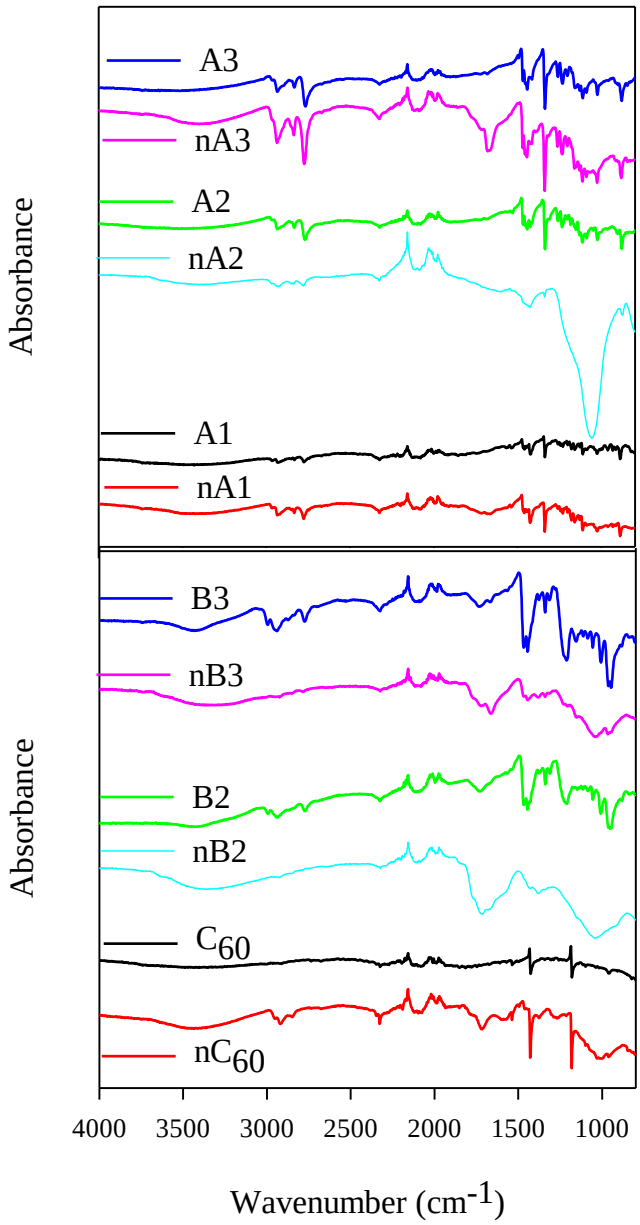

Figure 15: ATR-FTIR spectra for C_{60}, **A**, and **B** derivatives and their aggregates in KBr pellets.

6. ANTIMICROBIAL PROPERTIES OF FUNCTIONALIZED FULLERENES

With thorough characterization of the functionalized fullerenes, assessment of their antimicrobial properties is expedient to understanding the relationships between functionalization and aqueous (photo)biological properties. This chapter effectively tests and provides evidence towards hypothesis four in section 1.4. Size fractionation experiments were also performed on the photoactive **B2** and **B3** derivatives specifically to test the antimicrobial properties for size dependency, providing further examination of hypotheses three in section 1.4.

6.1. Effects of Size and Particle Interactions on Antimicrobial Interactions

6.1.1. Characterization of Size Fractionated Aggregates

Size fractionation via membrane filtration was performed successful for both **B2** and **B3** derivatives. The concentrations of permeate solutions, recorded in Table 4, were determined using UV/Vis absorption, with spectra for each size fraction shown in Figure 45 in the Appendix. With the exception of the 30 kDa fraction of **B2**, the spectral structures were consistent across size fractions, indicating that the fullerenes existed as aggregates in each size regime. The spectra for the 30 kDa fraction of **B2** closely resembled those of the **B3** peaks, possibly indicating the small presence of **B3** in the **B2** sample allowed a small fraction of the solution to form smaller particles containing primarily **B3** and pass through the 30 kDa membrane. This observation is in line with the known purity of the sample: **B2** containing small amounts of **B3** and vice versa, and it is notable that the **B2** and **B3** appeared to have segregated to some degree in solution [63].

For both **B2** and **B3**, nearly all particles passed through both the 0.45 and 0.22 μm membranes. While **B3** particles effectively passed through a 30 kDa membrane, **B2** had a higher yield of particles through the 300 kDa membrane. The 30 kDa permeate fractions reveal that **B3** aggregates may be loose compared with **B2**, breaking apart into smaller pieces or individual molecules, passing through the membrane, and re-aggregating in the permeate solution.

Table 4: Concentrations of size fractionated solutions.

Sample	*Concentration (µM)*	*Fraction of Total (%)*	*Approximate pore size (nm)*[a]
B2 0.45 µm	22.28	100	450
B2 0.22 µm	22.43	100	220
B2 300 kDa	17.86	80.2	35
B2 30 kDa	1.37	6.1	< 5
B3 0.45 µm	19.27	94.8	450
B3 0.22 µm	19.97	98.2	220
B3 300 kDa	13.82	68.0	35
B3 30 kDa	8.57	42.2	< 5

[a] Values for kDa membranes are approximate nominal pore sizes.

DLS revealed that fractionation did segregate particles with into variable sizes as seen in Figure 16, but also reveals that re-aggregation occurs for small, unstable particles. Both 30 kDa samples were not stable enough to measure, indicating re-aggregation occurring. The 300 kDa samples also exhibited some inconsistency and measurement errors during sample analysis, further demonstrating the instability of the smaller aggregates. Aggregates passed through a typical filter, with a 0.22 or 0.45 μm membrane, were comparable to typical nC_{60} aggregates. The presence of smaller particles in the **B** derivatives after passing through a 300 kDa membrane, particularly **B3**, suggests that the

large particles may actually be agglomerations of aggregates that are 20 or 40 nm in diameter for **B3** and **B2**, respectively. The distribution for the 300 kDa **B2** sample was bimodal, further indicating the presence of smaller, sub-aggregates undergoing re-aggregation post-filtration. Photochemical degradation of FFA was also recorded for the various size fractions of **B2** and **B3**, as seen in Figure 17. Consistent with previous results [63], **B2** out performed **B3** in $^1O_2$ production. Both samples exhibited subtle trends of increasing degradation kinetics with decreasing particle size, likely due to increased surface area for $^1O_2$ sensitization. It is notable that a shift of *ca*. 80 nm in average particle diameter resulted in only a very minor change in observed $^1O_2$ production, contrary to a common notion that fullerene aggregates are photochemically limited by surface area.

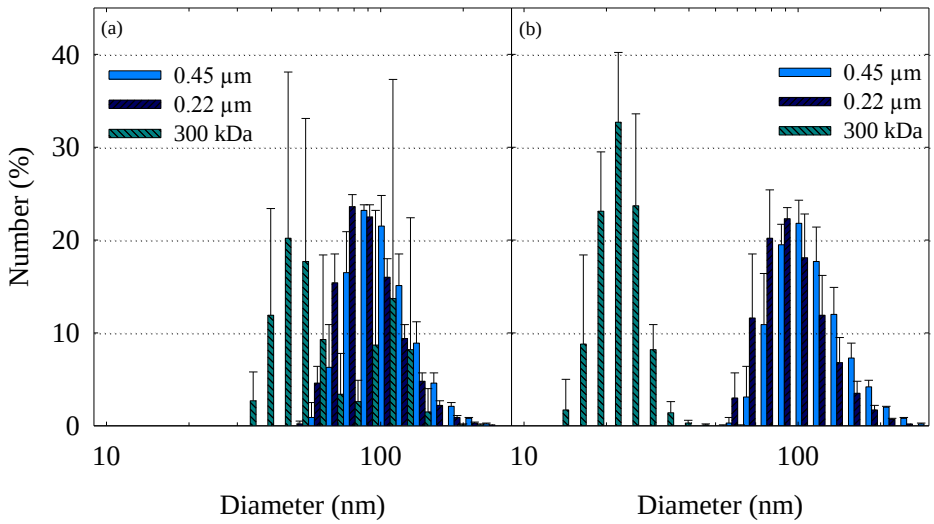

Figure 16: Number-weighted particle counts by diameter, measured with DLS for (a) **B2** and (b) **B3**. Error bars are the standard deviation of measurements.

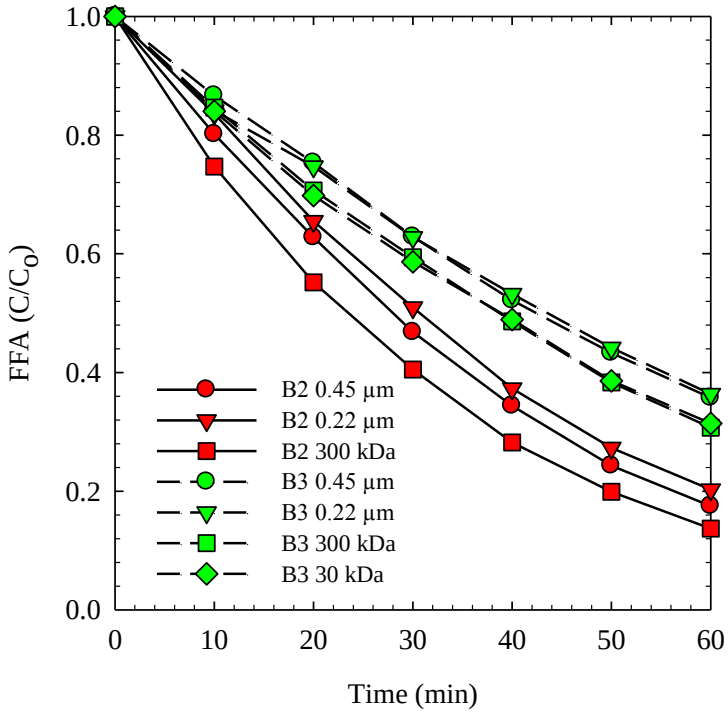

Figure 17: FFA degradation by various size fractions of **B2** and **B3** at 5 μM.

6.1.2. Particle-Microbe Interactions

The interactions between fullerene aggregates and MS2 were probed with DLS, reported in Figure 18. Note that intensity weighted measurements are reported here to identify the presence of particles with largely variable sizes; the distributions represent the presence, not quantity of the given size particles. Measurements of viruses alone found them to be at *ca*. 35 nm, while aggregates sizes ranged from 50 to 300 nm, depending on the derivative, and had highly polydisperse distributions. Samples of **A** and **B** derivatives were used to probe the interactions of the viruses and differentially charged aggregates. Analysis of the cases of **A2** and **A3** with MS2 revealed that the distributions were extended to include the virus particles in addition to the aggregates in solution. In

contrast, the **B** aggregates with MS2 had a bimodal size distribution, revealing some mono-dispersed virus particles at 40 nm and other agglomerations of MS2 and **B2** or **B3** at ca. 200 or 450 nm, respectively. In the **B2** with MS2 case, the intensity of signal for particles in the range of **B2** aggregates was very low. Similarly, no **B3** aggregates were apparent by themselves, suggesting that the virus particles may have acted as a binding agent to enhance agglomeration of the **B** aggregates, due to electrostatic attraction (zeta potential of MS2 = -55.4 mV [43] and **B3** = +27.4 mV [63]) as a major driving force.. A previous report analyzed the effect of proximity on various fullerene aggregates' abilities to inactive MS2 and provided evidence for higher inactivation rates with closer particle-virus interactions [64]. Based on the apparent, direct association of **B2** and **B3** aggregates with MS2, effective MS2 inactivation is expected.

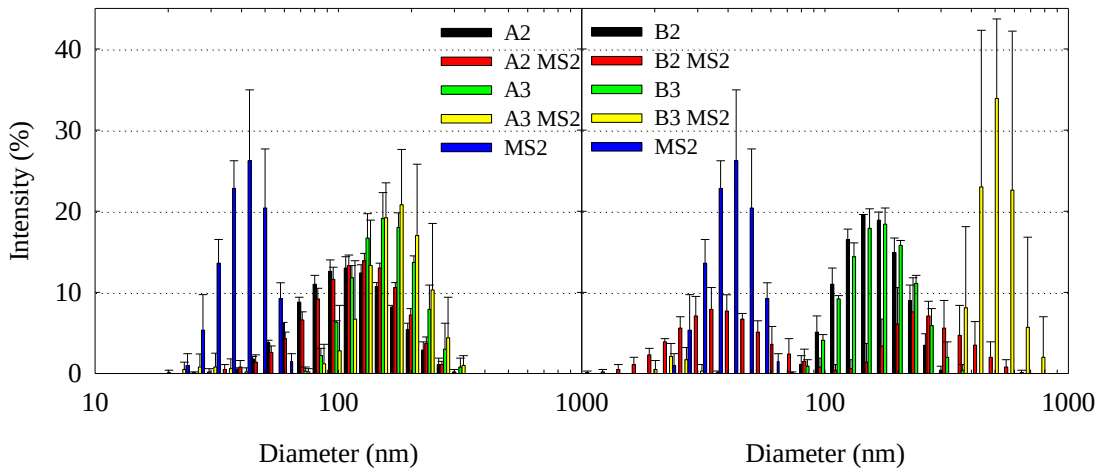

Figure 18: DLS intensity-weighted size distributions for **A2**, **A3**, **B2**, and **B3** with MS2 virus in a 10 mM PBS solution at pH 7.2.

6.1.3. Innate Toxicity of Functionalized Fullerenes

Toxicity of fullerene aggregates towards *E. coli* under dark conditions was probed using an MIC test. Inhibitive concentrations showed that only **B** derivatives were toxic under concentrations of fullerene aggregates reasonably attainable as colloidal suspensions: the fullerenes inhibited growth at 0.2, 0.3, and 0.5 μM for **B1**, **B2**, and **B3** respectively. The toxicity of the **B** series was in line with well-documented effects of quaternary ammonium groups as a class of molecules [145] as well as prior studies of cationic-functionalized C_{60} [43, 45, 47, 65-67]. Inhibitory concentrations for all non-cationic fullerenes studied here did not inhibit growth at concentrations up to 20 μM. The upper limit of concentrations for C_{60}, **A**, and **C** aggregates were limited by solution stability; concentrations of 400 μM as reported in Lee *et al*., were obtained using highly water soluble derivatives and were not possible for our derivatives [65]. Given that highly soluble derivatives do not exert toxicity up to 400 μM, it is reasonable to presume that the **A** and **C** derivatives, which were not toxic up to 20 μM, would also have an MIC unattainable in any realistic environment. MIC for **B2** and **B3** did not vary under different size regimes (data not shown), suggesting that size effects do not drive the toxicity mechanism. Although variations between **B** derivatives was too small to establish a meaningful trend, it is interesting that **B1** exerted toxic effects even though aggregates tended to be highly unstable in solution due to surface charge effects [63].

6.2. Photoinactivation of *E. coli*

All derivatives were tested for photoactivity towards *E. coli*. As expected given their previously reported photoactivities [63], only **B2** and **B3** were found to have activity towards bacteria under UVA irradiation at 5 μM, as plotted in Figure 19. No size-dependent differences were apparent for inactivation experiments when performed for the various size fractions of **B2** and **B3** aggregates. Size fraction data were, therefore, averaged and error bars show the standard error of the experiments. Inactivation data for **A** and **C** derivatives as well as control experiments are shown in Figure 46 in the Appendix. **B2** exhibited faster inactivation, with a 2-log kill in 40 minutes, compared to 60 minutes for **B3**, corresponding to the fact that **B2** also sensitized $^1O_2$ more efficiently. The lack of size-dependency on inactivation and the correspondence to $^1O_2$ production capacity suggest that either inactivation did not rely on the aggregates penetrating into the bacterial cell or that the differences in sizes in these regimes had no significant effect on cell penetration, an interesting topic for further investigation. The presence of a lag phase during the first 30 minutes of the experiments before inactivation began could be indicative of either the time required for aggregates to penetrate into the cell, or alternatively, the time it takes for the sensitized $^1O_2$ to degrade the cell membrane before inactivating the bacteria. An intriguing observation was made while conducting these experiments: bacterial colonies that grew on the samples after the lag phase were consistently smaller in diameter than those of controls or from initial time points. This qualitative observation likely has some implication concerning the ability for cells to repair and replicate and could warrant further investigation.

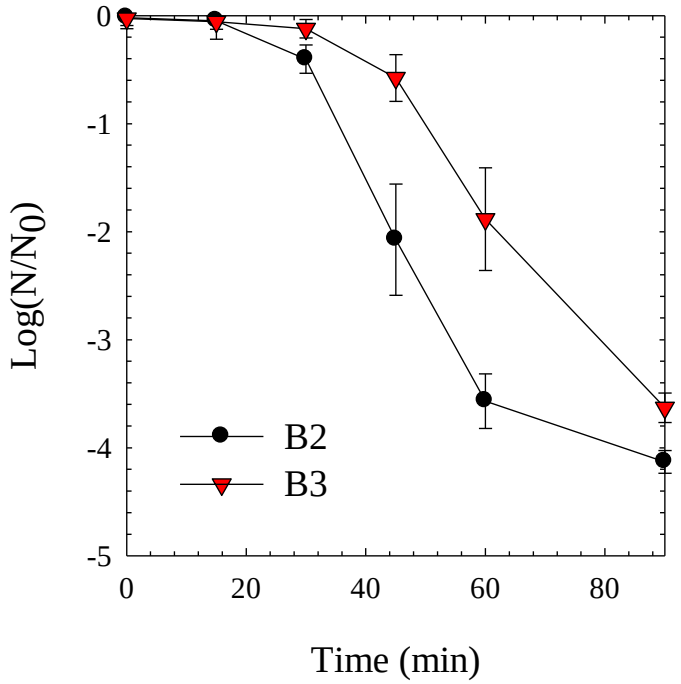

Figure 19: *E. coli* inactivation by combined size fractions of **B2** and **B3** at 5 μM under UVA light.

6.3. Photochemical Inactivation of MS2 Bacteriophage

6.3.1. Effects of Particle Size

Photo-inactivation experiments were performed on all derivatives with MS2 under visible or UVA light. Rapid degradation and inactivation of the viruses was observed for **B2** and **B3**. Parallel to the *E. coli* case, other derivatives that did not exhibit photoactivity did not exhibit viral inactivation under experimental conditions, as seen in Figure 47 in the Appendix. MS2 inactivation by size fractionated **B2** and **B3** aggregates, plotted in Figure 20, was remarkably rapid given the relatively low concentration and light intensity compared with the *E. coli* case or with other reports (as discussed in the

following sections). The **B3** aggregates exhibit no clear trend in size-dependent photoactivity, with all four sizes achieving approximately the same level of inactivation after 80 seconds. **B2** particles, however, were more variable in inactivation rates, with the smallest particles having the most rapid inactivation, on par with the **B3** particles. The variability between the 0.22 and 0.45 μm **B2** particles is surprising, given their similar sizes documented in Figure 16. Overall, it seems that particle size is not a significant factor in the ability for the fullerenes to produce $^1O_2$ and subsequently inactivate MS2.

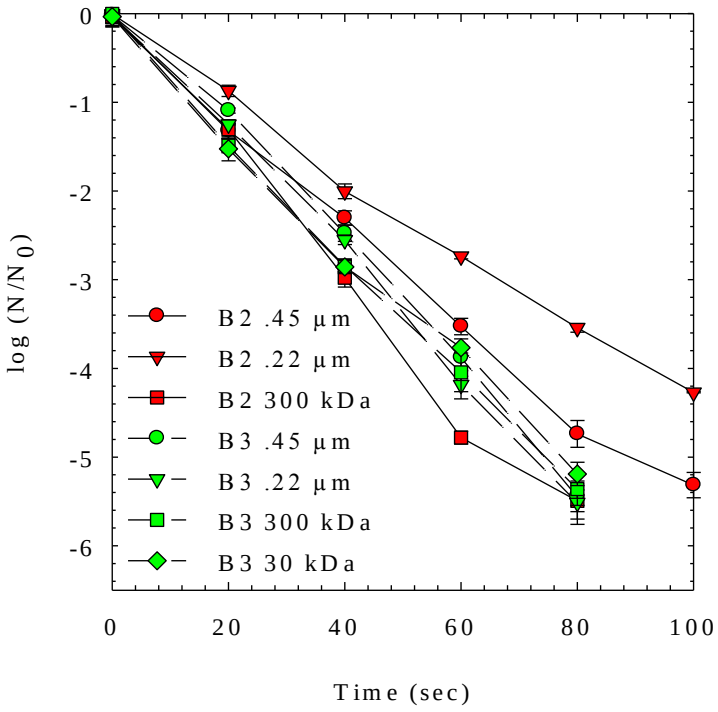

Figure 20: MS2 Bacteriophage inactivation by **B2** and **B3** aggregates by particle size.

6.3.2. Light and Concentration Dependence of MS2 Inactivation

Photoinactivation of MS2 by **B3** under visible irradiation exhibited an extremely fast kinetics; e.g., 5-log (99.999%) inactivation by 1 μM in less than 2 min as seen in

Figure 21. Dark control experiments showed no virus loss (i.e., viruses that associate with agglomerates can be still counted as an individual plaque during plate analysis), confirming that the adsorption alone does not contribute to inactivation observed in these experiments. A clear concentration dependency was observed from 100 to 1,000 nM, with a 2-log inactivation achieved after 5 min with 100 nM. No significant inactivation was observed for both 10 and 50 nM over 2 h. When low concentration suspensions were exposed to the UVA irradiation instead of visible light, efficient inactivation was observed, with an exceptional 4-log kill in 4 min by 50 nM. The inactivation for 10 nM under UVA was also increased, but plateaued at 2 logs after *ca*. 20 min. It is remarkable that **B3** achieved a 2-log within tens of min at 10 nM, or *ca*. 9 μg/L. As a reference, a recent study reported that wastewater NOM, a known $^1O_2$ sensitizer, achieves a 2-log MS2 inactivation at the mg/L range under UVB light after 12 h [146].

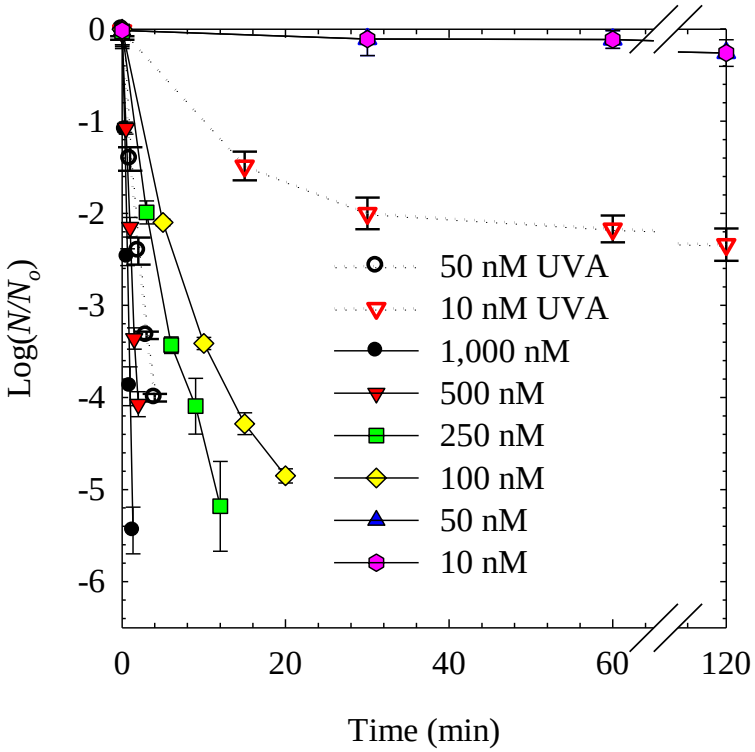

Figure 21: Concentration dependence of MS2 inactivation by **B3** aggregates under visible or UVA irradiation in 10 mM PBS at pH 7.2, 25 ^{o}C.

Extremely efficient viral inactivation necessitates the questions of efficiency in environmentally relevant conditions. Figure 22 displays the results from experiments conducted under sunlight with 250 nM **B3** with and without 5 mg/L NOM. Experiments were performed on the 4th and 12th of September, 2013. On both days experiments were conducted between 1:00 and 1:30 pm EST, the ambient temperature was measured at 36 ^{o}C, the blue light intensity averaged *ca*. 2.8 mW/cm^2 and the UVA intensity averaged *ca*. 1.0 mW/cm^2. The maximum UVA intensity reached a high mark of 1.20 and 1.01 mW/cm^2 on the 4th and 12th, respectively. Remarkably, a 2-log inactivation was almost immediately observed, even though the first sample was withdrawn within less than 5 s

after addition of viruses. The same rapid loss of MS2 was also observed in the laboratory, but only when **B3** concentrations were extremely high. Control experiments confirmed that this MS2 loss occurred only when the sample was exposed to sunlight with **B3** (i.e., no loss due to adsorption to **B3** or vessel). The inactivation of MS2 with 250 nM **B3** with NOM was slightly slower than in PBS, likely due to a quenching or protective effect by NOM [147] or possibly from subtle variation of light conditions on experimental days. NOM can play a role in the sensitization of $^1O_2$ and inactivation of viruses [146], but NOM's contribution to $^1O_2$-mediated MS2 inactivation would be too minor to be observed, given the brief experimental window. Light attenuation by the NOM is not likely significant, given the shallow depth (3.5 mm) of the reaction solution during experimentation. Even taking NOM effects into consideration, **B3** appears to be highly photochemically active under environmentally relevant conditions and at sub-micromolar concentrations.

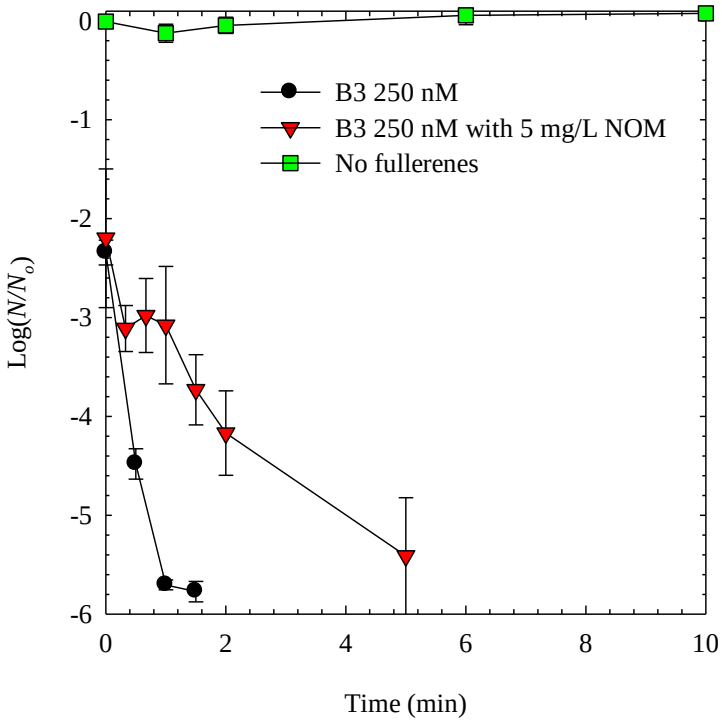

Figure 22: MS2 inactivation by 250 nM **B3** under sunlight, with and without 5 mg/L NOM (10 mM PBS, pH 7.2, 36 ^{o}C).

6.3.3. Singlet Oxygen as the Dominant Inactivation Agent

Control experiments suggest that $^1O_2$ is the dominant inactivating agent by **B3** as well as for **B2**, a derivative with one less methyl pyrrolidinium group than **B3** and slightly slower MS2 inactivation kinetics (Figure 48). Excess L-histidine (250 mM) as $^1O_2$ scavenger reduced the inactivation rates of **B3** and **B2** from k_{obs} = 3.95 and 3.37 to 1.17 and 0.433 min^{-1}, respectively ($k_{\text{L-histidine}}/k_{obs}$ ratios = 0.3 and 0.13 for **B3** and **B2**). As a comparison, $k_{\text{L-histidine}}/k_{obs}$ ratios of 0.57 [146] and 0.76 [148] have been reported when $^1O_2$ plays a dominant role in MS2 inactivation. The presence of SOD (30 mM), a commonly employed $\bullet O_2^-$ scavenger, also inhibited MS2 inactivation by B3 (k_{SOD}/k_{obs} =

0.32). But the $\bullet O_2^-$ production rate by 5 μM **B3** under UVA was very low and determined to be 0.02 or 0.06 μM/min, measured using nitro blue tetrazolium (NBT^{2+}) [35] or XTT (2,3-bis(2-methoxy-4-nitro-5-sulfophenyl)-2*H*-tetrazolium-5-carboxanilide salt) [116] with or without dimethylaniline (DMA) [117] as an electron donor (Figure 49), after calibration according to Lee *et al* [35]. Accounting for the **B3** concentration difference, the actual $\bullet O_2^-$ produced during the inactivation experiments is estimated to be on the order of 10^{-10} M/min, whereas $^1O_2$ production is estimated to have a steady state concentration on the order of 10^{-11} M, as discussed below. This observation, combined with the fact that *tert*-butanol (30 mM) as a •OH scavenger did not reduced the inactivation rate, rules out •OH and $\bullet O_2^-$ as oxidants responsible for MS2 inactivation. It should be noted that SOD is also an efficient $^1O_2$ quencher (2.7×10^9 $L\cdot mol^{-1}\cdot s^{-1}$), even compared with L-histidine (3×10^7 $L\cdot mol^{-1}\cdot s^{-1}$), explaining the reduced MS2 inactivation in the SOD control [149]. MS2 inactivation with other derivatives, which were shown to be incapable of producing $^1O_2$ [63], yielded no inactivation (Figure 50).

The fact that **B3** and **B2** exerted *ca*. 4 log *E. coli* inactivation after 90 min of UVA irradiation while other, non-cationic derivatives exhibited no observable inactivation (Figure 19Figure 46), matched the lack of $^1O_2$ production observed in Figure 7 [63]. The MS2 consists of a protein capsid that acts as a protective shell to the genomic RNA [150]; this structure is much more vulnerable to $^1O_2$, which is selective towards proteins compared to the lipid membrane of *E. coli* [151]. These controls and results collectively support that photochemically produced $^1O_2$ was responsible for viral inactivation.

6.3.4. Quantitation of Photo-Induced Inactivation by Fullerenes.

The inactivation kinetics were plotted against *CT* (concentration of disinfecting agent ($^1O_2$) × exposure time) in Figure 23 to compare the kinetics of $^1O_2$ inactivation obtained in this study with previously reported kinetics. The $[^1O_2]_{ss}$ was calculated to be 1.01×10^{-8} and 7.63×10^{-9} mg/L from the kinetics of FFA degradation for **B3** at 5 and 1 μM under visible and UVA light, respectively, as seen in Figure 51. Examining the data from experiments in the FL reactor, points are scattered along a reasonably correlated trend line (R^2 = 0.865). The linear regression includes only data from the linear portion of FL experiments. A linear relationship between sensitizer concentration and $^1O_2$ production, as demonstrated previously [43], was assumed in order to calculate $[^1O_2]_{ss}$ at very low **B3** concentrations when it was impossible to quantify FFA degradation. Accordingly, a 2-log inactivation corresponds to a *CT* of 1.21×10^{-9} mg-min/L, which is markedly smaller than previously reported $^1O_2$-*CT* by cationic aminofullerenes at 6.4×10^{-5} mg-min/L [43]. Our *CT* value is also lower than other $^1O_2$-*CT* estimations in other systems but only by an order of magnitude; Badireddy *et al*. reported a *CT* of 1.27×10^{-8} mg-min/L for several fullerenes for 2-log MS2 inactivation, and 2.25×10^{-8} mg-min/L was calculated from Kohn *et al.*'s reported $[^1O_2]_{ss}$ [64, 146]. Rose Bengal (RB) is another well-known $^1O_2$ sensitizer that has recently been studied for MS2 inactivation. Rosado-Lausell, *et al*. reported RB at 0.5 μM to have a k_{obs} of 0.076 min^{-1} which corresponds to a 2-log *CT* of 3.07×10^{-7} mg-min/L, while **B3** at 0.5 μM had a k_{obs} of 2.12 min^{-1} [148]. On a molar basis **B3** outperforms RB significantly.

Strong association between MS2 and **B3** further contributed to enhanced inactivation kinetics [64]. Dynamic light scattering (DLS) analysis suggests that **B3** agglomerated with MS2 (*ca*. 30 nm), shifting average sizes from 150 to 600 nm, with a

surprising disappearance of signal in the range of the aggregates alone (Figure 18). The agglomeration was not observed when **A3**, a non-ionic analogue of **B3**, was used, indicating electrostatic attraction (zeta potential of MS2 = -55.4 mV [43] and **B3** = +27.4 mV[63]) as a major driving force. The gradual decrease in inactivation kinetics in Figure 21 (e.g., 10 nM **B3** under UVA irradiation) might have resulted due to an accumulation of MS2 on the **B3** particles, preventing further MS2-**B3** interactions.

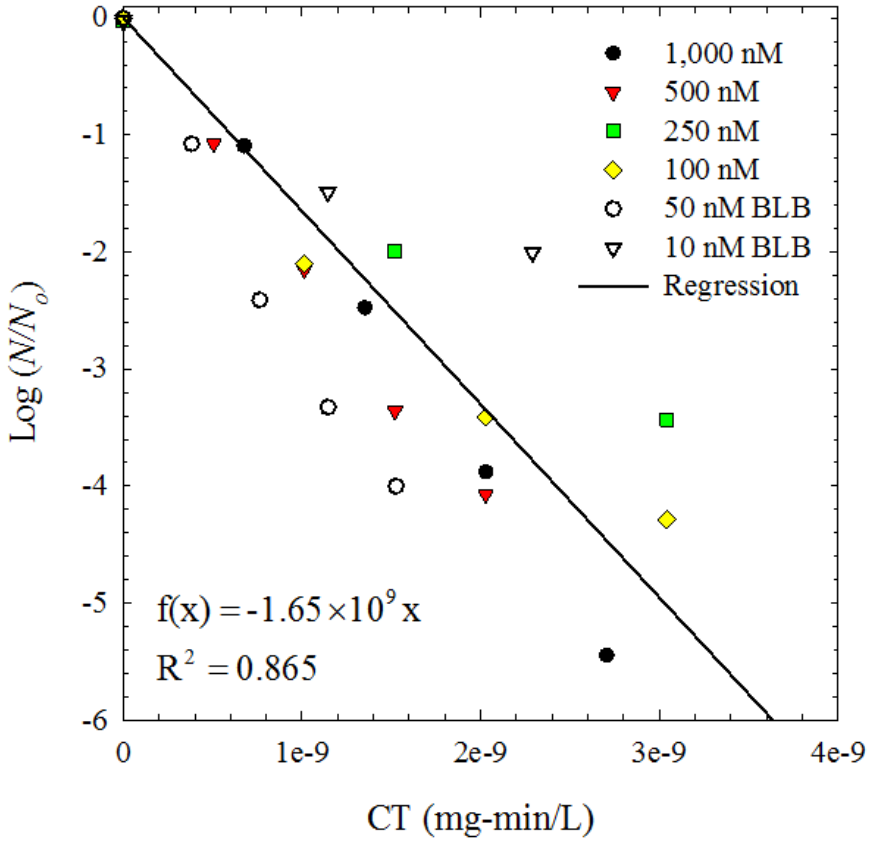

Figure 23: MS2 inactivation is plotted versus $^1O_2$-*CT* for concentration-dependence experimental data.

7. MOLECULAR INTERACTIONS

Having compiled significant characterizations on the structure to activity relationships of the functionalized fullerenes, it is obvious that cationic functionality for fullerenes with few functional groups attached are an important structural factor in determining their photoactivity and consequent biological activity. The mechanism responsible for the variable photoactivities, however, is still unresolved. This chapter provides experimental and theoretical evidence towards understanding how aggregation phenomena affect the photochemistry of fullerene aggregates, according to hypothesis five in section 1.4.

7.1. Fullerene-Fullerene Interactions

7.1.1. Examination of Nanoscale Morphology

While the size and crystallinity of the aggregates were previously measured and discussed using TEM imaging, the resolution was lacking to examine the fine features of the aggregates, including their surface roughness and crystal lattice lines. Of the derivatives studied, **A**, and **B** are compared here to examine the effects of cationic functionalization on aggregate structure, given the difference in photoactivity between the two. High resolution TEM images of the fullerenes can be found in the following figures: nC_{60} in Figure 24, **A1** in Figure 25, **A2** in Figure 26, **A3** in Figure 27, **B2** in Figure 28, and **B3** in Figure 29. High magnification imaging of nC_{60} and **A1** in Figure 24b and Figure 25b yielded clear images of crystal lattice lines, consistent with the

crystallinity observed with EDS as described in section 5.3.2. Counting the number of lattice lines found within the 20 nm scale bar, yielded 24 crystal lattice lines (or one line every 0.83 nm) for both nC_{60} and **A1**, consistent with previous reports of nC_{60} [78, 152]. Assuming a 0.35 nm radius of the C_{60} cage, the fullerenes are calculated to be 0.16 nm apart. Crystal lattice lines were not found in any of the remaining derivatives, despite the fact that EDS showed crystallinity for **A2** and **A3**. The lack of observable lattice lines may be due to the presence of functional groups causing a less uniform crystal structure to form or causing a blurring of the interstitial spaces between lattice lines.

With progressively more functional groups the **A** and **B** aggregates both appear to have less discrete particle morphology. **A3** retains distinct particle boundaries, however, while **B2** and **B3** have progressively more ambiguous particle edges. These observations can be seen in the images provided but were also consistent with other particles during analysis (images not captured). Interestingly, a large particle of what appeared to be a solid block (non-aggregated) of **B2** was found, as seen in Figure 28b and c; images of this chunk were captured to compare it to aggregated clusters and to search for crystal lattice lines, which were not found. The lack of clearly defined particles in the **B3** images; even at lower magnifications particles were difficult to image in a way that appeared fully in focus. This observation suggests that the **B3** particles are more amorphous than others. Prior work on analyzing the dependence of fullerene aggregate photoactivity on particle morphology has suggested that higher fractal dimensions (*i.e*. higher particle surface area within a given area) have greater ROS production efficiencies [75, 153]. While the fractal dimension analysis is not performed here, it is noteworthy that the observations based on the images presented seem to be in agreement, with the possible exception of **A3**. Based

on the lack of photoactivity observed for **A3** and its more irregular particles as compared to the **A1** and **A2** particles, the degree to which the particles are formed as discrete units may be more important than the fractal dimensions alone.

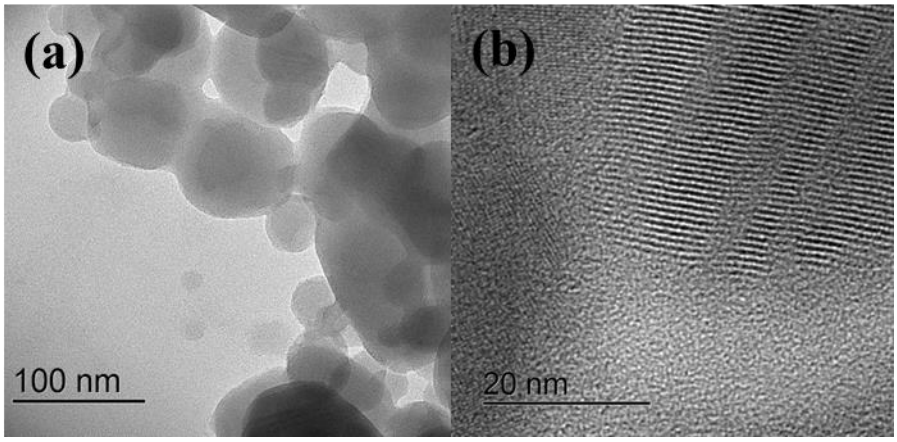

Figure 24: TEM images of nC_{60} under (a) 60k × and (b) 400k × magnification.

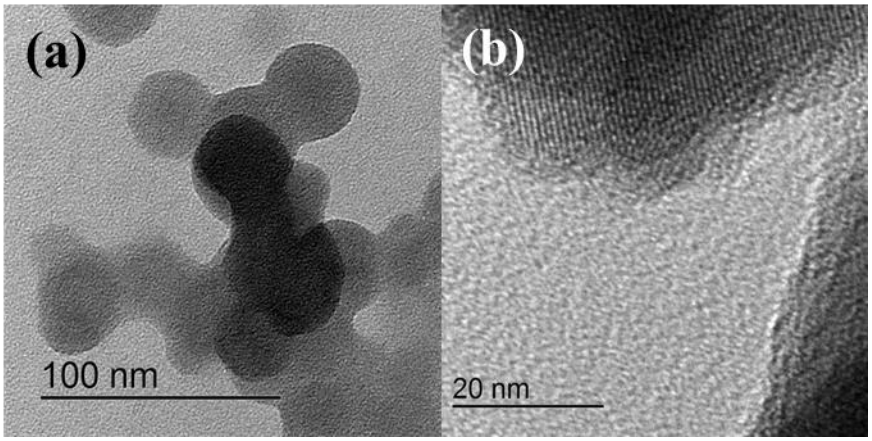

Figure 25: TEM images of **A1** under (a) 100k × and (b) 400k × magnification.

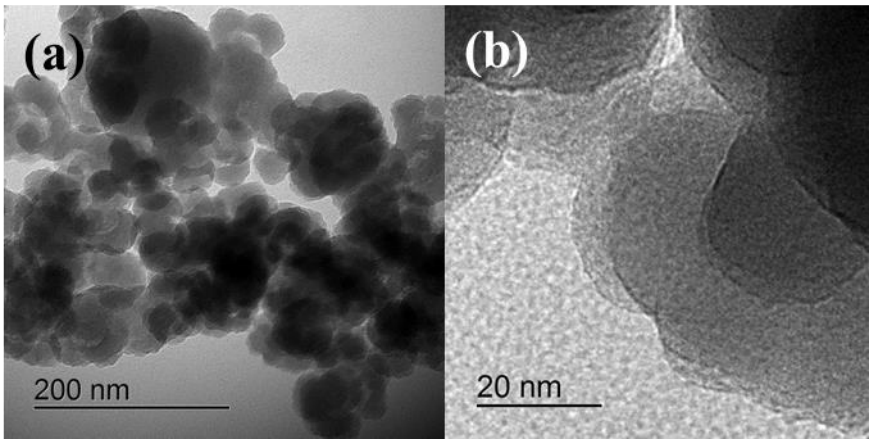

Figure 26: TEM images of **A2** under (a) 50k × and (b) 300k × magnification.

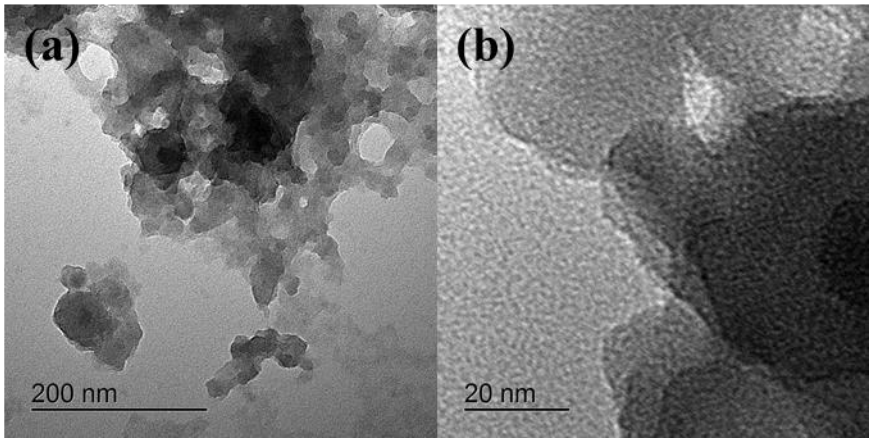

Figure 27: TEM images of **A3** under (a) 50k × and (b) 300k × magnification.

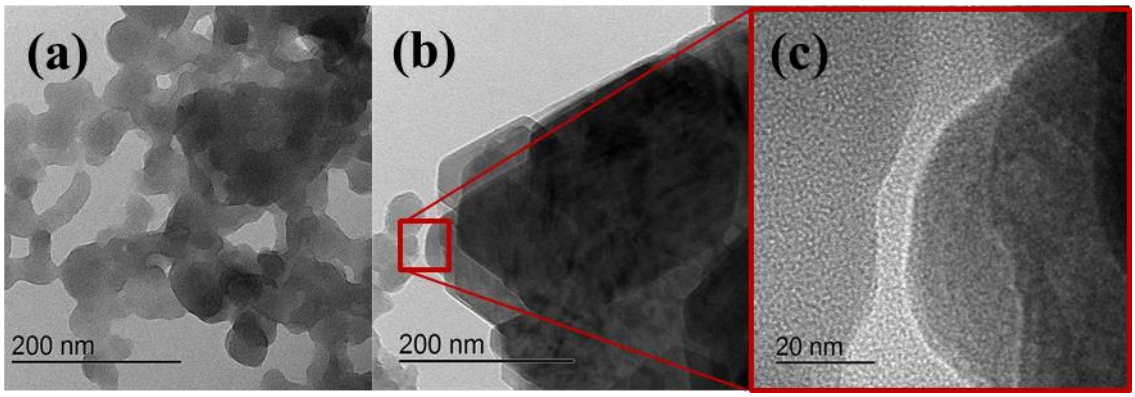

Figure 28: TEM images of **B2**, with (a) and (b) at 50k × and (c) at 300k × magnification.

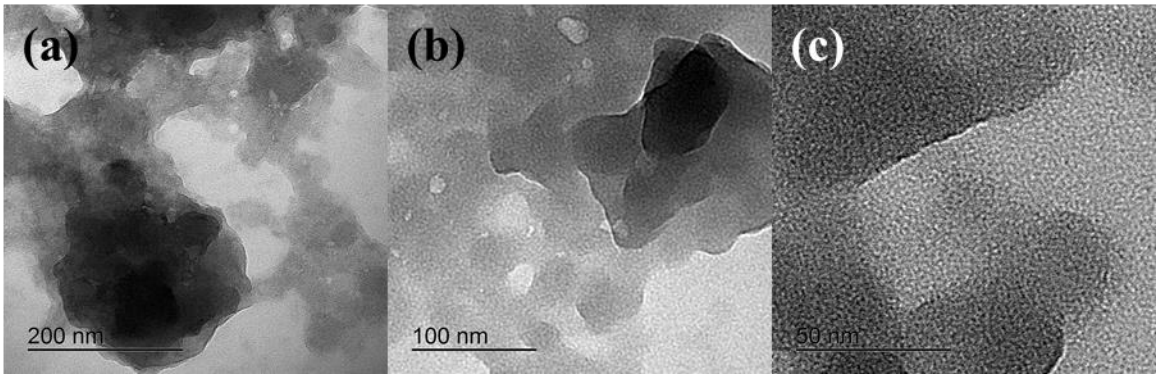

Figure 29: TEM images of B3 under (a) 50k ×, (b) 80k, and (c) 200k × magnification.

7.1.2. Simulated Interactions

As described in the section 4.5, the MD simulations in the successive NVT (298 K) – NPT (298 K and 1 atm) ensembles were performed for two nanoseconds to equilibrate the systems of 1,000 water molecules and two fullerenes of the same functionality. Subsequently, the additional MD simulations in the NPT (298 K and 1 atm) ensembles were performed for one nanosecond to characterize the time-evolved trajectories and interactions of fullerenes/fullerene derivatives. Interaction distances of the two fullerenes, measured as distances between their respective centers of mass, were computed as a function of time for one nanosecond with initial positions at 1.3 nm apart. Plots of the fullerene-fullerene distances are shown in Figure 30. The C_{60}, **A1**, and **A2** cases show clear attraction, sticking at a distance of 1 nm, or 0.3 nm from edge to edge of the fullerene cages for the C_{60} case. This result is in good agreement with the observed lattice lines in the TEM imaging in the previous section, where fullerenes were observed to arrange in a lattice with 0.16 nm spacing, between lattice lines. Of course, a crystal structure is a more complicated environment, with more external forces affecting the

spacing. Still, the values of 0.3 nm spacing predicted for solvated fullerenes and 0.16 observed in a lattice structure are not unreasonably different. The appearance of lattice lines in the **A1** and nC_{60} TEM images also correlate well with the modeling results in that C_{60} and **A1** both exhibit rapid attraction with no subsequent movement away from each other. The simulated interaction of **A2** fullerenes also predicts close attraction, even though crystal lines were not found during TEM observation. The **A2** particles were observed, however, to have very clearly defined particle boundaries with similar surface morphology as nC_{60} or **A1** aggregates. **A3**, however, exhibited a significantly more fractured or jagged morphology for particles, suggesting less regular **A3**-**A3** interactions. The simulated interactions show that **A3** fullerenes do not immediately attract and stick together, but did so after 0.7 ns of the simulation. The **A3** interaction appears to be less probable, perhaps dependent on the physical alignment of functional groups, but strong enough to stick together once the fullerenes get near each other. These observed interaction dynamics may be responsible for the aggregate surface morphology discussed previously. Finally, the **B** series exhibits significantly different and weaker interactions than C_{60} or the **A** series. For each **B** derivative, the distances never became closer than *ca*. 1.3 nm and generally varied between 1.3 and 2 nm apart, indicating weaker—and potentially nonexistent—interactions and electrostatic repulsion. The **B2** case exhibits a portion from 0.3 ns on where the **B2** fullerenes appear to have drifted apart resulting in no interaction. This distance between **B** fullerenes may be important in preventing the TTA self-quenching pathway that drastically reduces fullerene aggregates ability to photosensitize $^1O_2$ in aqueous media. The weaker interactions are also in good agreement with the observed photochemistry and particle morphology; **B** aggregates (excluding **B1**

which did not form stable aggregates) were found to be significantly photoactive with less dense and less defined particles.

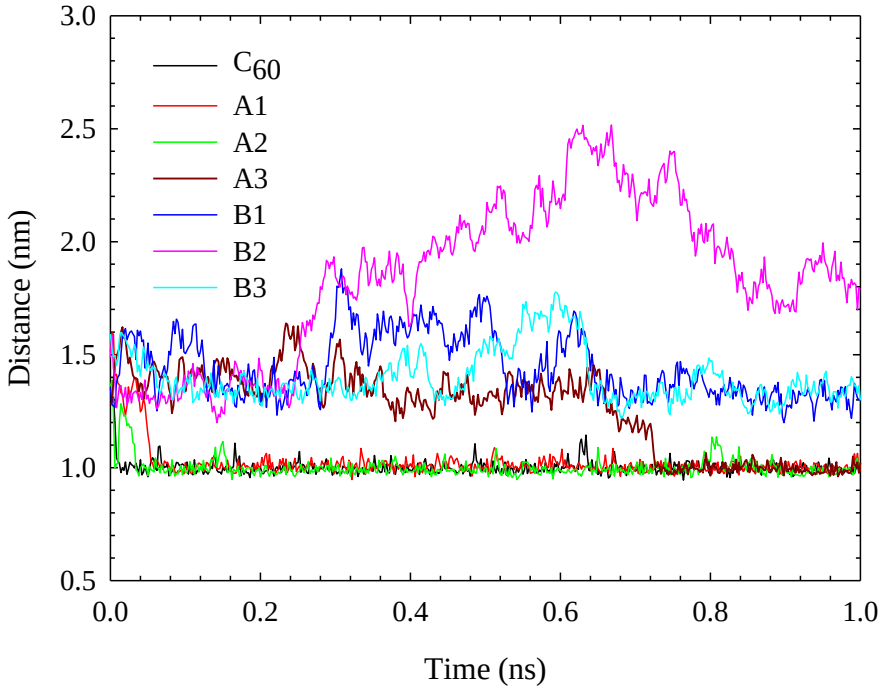

Figure 30: Fullerene-fullerene interactions in a system of 1,000 water molecules for C_{60}, **A**, and **B**.

7.2. Fullerene-Water Interactions

7.2.1. Raman Spectroscopy of Aggregate Solutions

Raman spectroscopy was employed to probe the effects of fullerene aggregates on their surrounding water solvation structures. The characteristic Raman signal from liquid water is known to shift upon changing temperature or addition of solutes and has been used to measure the impacts of such changes by various experimental conditions [154, 155]. Raman spectroscopy has recently been employed to assess the impacts of C_{60}

aggregates on the localized water structure, reporting more structured hydration environments with increasing nC_{60} concentrations [89]. The characteristic water signal was collected and is shown in Figure 31. Raman spectra of nC_{60}, **A,** and **B** aggregates were collected at varying concentrations and subsequently fitted with Gaussian-Lorentzian peaks. The peak fitting calculations provided variable results, depending on initial peak location guesses. 10 fitting attempts were therefore performed and averaged for each of the three characteristic peaks at each concentration and sample tested. Results from this Raman analysis are shown in Figure 32 for the O-H symmetric bending mode and in Figure 52 and Figure 53 in the Appendix for the first order stretching modes. The stretching modes did not appear to exhibit any clear trend, given the error bars, which represent the standard deviation of the 10 fitting attempts. The symmetric bending, however, appears to experience a slight blue shift with increasing aggregate concentrations, consistent with the previous report on nC_{60} [89]. This blue shift in the symmetric bending is likely due to an increase in the order of the water molecules solvated the fullerenes. Of the aggregates, **B3** caused the greatest blue shift in the symmetric bending mode, likely due to a greater surface area of the aggregates, as observed in the TEM imaging. It is noteworthy that all fullerenes appear to shift the bending mode to a higher energy, indicating that they are all affecting the localized water structures.

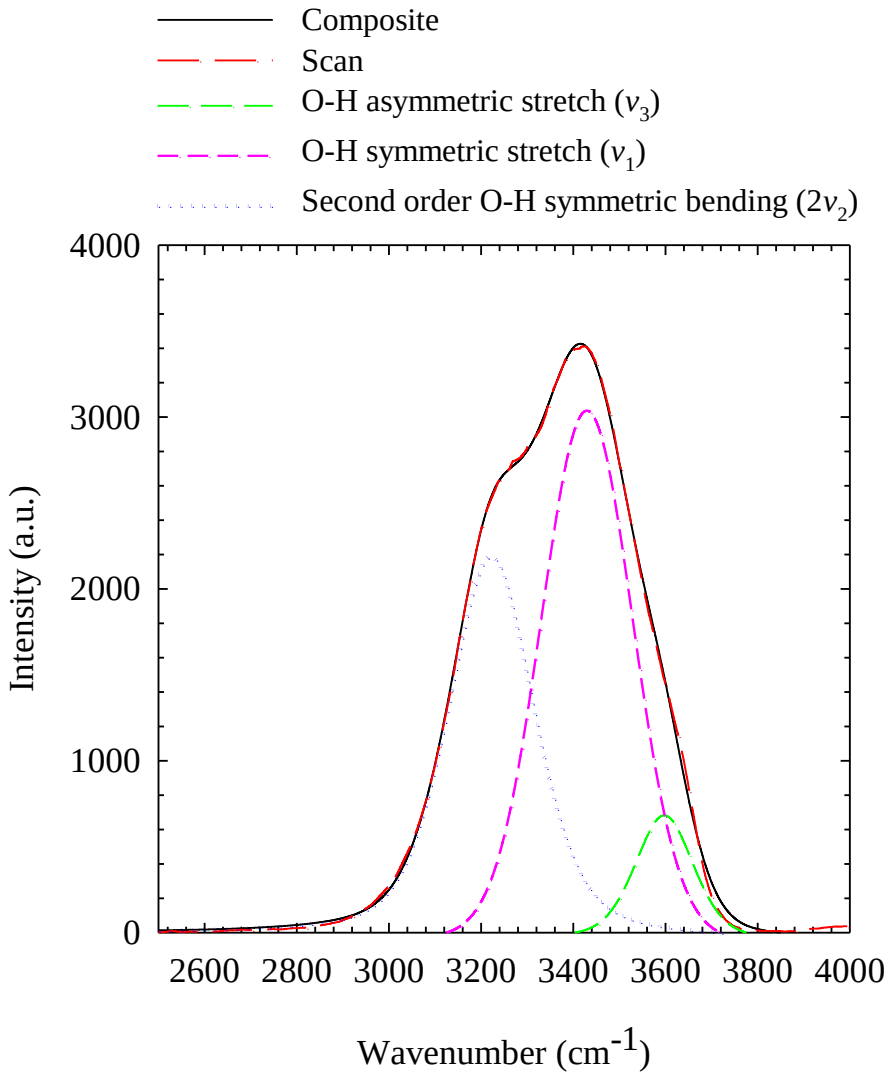

Figure 31: Raman spectra and fitted Gaussian-Lorentzian peaks for DI water.

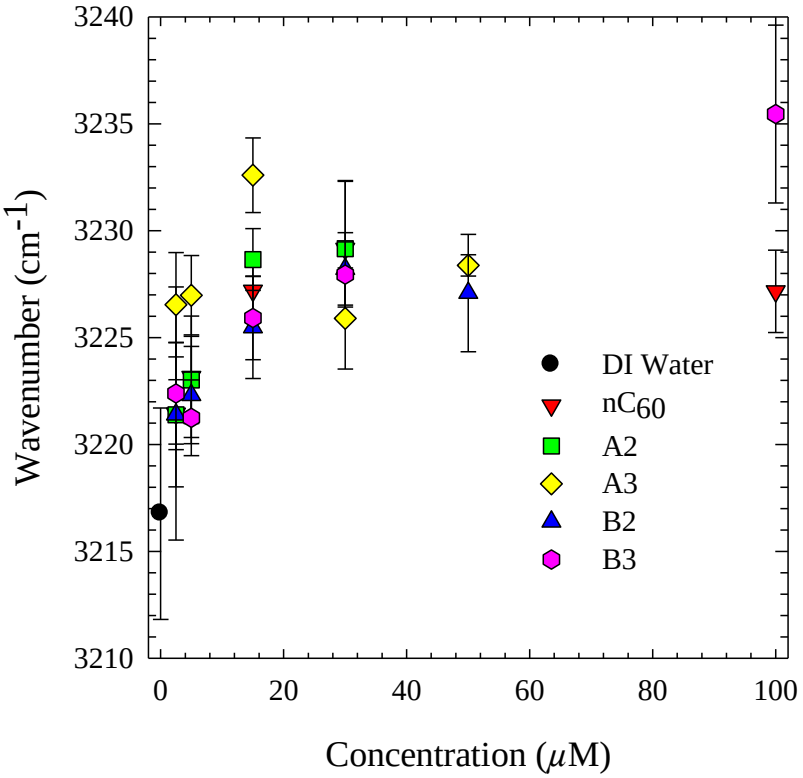

Figure 32: Raman peak locations of the second order O-H symmetric bending ($2\nu_2$) for varying concentrations of fullerene aggregates.

7.2.2. Radial Distribution Functions

RDF predicted from the MD simulations in the NPT (298 K and 1 atm) ensemble were analyzed calculations were computed for C_{60}, and the **A** and **B** derivatives. Results for C_{60} appear to match well with what has been reported previously in literature. In Figure 33 the calculations shown predict a first hydration shell at approximately 6.5 Å and a second at around 9.5 Å from the center of mass for the fullerenes. These values match the reported radii for hydration shells very well [84-86, 88]. A slight reduction in the density of water molecules at the first hydration shell is noted in the derivatives as

compared with C_{60}, likely due to the presence of the functional groups occupying space that would otherwise have water molecules. This observation is consistent within each series of derivative: with each functional group added there is a lower density of water molecules in the first water layer. A corresponding increase in density in the region just beyond the first hydration shell with increasing functionalization provides further evidence. Generally, the fullerenes do not appear to be significantly different in the way they affect the hydration layer immediately surrounding fullerenes, consistent with observations from Raman spectroscopy. One scarcely noticeable difference between the **A** and **B** series is a slight shift in distance for **B3** compared to **A3**, as seen in Figure 33b, which could indicate slightly weaker **B3**-H_2O interactions.

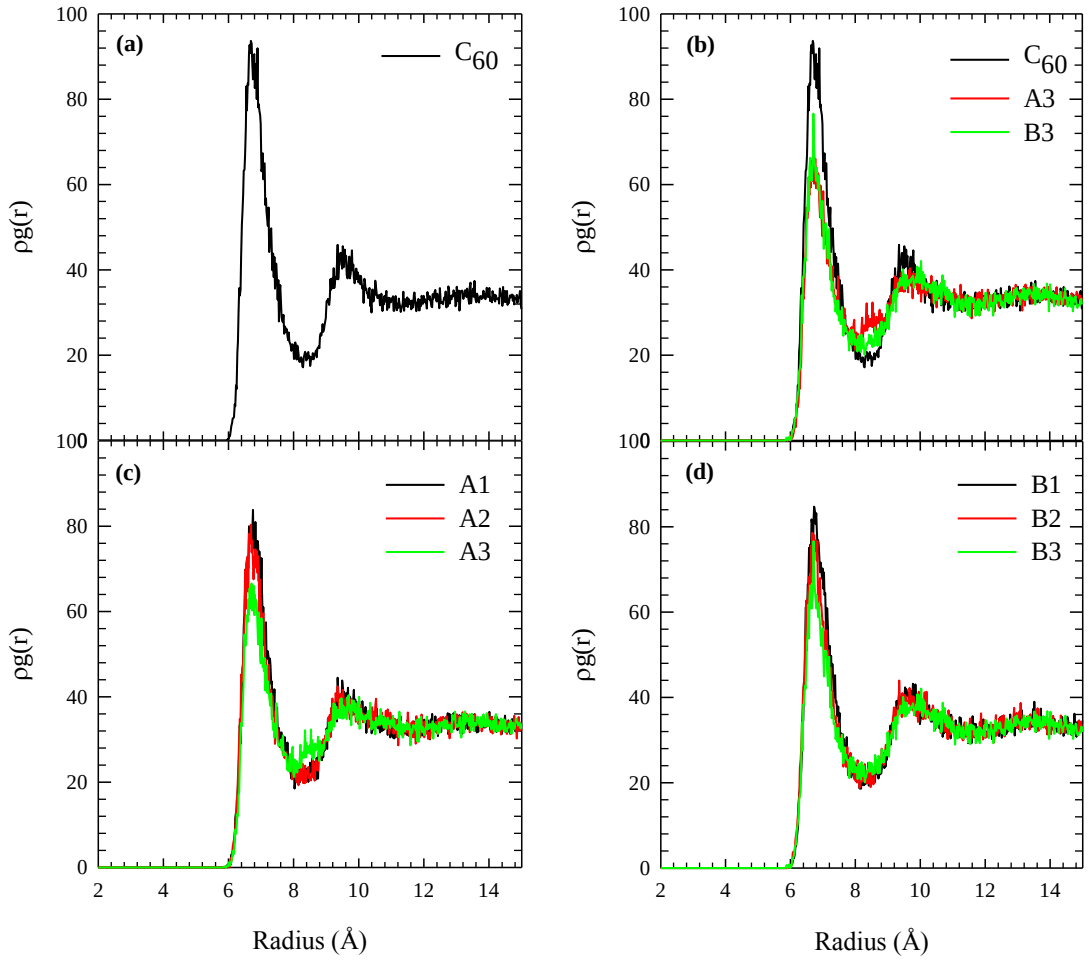

Figure 33: RDF of water molecules from the center of mass of (a) C_{60}, (b) C_{60} compared with **A3** and **B3**, (c) the **A** series, and (d) the **B** series. ρg(r) indicates the density of water molecules at a given radius r.

7.2.3. Mean Squared Displacement Computations

Similar to the RDF case, the MSDs matched well with previous reports of the MSDs of water molecules around C_{60} [85]. Figure 34 plots the MSD of all water molecules in the C_{60}, **A2**, and **B2** systems along with the MSD for each water layer around C_{60}. The MSD of the first and second hydration layers of C_{60} are also in well accordance with reported literature values [85]. Analysis of these three fullerenes shows that hydrophilic functionality causes a decrease in water mobility around the fullerenes. This decreased mobility likely indicates a shift in the nature of the hydration of water around the fullerene cage; water molecules would be more stable next to hydrophilic functional groups compared with the hydrophobic cage of C_{60}, resulting in reduced movement. Another observation from the hydration layers for each of the **A** and **B** fullerenes in Figure 35 is that the mobilities for each fullerene vary by hydration layer (*ie*., 1^{st}, 2^{nd}, or bulk water molecules), but there appears to be no consistent trend for the variable order of the layers' MSD values. These results are in good agreement with the RDF results, suggesting that there are distinct hydration layers that can be characterized, but the differences in hydration between different types of fullerenes are not noticeably different.

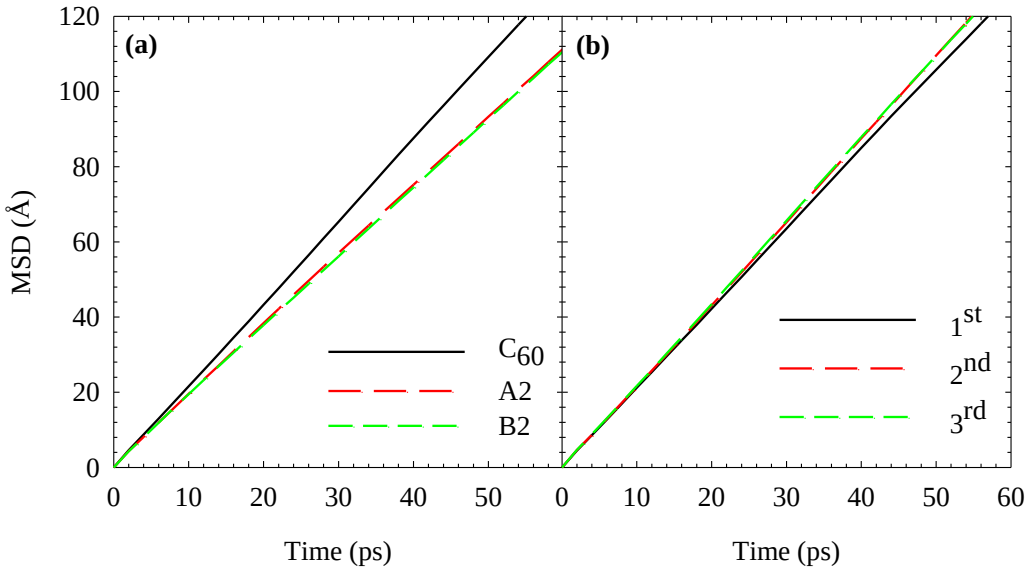

Figure 34: MSD as a function of time of (a) all water molecules in the C_{60}, **A2**, and **B2** cases and (b) the water molecules in the 1st, 2nd, and 3rd hydration layers for C_{60}.

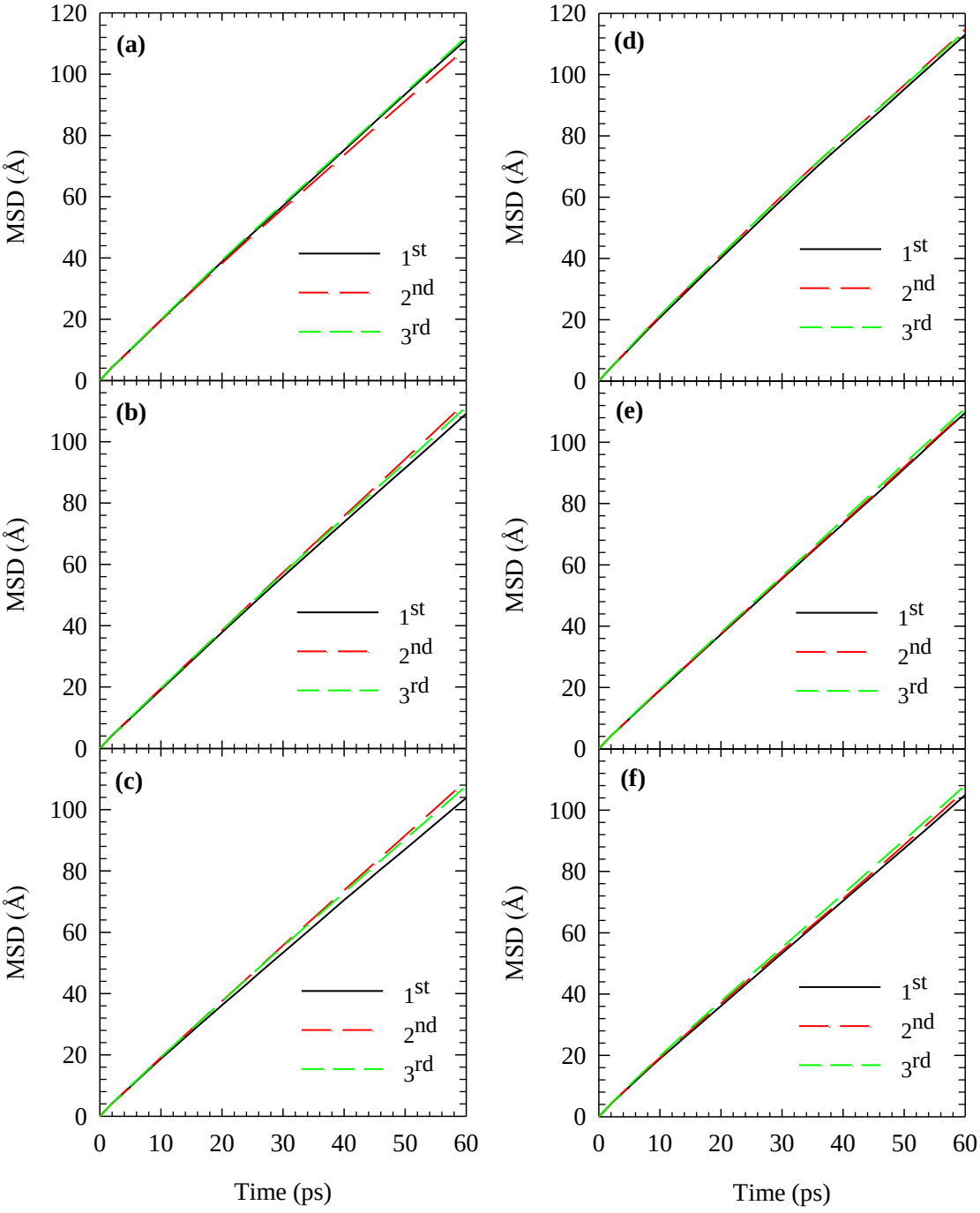

Figure 35: Water molecules in the 1st, 2nd, and 3rd hydration layers as a function of time for (a) **A1**, (b) **A2**, (c) **A3**, (d) **B1**, (e) **B2**, and (f) **B3**.

7.3. Fullerene-Oxygen Interactions

The interactions between an O_2 molecule and each fullerene within the system of 1,000 water molecules were analyzed from the MD simulations in the NPT (298 K and 1 atm) ensemble which were performed over a 1 ns timeframe. Fullerene-O_2 interactions may have significant implications on the ability for the sensitization process to occur. Interaction distances and energies have been recorded for C_{60} and each of the **A** and **B** fullerenes. Figure 36 shows the interactions of O_2 with C_{60}. Clear and strong interactions are present between 0.2 and 0.4 ns, for a total of 201 ps of interaction time, with interaction energies ranging between -0.5 and -1.4 kcal/mol. These strong interactions may cause adsorption (or exciplex formation) of O_2 onto the C_{60} such that it does not subsequently escape into the bulk phase after receiving an excitation. Indeed, a study of sensitizing $^1O_2$ in the gas phase using fullerene coated surfaces showed that $^1O_2$ adsorbed onto the fullerene surfaces rapidly without significantly escaping into the gas phase [156]. It has also been shown that O_2 can act as a catalyst for back electron transfer (BET) reactions in a zinc porphyrin-fullerene system [157], which may be a relevant process by which a ground state fullerene quench $^1O_2$ [9]. Alternatively, if an O_2 molecule remains at the surface of a fullerene too long, the BET process may proceed and quench the excitation before the C_{60}-O_2 exciplex dissociates. Lifetimes of charge transfer exciplexes for 9-cyanophenanthrene and electron donors were reported in the nanosecond time frame [158]. Finally, the ability for the O_2 molecule to rotate within the solvent cage is an important factor limiting the internal conversion rate step of the $^1O_2$ sensitization [159]. Researchers have shown that sensitizers with strong sensitizer-O_2 interactions experience

decreasing $^1O_2$ production efficiency with increasing solvent polarity [160-164]. Overall $^1O_2$ production efficiencies were also shown to decrease with decreasing sensitizer oxidation potentials [160-165]. The dependence of $^1O_2$ sensitization efficiency on solvent polarity and sensitizer oxidation potentials stems from the nature of the charge-transfer exciplex that is responsible for the majority of $^1O_2$ sensitization, including by fullerenes [164].

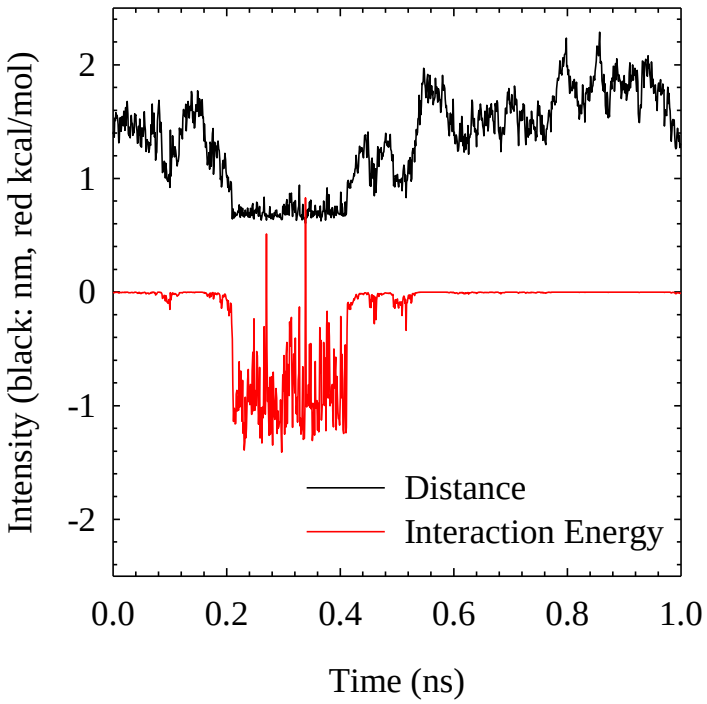

Figure 36: Interactions between C_{60} and O_2 over 1 ns; the black line represents distance and the red represents interaction energy between C_{60} and the O_2 molecule.

The interaction dynamics of O_2 with the **A** and **B** fullerenes are presented in Figure 37. A clear distinction between the **A** and **B** series is immediately visible, with less O_2-fullerene interactions for the **A** series than for **B**. On average the **A** derivatives

had interaction times of 103 ps during the 1 ns simulation, while the **B** derivatives had an average of 30 ps of interaction time. The interaction energies were generally in the range of -0.5 to -1.8 kcal/mol, with the notable exception of **B2** which only reached an interaction energy of -0.18 kcal/mol. The significant difference in the O_2 interactions between the **A** and **B** fullerenes correlates well with the photoactivities of **A** and **B** as aggregates reported here and implicates the importance of the sensitizer oxidation potentials, as discussed above. The **B** series has innately higher oxidation potential, given the cationic charge(s), than the **A** series, which was also observed during the measurement of their surface charges. These theories provide a new framework for understanding the photoactivity of fullerene aggregates. Given the highly polar nature of water and the strong interactions between most fullerenes and O_2, the rotational mobility of O_2 during exciplex formation and electron and energy transfer processes, the oxidation potential of the fullerene may be an important driver of its photoactivity, with higher potentials allowing for more mobile O_2 molecules and higher sensitization efficiencies.

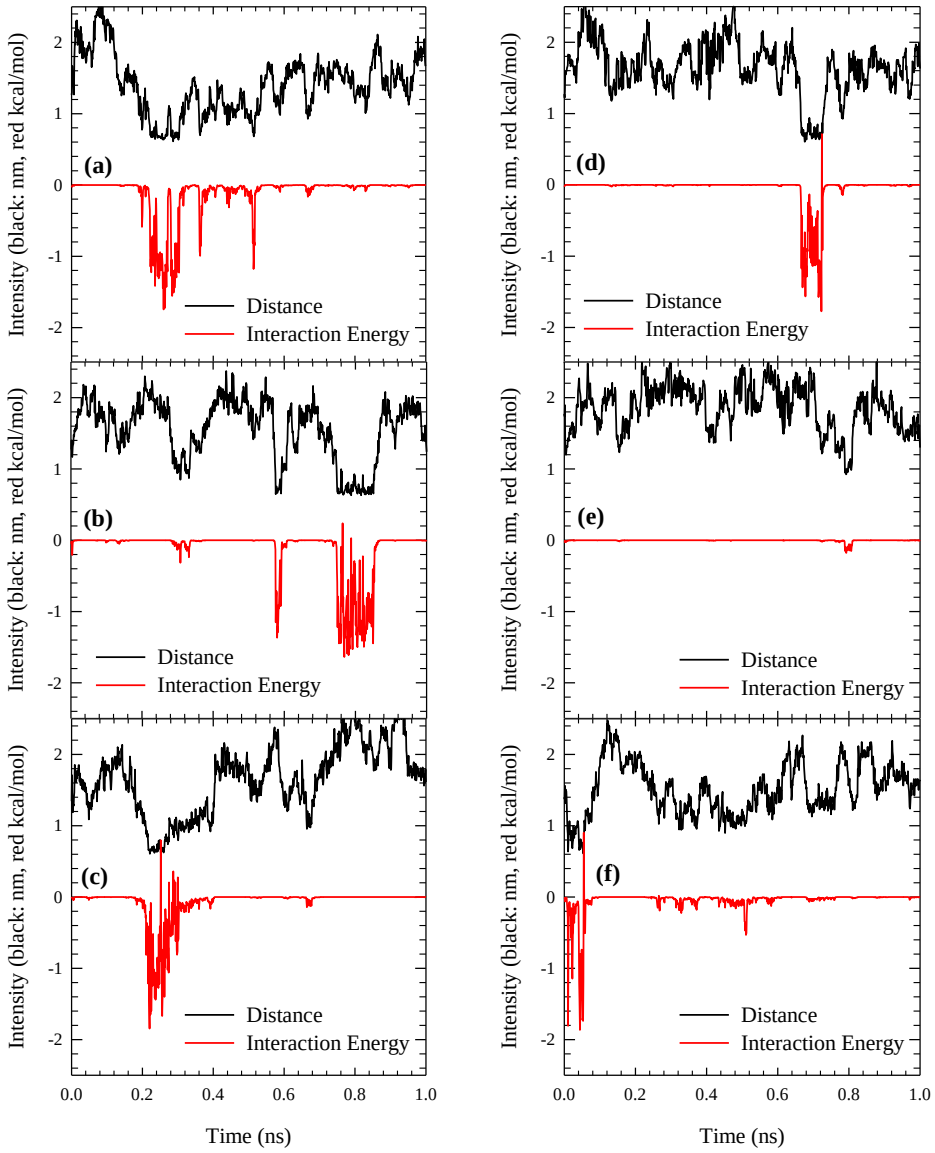

Figure 37: Interactions between (a) **A1**, (b) **A2**, (c) **A3**, (d) **B1**, (e) **B2**, and (f) **B3** and O_2 over 1 ns; the black line represents distance and the red represents interaction energy between each fullerene and the O_2 molecule.

8. ENVIRONMENTAL IMPLICATIONS

8.1. Importance of Physical, Chemical, and Photochemical Characterizations

The results of thorough characterizations of carefully chosen fullerene derivatives herein highlight and addressed several key gaps in the understanding of how aggregation affects fullerene photochemistry, particularly for functionalized fullerenes. There have been two common explanations for the lack of photoactivity of fullerene aggregates: reduced surface area [53] of the particles and their crystalline nature promoting triplet-triplet annihilation [10, 54, 65] effectively reducing their photoactivity. In this study, however, neither theory has fully explained the observations made for the derivatives studied: large aggregates effectively produced $^1O_2$, while smaller particles that were not crystalline produced no observable $^1O_2$. The only observable difference between the photoactive and non-photoactive derivatives was that **B2** and **B3**, which both produced $^1O_2$, had positively charged surfaces, unlike all other derivatives with negative zeta potentials. Although molecule-molecule interactions are still likely to be important, surface phenomena may also be critical to the photochemistry of aggregates. In particular, surface oxidation potential and consequent hydration structures may interfere with the sensitization process of negatively charged fullerene aggregates that may otherwise be effective sensitizers (*e.g.*, the **C** series which were not crystalline) [78, 135-137]. It is known that redox characteristics affect $^1O_2$ production efficiency for sensitizers [159] and that significant solvent-complex reorganization must be allowed for an important route of $^1O_2$ sensitization [166]. These characteristics have perhaps been overlooked by

researchers wishing to establish a mechanistic understanding of fullerene aggregate photochemistry. For the cases of slightly functionalized fullerenes, environmental concerns based on the photosensitization capacity of fullerene aggregates appear to be dependent on the properties of the type of functional group attached, more than the number of addends.

Close examination of the chemical changes in the fullerene derivatives upon aggregation in water were made to discern the effects of aggregation-induced functionalization (with O groups) on aggregate photochemistry. While several research groups have examined this type of functionalization (and intentionally induced further surface oxidation in some cases) of nC_{60} and have attributed these effects to increased photoactivity [75, 78, 79, 90, 139, 153], few studies have conducted these types of studies on functionalized fullerenes. Based on the FTIR and XPS analysis reported here, it is clear that surface oxidation of the functionalized fullerenes occurs consistently across various types of fullerenes and does not drive the stark difference in photochemistry observed between the **A** and **B** series. It is important to realize that this surface oxidation mechanism responsible for the stabilization of nC_{60} aggregates in water with a negative charge is at play for both **A** and **B** derivatives, noted by the negative surface potential of **B1** aggregates and increasingly positive potentials for **B2** and **B3** [63]. This finding suggests that the aggregation process and technique employed may not be as important in determining the photosensitization capacity of fullerenes as their final surface character and potentials.

8.2. Remarks on Photoinactivation and Toxicity

The potential biological effects of the fullerenes were tested to examine the relationships between photoactivity, functionalization, and toxicological effects. The work presented herein found that of nC_{60} and each series of derivatives studied, only the **B** series was found to exert significant toxicity on *E. coli*. Further, only **B2** and **B3** showed any appreciable photo-induced inactivation of MS2 bacteriophage or *E. coli*, in excellent agreement with the observed $^1O_2$ production. Although **B2** and **B3** exhibited highly similar inactivation rates, **B3** was examined thoroughly in order to make comparisons with previously reported inactivation kinetics. It is difficult to directly compare the kinetics of **B3** with other fullerenes in literature, given the variable concentrations and light sources used. Close examination of published data on fullerenes as photoinactivation agents, summarized in Table 5 in the Appendix, points to the remarkable photoinactivation efficiency of the methyl pyrrolidinium substituted fullerene. Badireddy *et al*. conducted experiments with twice the UVA intensity (2.3 mW/cm^2) and *ca*. 1000 times higher concentration and reported inactivation rates that were an order of magnitude slower for several fullerenes as compared with **B3** [64]. The aminofullerene [43] was also tested under stronger light intensity and concentrations that were 5 to 20 times higher than our highest reported here and yielded inactivation rates that were two orders of magnitude slower than our values. The account of **B3** photo-induced MS2 inactivation here is particularly astonishing because vanishingly low concentrations achieved rapid MS2 inactivation under environmentally relevant light intensities. While *ca*. 1-log difference in inactivation kinetics may be attributed to difference in $^1O_2$-*CT*,

which is likely enhanced due to virus-aggregate interactions as discussed above, the remarkably rapid kinetics of **B3**-MS2 inactivation could be the result of more efficient $^1O_2$ production per irradiation intensity and sensitizer concentration. We report a $[^1O_2]_{ss}$ of 3.17×10^{-13} M produced from 5 μM **B3** (Figure 54), while we estimate the $[^1O_2]_{ss}$ from the reported *CT* and inactivation time of Badireddy *et al.*'s $C_{60}(NH_2)_6$ sample to be 7.94×10^{-14} M from 6.13 μM of fullerene under much more intense light conditions. Overall, this study calls for greater attention to the promising environmental applications and potentially significant environmental implications of this material.

8.3. A Closer Look

Conflicting theories regarding the variable photoactivities of fullerene aggregates prompted a closer examination of the molecular interactions and surface phenomena that have not previously been explored for sequentially functionalized fullerenes. A suite of molecular characterization and modeling techniques were employed to explore the dynamics of fullerene photosensitization of $^1O_2$ at the molecular scale. High resolution TEM imaging revealed important morphological differences between the non-photoactive **A** derivatives and the photoactive **B** series. TEM imaging suggests that the surface character (amorphous verses clearly bounded) of aggregates may be more important in deciding their photoactivity than their size. This structural factor will be important in predicting the photoactivity of other functionalized fullerenes. Furthermore, these physical observations align well with the modeled results of fullerene to fullerene interactions in an aqueous system, where the **B** derivatives were found to have less

interaction and no ‘adhesion’ to one another, as observed in the **A** cases. The closer clustering of fullerenes in the **A** cases likely leads to increased triplet-triplet annihilation compared with the **B** aggregates, explaining the dichotomized photoactivities. In this case, molecular modeling may be a quick and relatively cheap method of predicting the photoactivity, and therefore photo-toxicity, of novel functionalized fullerenes.

To summarize the findings of hydration dynamics around the fullerenes, it was found that, as previously reported for C_{60}, each fullerene is predicted to have two to three distinct water layers acting as solvation cages around the fullerene core. Interestingly, these water layers were not significantly different in physical ways probed with RDF and MSD simulations. Similarly, the Raman spectroscopic results suggested an increase in the structure of water around aggregates but did not find significant differentiation between types of functionalization. At first look, these results of hydration layers seem inconsequential to the examination of the photosensitization mechanism of fullerene aggregates. Combining the hydration observations with O_2-fullerene interactions modeled in an aqueous system, however, provides a deeper understanding of how the surface character of fullerene aggregates affects the interactions of O_2 with fullerenes within the solvation shells. It is known that during the photosensitization process, a sensitizer and O_2 form an exciplex where energy is transferred through partial charge transfer (zero net charge exchange) [159]. These exciplexes undergo an internal conversion that requires the O_2 molecule to be able to rotate within the solvation cage; stronger interactions between the O_2 molecule and the sensitizer can cause a decrease in sensitization efficiency due to a decreased mobility of O_2 [159, 164, 167]. A clear difference in O_2-fullerene interactions was observed for the **A** and **B** derivatives here. The **B** series, which

was found to be significantly photoactive as aggregates, had significantly weaker interactions with O_2 than C_{60} or the **A** fullerenes. The strong O_2-C_{60} interactions for non-photoactive fullerenes suggest that the sensitization route is inhibited by a decrease in O_2 mobility within the solvent cage around the exciplex unit. These observations suggest that the aggregation of the fullerenes themselves may not play such an important role in photosensitization of $^1O_2$ after all. It is possible that an individual C_{60} molecule in an aqueous solution would have inhibited $^1O_2$ production efficiency simply due to its low oxidation potential in a highly polar solvent. These analyses also provide a useful tool for predicting the photochemistry of novel fullerene derivatives, particularly if prediction can me made simply based on the oxidation-reduction potential of a given fullerene in water.

It is likely that many factors are at play in determining the photoactivity of fullerene derivatives. The thesis presented here provides significant insights on the degrees to which various mechanisms affect fullerene photochemistry in water. The results presented discount the mechanisms of aggregate size, crystallinity, surface oxidation, and alteration of the pi-conjugated C_{60} cage as major factors in predicting fullerene photoactivity in water. Rather, the fullerene-fullerene interactions and consequent surface morphology of aggregates and the oxidation potential at the surface of the fullerenes may be the two most important factors predictive of the capacity for fullerene aggregates to effectively sensitize $^1O_2$ in aqueous media.

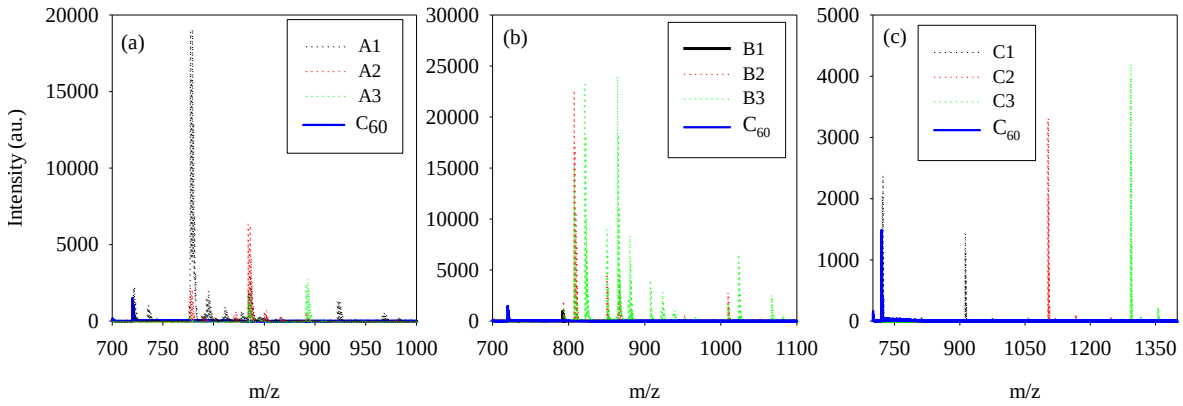

Figure 38: MALDI-Mass spectra for C_{60} with a.) **A** derivatives in toluene, b.) **B** derivatives as aqueous aggregates, and c.) **C** derivatives in toluene.

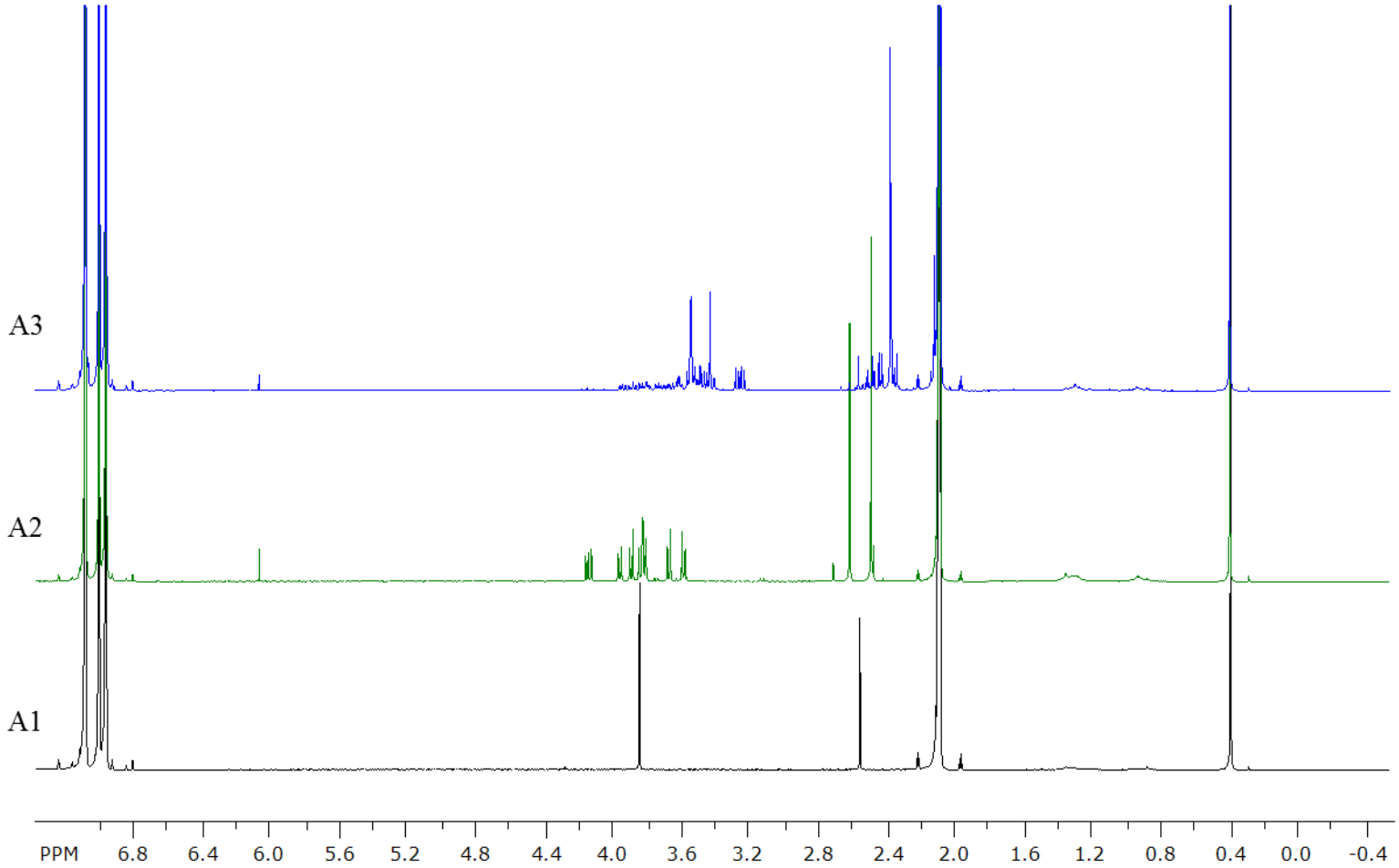

Figure 39: H-NMR Spectra for **A** derivatives in deuterated toluene, showing characteristic methyl and methylene signals from the pyrrolidine group(s) at ca. 2.5 and 3.8 ppm, respectively.

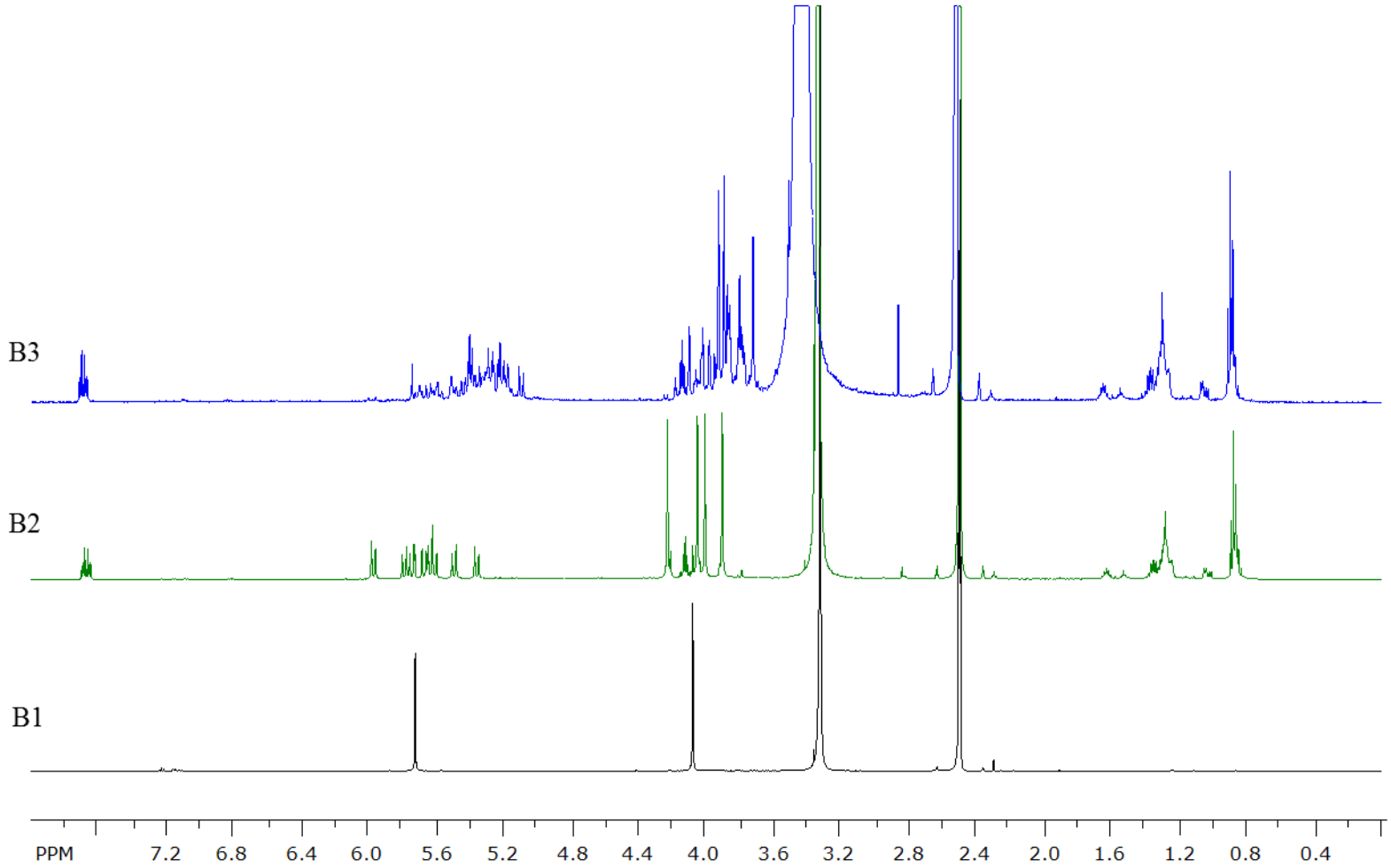

Figure 40: H-NMR Spectra for **B** derivatives in deuterated dimethyl sulfoxide, showing characteristic methyl and methylene signals from the pyrrolidine group(s) at ca. 4.0 and 5.8 ppm, respectively.

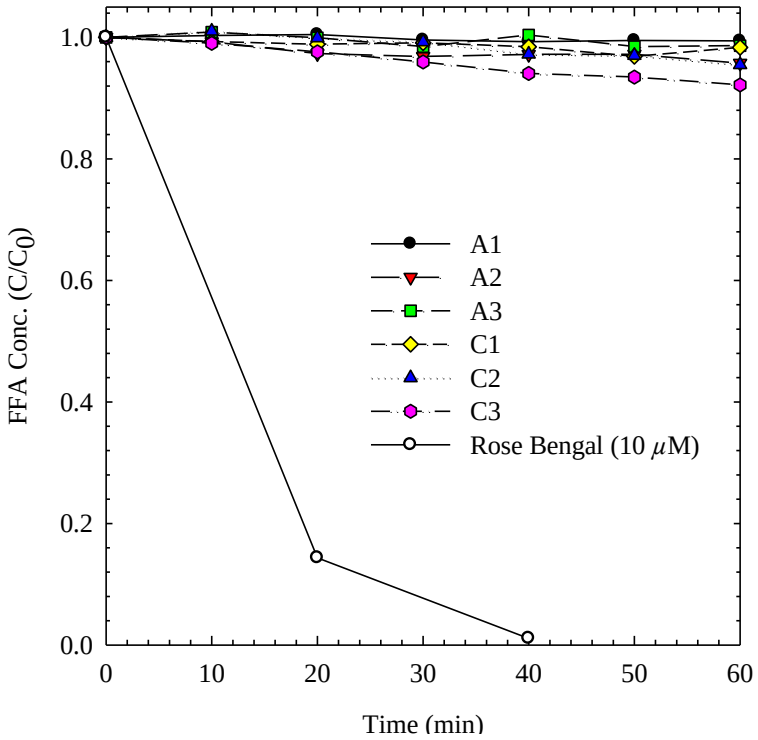

Figure 41: FFA degradation in water by 5 μM A and C derivatives under BLB with 10 µM Rose Bengal under visible light as a positive control.

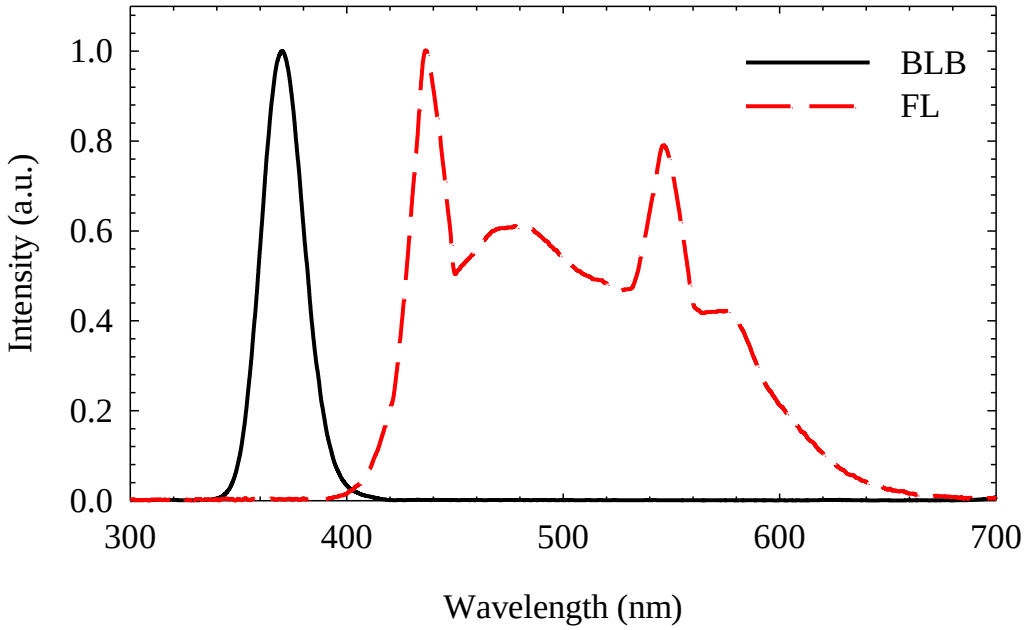

Figure 42: Normalized intensity spectra for the BLB lamps and the FLs with a UV cutoff filter.

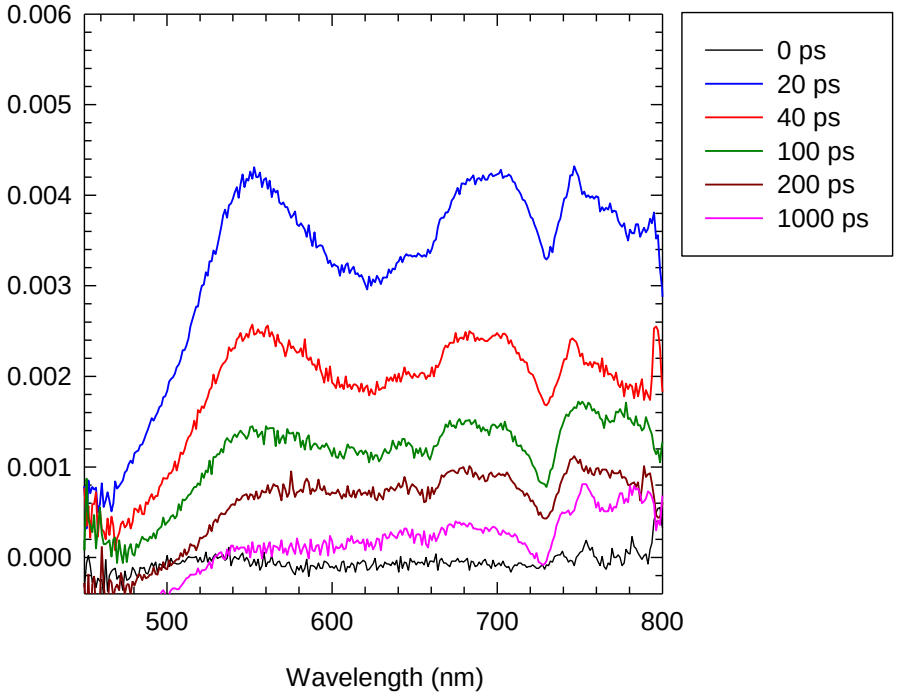

Figure 43: Transient absorption spectra for **A1** during pulse radiolysis.

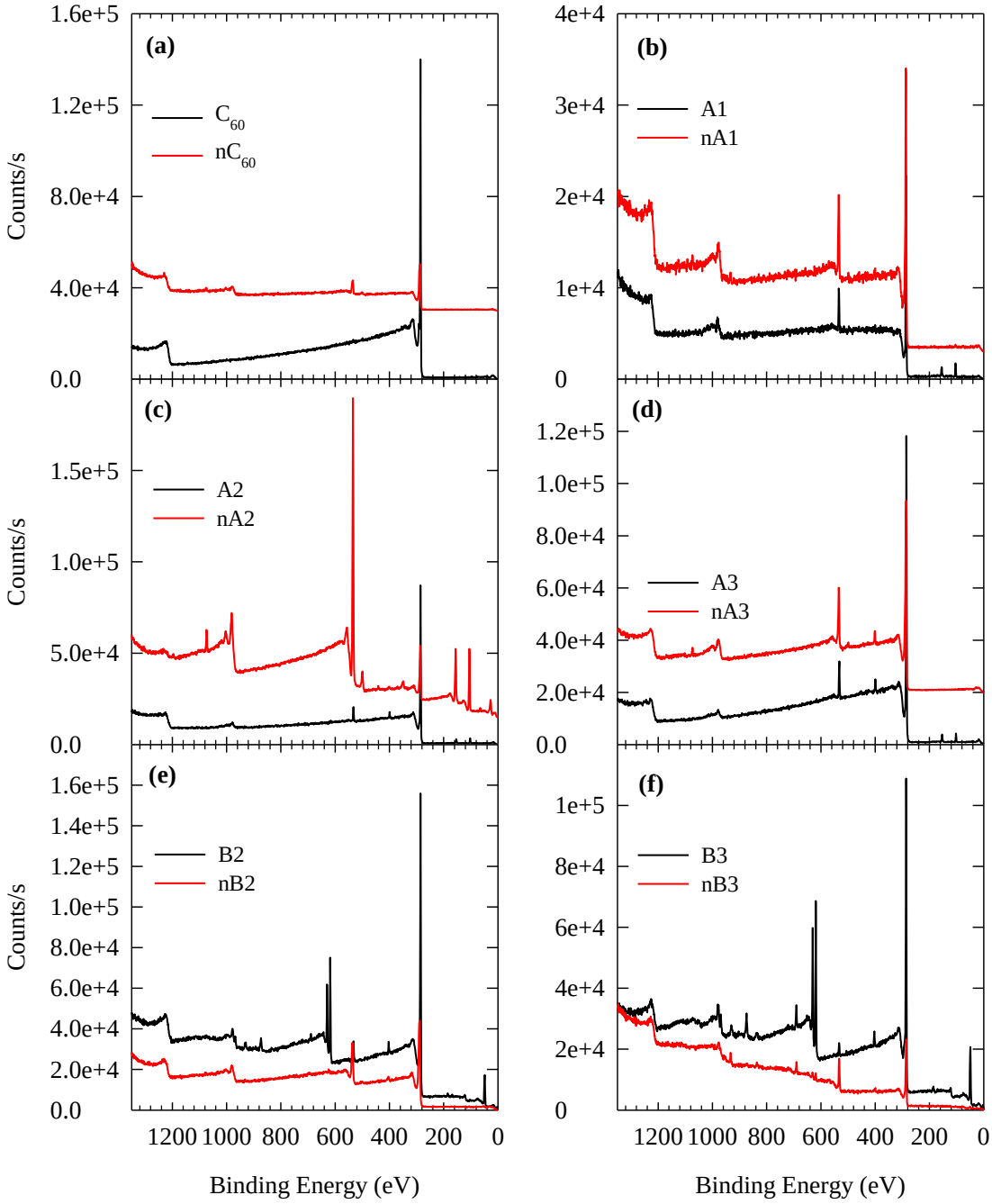

Figure 44: XPS scans of fullerenes before and after aggregation.

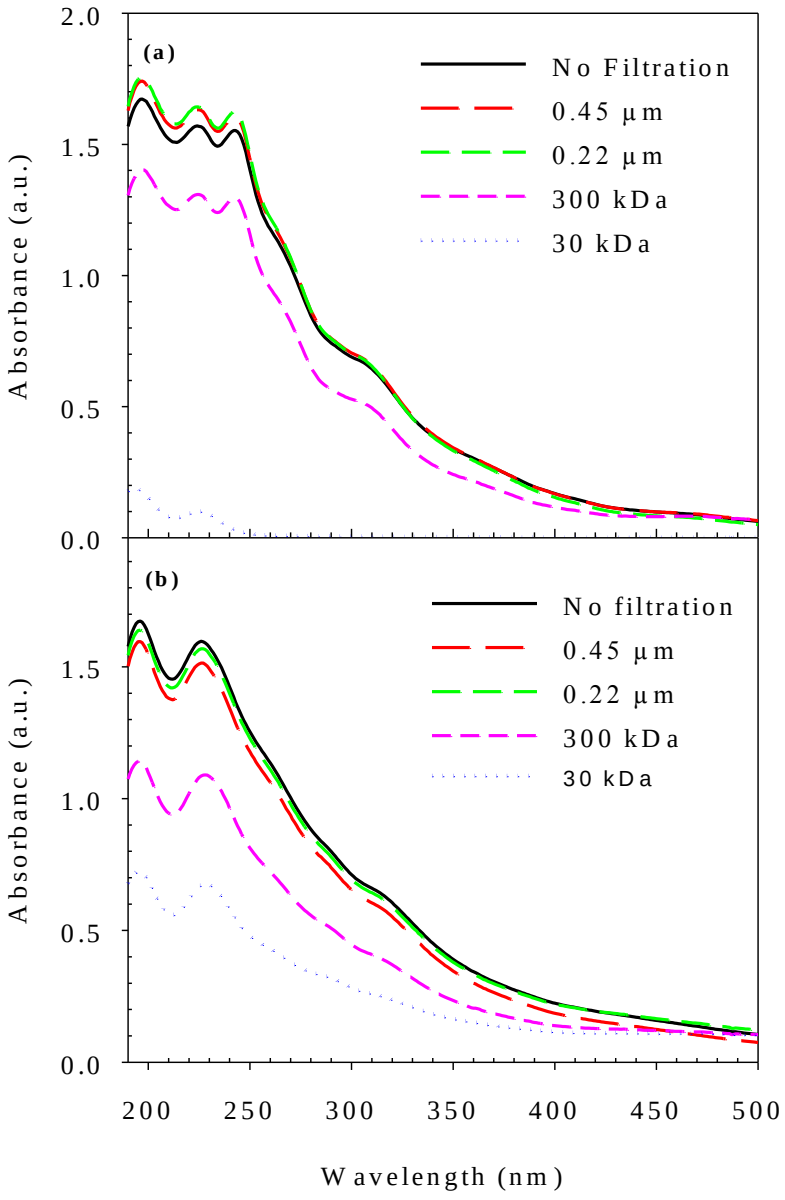

Figure 45: UV/Vis spectra characterizing the size fractionated solutions for (a) **B2** and (b) **B3**.

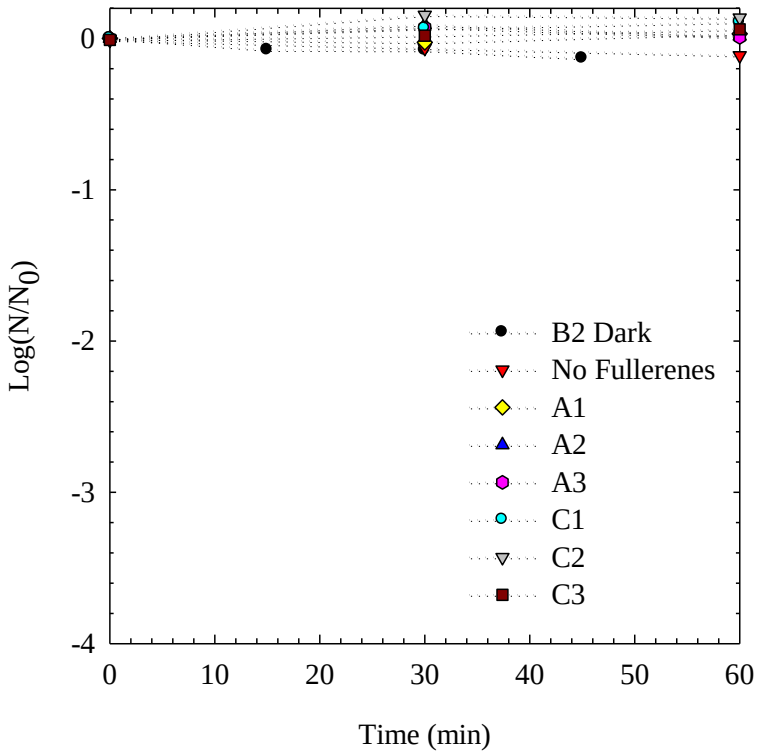

Figure 46: *E. coli* inactivation by UVA only, **A**, and **C** derivatives at 5 µM under UVA, with a dark control using **B2** at 5 µM.

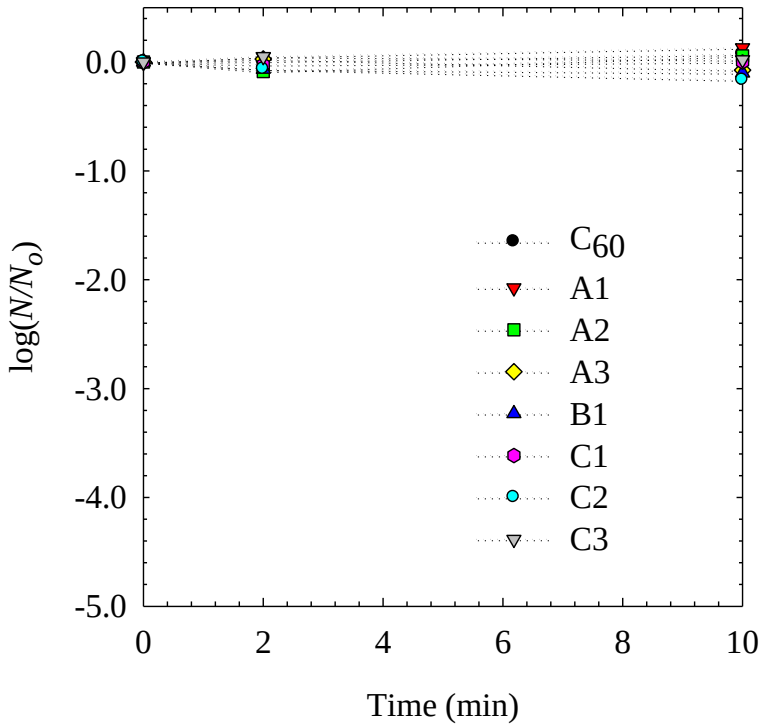

Figure 47: MS2 inactivation by nC_{60}, **A**, and **C** derivatives at 5 μM with UVA irradiation.

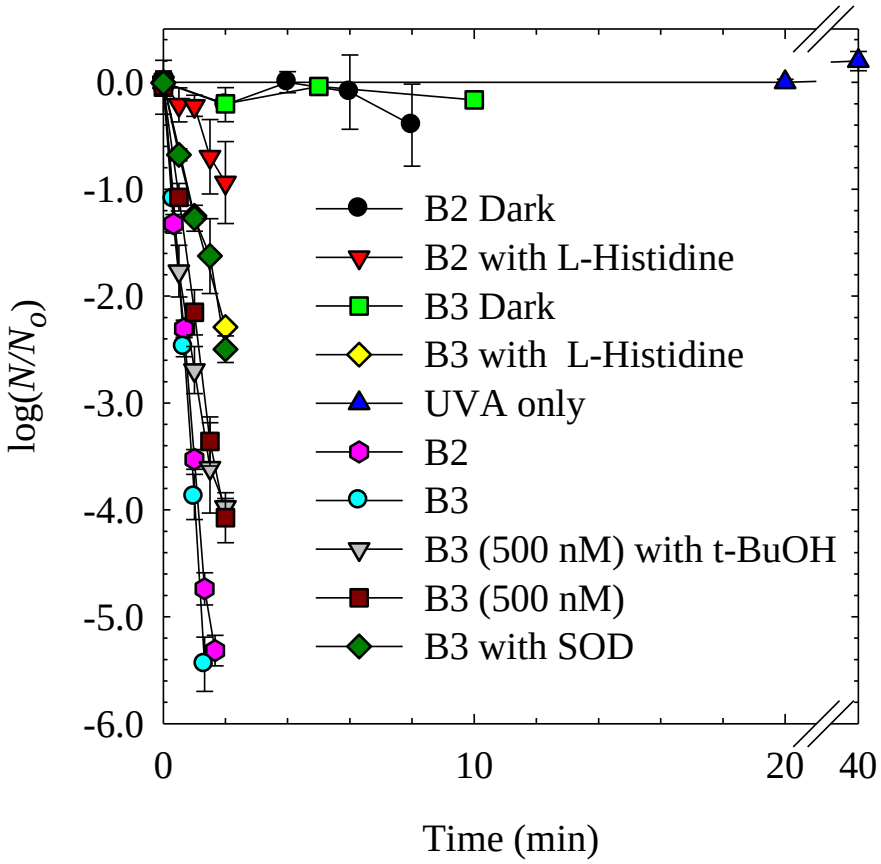

Figure 48: MS2 inactivation for **B2** and **B3** at 1 μM (unless otherwise specified) with dark, L-histidine (250 mM), t-BuOH (30 mM), and SOD (30 mM) controls using and a UVA only (no fullerene) case. Data is also shown from Figure 21 for experimental values of **B3** at 500 and 1,000 nM.

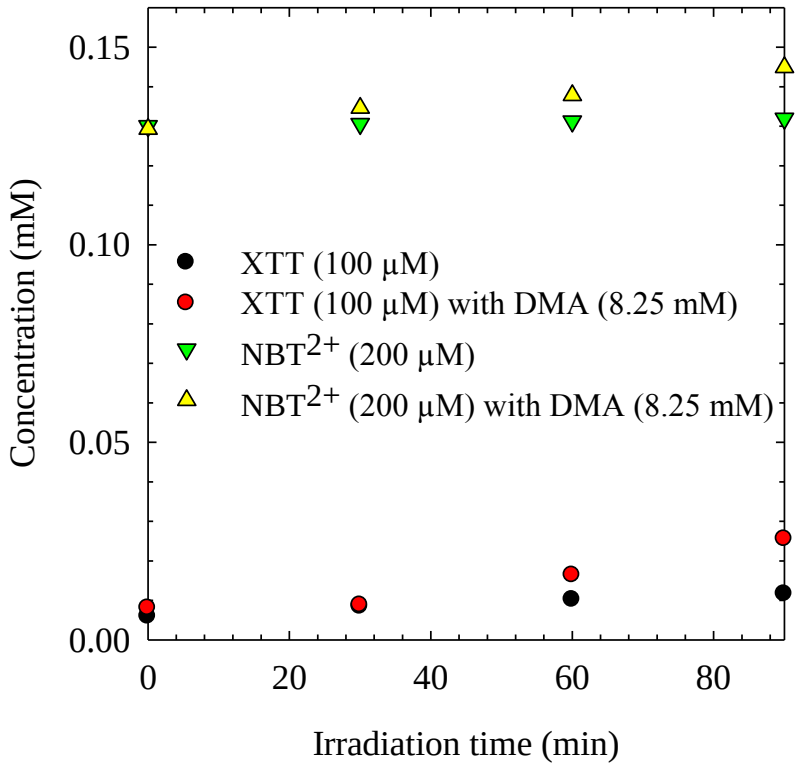

Figure 49: Production of $O_2^{\cdot -}$ as measured by the formation of formazan in the XTT method (observed at 470 nm) and by the formation of monoformazan by the NBT^{2+} method (observed at 530 nm), by 5 μM of **B3** under UVA irradiation.

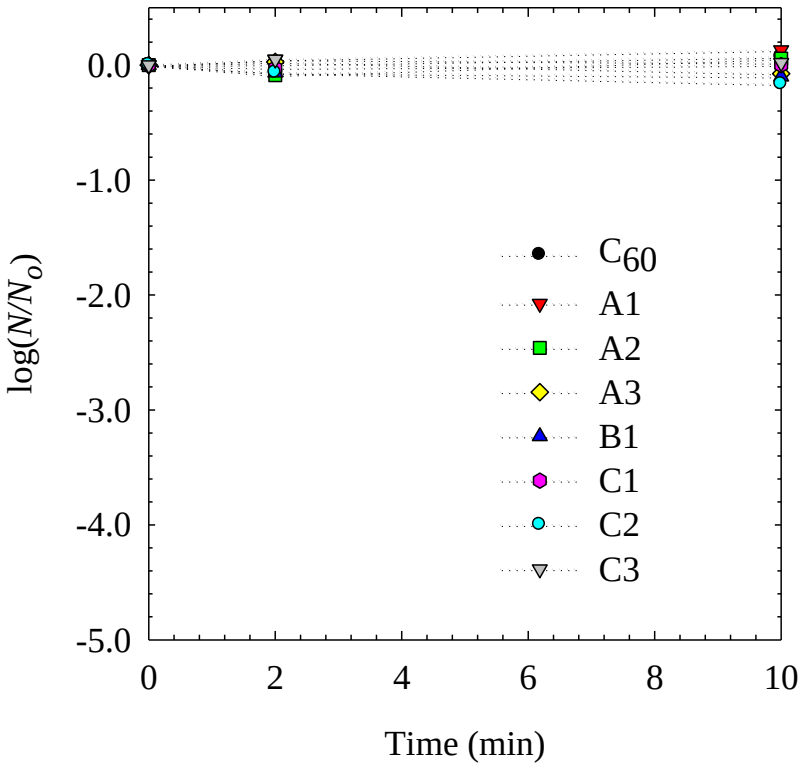

Figure 50: MS2 inactivation by nC_{60}, **A**, **B1**, and **C** derivatives at 5 μM under UVA light.

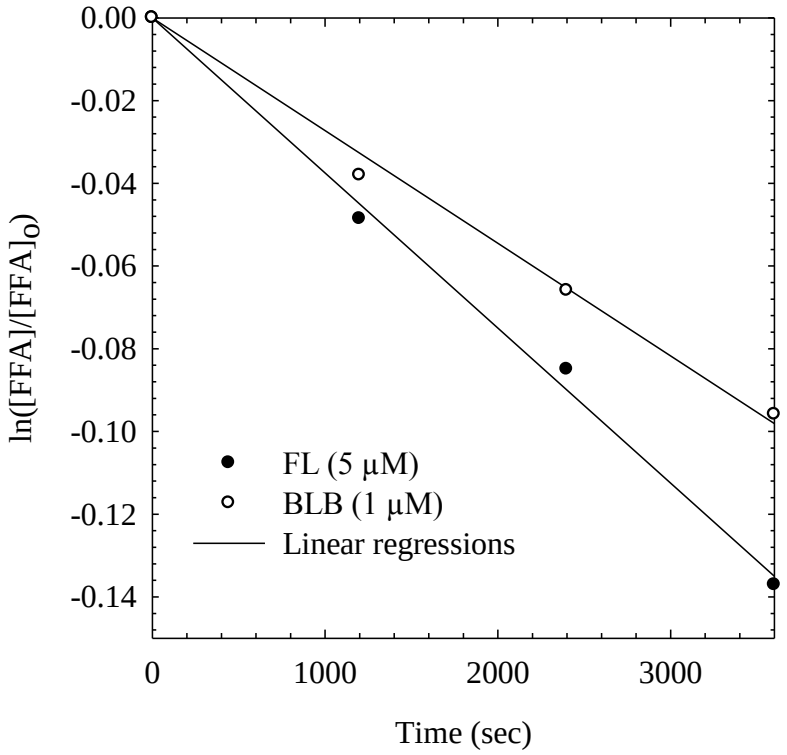

Figure 51: FFA degradation kinetics for **B3** under visible and UVA light at 5 and 1 μM, respectively.

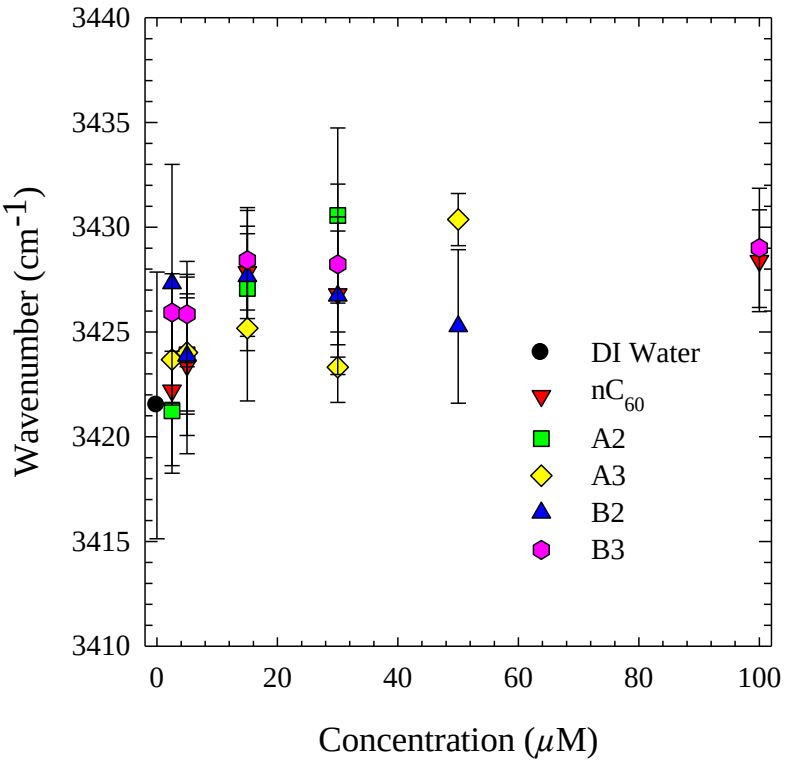

Figure 52: Raman peak locations of the first order O-H symmetric stretching (v_1) for varying concentrations of fullerene aggregates.

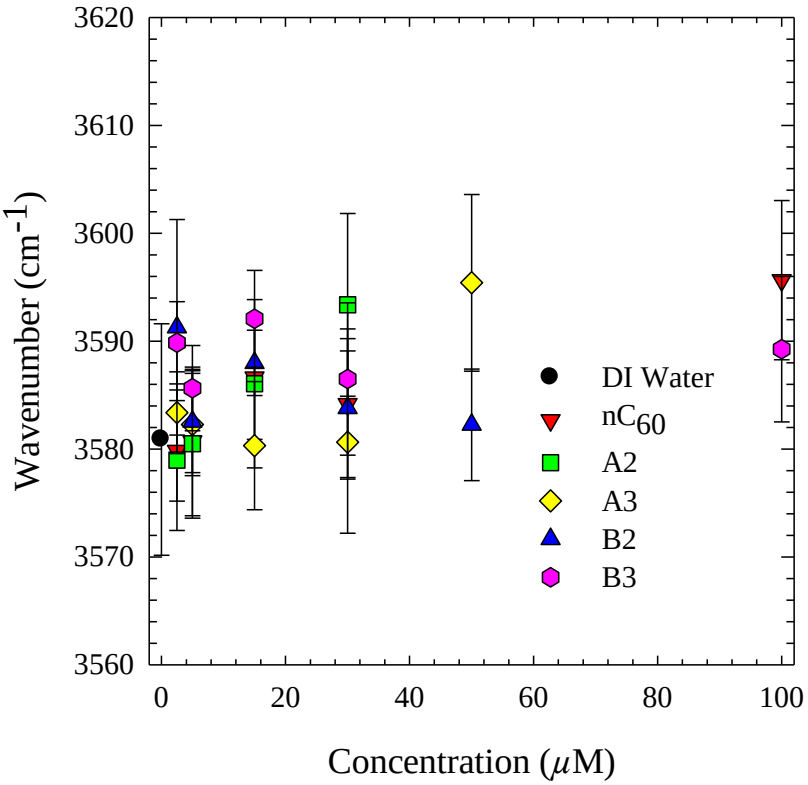

Figure 53: Raman peak locations of the first order O-H asymmetric stretching (ν_3) for varying concentrations of fullerene aggregates.

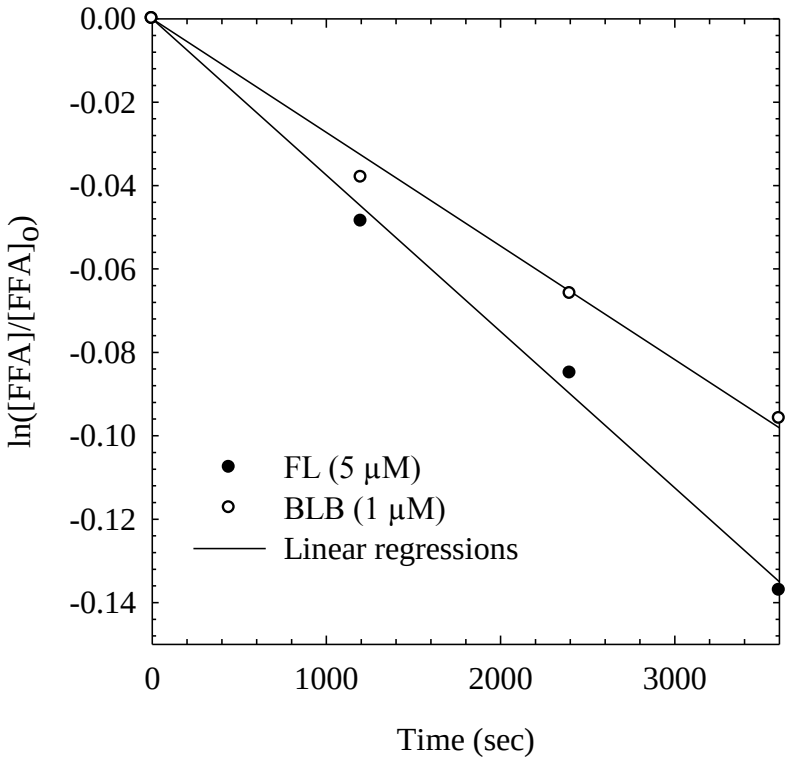

Figure 54: FFA degradation kinetics for **B3** under visible and UVA light at 5 and 1 μM, respectively.

Table 5: Comparative inactivation and sensitization efficiencies of fullerenes.

Type of Sensitizer:	Conc. (μM)	Microbial Agent	Oxidant Yield	Units	Inactivation Rate (k_{obs} min^{-1})	Irradiance (mW/cm^2)	Light Spectrum
Fullerol [138]	40	MS2	0.039	μM/min	0.105	2.89	UVA
Fullerol [138]	40	PRD1	0.039	μM/min	0.026	2.89	UVA
Fullerol [138]	40	T7	0.039	μM/min	0.035	2.89	UVA
nC_{60} [64]	6.944	MS2	0.132	μM/min	0.059	2.3	UVA
$C_{60}(OH)_6$ [64]	6.083	MS2	0.563	μM/min	0.175	2.3	UVA
$C_{60}(OH)_{24}$ [64]	4.433	MS2	0.686	μM/min	0.187	2.3	UVA
$C_{60}(NH_2)_6$ [64]	6.127	MS2	0.969	μM/min	0.389	2.3	UVA
nC_{60} <800 nm [53]	1.389	MS2	18.1	au/s/mg TC	0.00333	2.41	UVA
nC_{60} <450 nm [53]	1.389	MS2	31.5	au/s/mg TC	0.0208	2.41	UVA
nC_{60} <50 nm [53]	1.389	MS2	56.3	au/s/mg TC	0.0645	2.41	UVA
HC4 [43]	15	MS2	0.0074	s^{-1}	0.0408	0.165	Visible
NOM (WSP) [146]	15 (mg/L)	MS2	-	-	0.00333	35.2	320-800 nm
Rose Bengal [148]	0.5	MS2	3.64×10^{-13}	M (ss*)	0.0758	40.0	320-800 nm
B3 (here)	1.0	MS2	0.00229	min^{-1}	4.08	.0380	Visible
B3 (here)	0.0010	MS2	1.60×10^{-6}	min^{-1}	0.036	1.17	UVA

*Steady State

REFERENCES

1. Lee, J.U., et al., *Synthesis and photophysical property of well-defined donor-acceptor diblock copolymer based on regioregular poly(3-hexylthiophene) and fullerene.* Journal of Materials Chemistry, 2009. **19**(10): p. 1483-1489.

2. Mayer, A.C., et al., *Polymer-based solar cells.* Materials Today, 2007. **10**(11): p. 28-33.

3. Sariciftci, N.S., et al., *Semiconducting Polymers (as Donors) and Buckminsterfullerene (as Acceptor) - Photoinduced Electron-Transfer and Heterojunction Devices.* Synthetic Metals, 1993. **59**(3): p. 333-352.

4. Collini, E., et al., *A fullerene-distyrylbenzene photosensitizer for two-photon promoted singlet oxygen production.* Phys Chem Chem Phys, 2010. **12**(18): p. 4656-66.

5. Markovic, Z. and V. Trajkovic, *Biomedical potential of the reactive oxygen species generation and quenching by fullerenes (C_{60}).* Biomaterials, 2008. **29**(26): p. 3561-73.

6. Yu, C., et al., *Efficiency of singlet oxygen production from self-assembled nanospheres of molecular micelle-like photosensitizers FC4S.* Journal of Materials Chemistry, 2005. **15**(18): p. 1857-1864.

7. Kroto, H.W., et al., *C_{60}: Buckminsterfullerene.* Nature, 1985. **318**: p. 162.

8. Arbogast, J.W., et al., *Photophysical Properties of C_{60}.* Journal of Physical Chemistry, 1991. **95**(1): p. 11-12.

9. Ebbesen, T.W., K. Tanigaki, and S. Kuroshima, *Excited-State Properties of C_{60}.* Chemical Physics Letters, 1991. **181**(6): p. 501-504.

10. Dimitrijevic, N.M. and P.V. Kamat, *Triplet Excited-State Behavior of Fullerenes - Pulse-Radiolysis and Laser Flash-Photolysis of C_{60} and C_{70} in Benzene.* Journal of Physical Chemistry, 1992. **96**(12): p. 4811-4814.

11. Kearns, D.R., *Physical and Chemical Properties of Singlet Molecular Oxygen.* Chemical Reviews, 1971. **71**(4): p. 395-&.

12. Wilkinson, F. and J.G. Brummer, *Rate constants for the decay and reactions of the lowest electronically excited singlet-state of molecular-oxygen in solution.* journal of Physical and Chemical Reference Data, 1981. **10**(4): p. 809-1000.

13. Kautsky, H., *Quenching of luminescence by oxygen.* Transactions of the Faraday Society, 1939. **35**(1): p. 0216-0218.

14. Leach, A.G. and K.N. Houk, *Diels-Alder and Ene reactions of singlet oxygen, nitroso compounds and triazolinediones: transition states and mechanisms from contemporary theory.* Chemical Communications, 2002(12): p. 1243-1255.

15. Stephenson, L.M., *Mechanism of the singlet oxygen Ene reaction.* Tetrahedron Letters, 1980. **21**(11): p. 1005-1008.

16. Moura, J.C.V.P., A.M.F. OliveiraCampos, and J. Griffiths, *Synthesis and evaluation of phenothiazine singlet oxygen sensitising dyes for application in cancer phototherapy.* Phosphorus Sulfur and Silicon and the Related Elements, 1997. **120**: p. 459-460.

17. Ogawa, K., et al., *Singlet oxygen generation and photocytotoxicity against tumor cell by two-photon absorption.* Molecular Crystals and Liquid Crystals, 2007. **471**: p. 61-67.

18. Haag, W.R., et al., *Singlet oxygen in surface waters .2. Quantum yields of its production by some natural humic materials as a function of wavelength.* Chemosphere, 1984. **13**(5-6): p. 641-650.

19. Escalada, J.P., et al., *Dye-sensitized photodegradation of the fungicide carbendazim and related benzimidazoles.* Chemosphere, 2006. **65**(2): p. 237-244.

20. Miller, J.S., *Rose bengal-sensitized photooxidation of 2-chlorophenol in water using solar simulated.* Water Research, 2005. **39**(2-3): p. 412-422.

21. Sun, A.H., Z.G. Xiong, and Y.M. Xu, *Removal of malodorous organic sulfides with molecular oxygen and visible light over metal phthalocyanine.* Journal of Hazardous Materials, 2008. **152**(1): p. 191-195.

22. Jimenez-Hernandez, M.E., et al., *Solar water disinfection by singlet oxygen photogenerated with polymer-supported Ru(II) sensitizers.* Solar Energy, 2006. **80**(10): p. 1382-1387.

23. Rengifo-Herrera, J.A., et al., *A comparison of solar photocatalytic inactivation of waterborne E-coli using tris (2,2 '-bipyridine)-ruthenium(II), rose bengal, and TiO_2.* Journal of Solar Energy Engineering-Transactions of the Asme, 2007. **129**(1): p. 135-140.

24. Ogilby, P.R., *Singlet oxygen: there is indeed something new under the sun.* Chemical Society Reviews, 2010. **39**(8): p. 3181-209.

25. Wainwright, M., *Photodynamic antimicrobial chemotherapy (PACT).* J Antimicrob Chemother, 1998. **42**(1): p. 13-28.

26. Ruoff, R.S., et al., *Solubility of C_{60} in a variety of solvents.* Journal of Physical Chemistry, 1993. **97**(13): p. 3379-3383.

27. Deguchi, S., R.G. Alargova, and K. Tsujii, *Stable dispersions of fullerenes, C_{60} and C_{70}, in water. Preparation and characterization.* Langmuir, 2001. **17**(19): p. 6013-6017.

28. Fortner, J.D., et al., *C_{60} in water: Nanocrystal formation and microbial response.* Environmental Science & Technology, 2005. **39**(11): p. 4307-4316.

29. Andersson, T., et al., *C_{60} embedded in r-cyclodextrin - a water-soluble fullerene.* Journal of the Chemical Society-Chemical Communications, 1992(8): p. 604-606.

30. Beeby, A., J. Eastoe, and R.K. Heenan, *Solubilization of C_{60} in aqueous micellar solution.* Journal of the Chemical Society-Chemical Communications, 1994(2): p. 173-175.

31. Yamakoshi, Y.N., et al., *Solubilization of fullerenes into water with polyvinylpyrrolidone applicable to biological tests.* Journal of Chemical Society chemical communications, 1994(4): p. 517-518.

32. Guldi, D.M. and M. Prato, *Excited-state properties of C_{60} fullerene derivatives.* Accounts of Chemical Research, 2000. **33**(10): p. 695-703.

33. Jensen, A.W., S.R. Wilson, and D.I. Schuster, *Biological applications of fullerenes.* Bioorganic & Medicinal Chemistry, 1996. **4**(6): p. 767-779.

34. Hotze, E.M., et al., *Mechanisms of photochemistry and reactive oxygen production by fullerene suspensions in water.* Environmental Science & Technology, 2008. **42**(11): p. 4175-4180.

35. Lee, J., et al., *Photochemical production of reactive oxygen species by C_{60} in the aqueous phase during UV irradiation.* Environmental Science & Technology, 2007. **41**(7): p. 2529-2535.

36. Lee, J., et al., *Mechanism of C_{60} photoreactivity in water: Fate of triplet state and radical anion and production of reactive oxygen species.* Environmental Science & Technology, 2008. **42**(9): p. 3459-3464.

37. Sun, Y.P., et al., *Photophysical and electron-transfer properties of mono- and multiple-functionalized fullerene derivatives.* Journal of Physical Chemistry B, 2000. **104**(19): p. 4625-4632.

38. Prat, F., et al., *Triplet-state properties and singlet oxygen generation in a homologous series of functionalized fullerene derivatives.* Journal of Physical Chemistry A, 1999. **103**(36): p. 7230-7235.

39. Guldi, D.M. and K.D. Asmus, *Photophysical properties of mono- and multiply-functionalized fullerene derivatives.* Journal of Physical Chemistry A, 1997. **101**(8): p. 1472-1481.

40. Hamano, T., et al., *Singlet oxygen production from fullerene derivatives: Effect of sequential functionalization of the fullerene core.* Chemical Communications, 1997(1): p. 21-22.

41. Guldi, D.M. and M. Prato, *Excited-state properties of C_{60} fullerene derivatives.* Accounts of Chemical Research, 2000. **33**(10): p. 695-703.

42. Bosi, S., et al., *Fullerene derivatives: an attractive tool for biological applications.* European journal of medicinal chemistry, 2003. **38**(11-12): p. 913-23.

43. Cho, M., et al., *Visible Light Sensitized Inactivation of MS-2 Bacteriophage by a Cationic Amine-Functionalized C_{60} Derivative.* Environmental Science & Technology, 2010. **44**(17): p. 6685-6691.

44. Gao, J., et al., *Polyhydroxy fullerenes (fullerols or fullerenols): beneficial effects on growth and lifespan in diverse biological models.* Plos One, 2011. **6**(5): p. e19976.

45. Huang, L., et al., *Innovative cationic fullerenes as broad-spectrum light-activated antimicrobials.* Nanomedicine, 2010. **6**(3): p. 442-52.

46. Mroz, P., et al., *Functionalized fullerenes mediate photodynamic killing of cancer cells: Type I versus Type II photochemical mechanism.* Free Radical Biology and Medicine, 2007. **43**(5): p. 711-9.

47. Tegos, G.P., et al., *Cationic fullerenes are effective and selective antimicrobial photosensitizers.* Chem. Biol., 2005. **12**(10): p. 1127-35.

48. Cho, M., et al., *Escherichia coli Inactivation by UVC-Irradiated C_{60}: kinetics and mechanisms.* Environmental Science & Technology, 2011. **45**(22): p. 9627-33.

49. Hou, W.C. and C.T. Jafvert, *Photochemical Transformation of Aqueous C_{60} Clusters in Sunlight.* Environmental Science & Technology, 2009. **43**(2): p. 362-367.

50. Cho, M., et al., *Escherichia coli Inactivation by Water-Soluble, Ozonated C_{60} Derivative: Kinetics and Mechanisms.* Environmental Science & Technology, 2009. **43**(19): p. 7410-7415.

51. Thompson, L.H. and L.K. Doraiswamy, *Sonochemistry: Science and engineering.* Industrial and Engineering Chemistry Research, 1999. **38**(4): p. 1215-1249.

52. Chang, X. and P.J. Vikesland, *UV-vis spectroscopic properties of nC_{60} produced via extended mixing.* Environmental Science & Technology, 2011. **45**(23): p. 9967-74.

53. Chae, S.R., et al., *Heterogeneities in fullerene nanoparticle aggregates affecting reactivity, bioactivity, and transport.* ACS Nano, 2010. **4**(9): p. 5011-8.

54. Fujitsuka, M., et al., *Laser flash photolysis study on photophysical and photochemical properties of C_{60} fine particles.* Journal of Photochemistry and Photobiology a, 2000. **133**(1-2): p. 45-50.

55. Lyon, D.Y., et al., *Antibacterial activity of fullerene water suspensions: effects of preparation method and particle size.* Environmental Science & Technology, 2006. **40**(14): p. 4360-6.

56. Lyon, D.Y., et al., *Bacterial cell association and antimicrobial activity of a C_{60} water suspension.* Environmental Toxicology and Chemistry, 2005. **24**(11): p. 2757-2762.

57. Sayes, C.M., et al., *The differential cytotoxicity of water-soluble fullerenes.* Nano Letters, 2004. **4**(10): p. 1881-1887.

58. Henry, T.B., et al., *Attributing effects of aqueous C_{60} nano-aggregates to tetrahydrofuran decomposition products in larval zebrafish by assessment of gene expression.* Environmental Health Perspectives, 2007. **115**(7): p. 1059-65.

59. Kovochich, M., et al., *Comparative Toxicity of C_{60} Aggregates toward Mammalian Cells: Role of Tetrahydrofuran (THF) Decomposition.* Environmental Science & Technology, 2009. **43**(16): p. 6378-6384.

60. Zhang, B., et al., *Delineating Oxidative Processes of Aqueous C_{60} Preparations: Role of THF Peroxide.* Environmental Science & Technology, 2009. **43**(1): p. 108-113.

61. Trpkovic, A., et al., *Oxidative stress-mediated hemolytic activity of solvent exchange-prepared fullerene (C_{60}) nanoparticles.* Nanotechnology, 2010. **21**(37): p. 375102.

62. Trpkovic, A., B. Todorovic-Markovic, and V. Trajkovic, *Toxicity of pristine versus functionalized fullerenes: mechanisms of cell damage and the role of oxidative stress.* Archives of Toxicology, 2012. **86**(12): p. 1809-27.

63. Snow, S.D., J. Lee, and J.H. Kim, *Photochemical and photophysical properties of sequentially functionalized fullerenes in the aqueous phase.* Environmental Science & Technology, 2012. **46**(24): p. 13227-34.

64. Badireddy, A.R., et al., *Bacteriophage Inactivation by UV-A Illuminated Fullerenes: Role of Nanoparticle-Virus Association and Biological Targets.* Environmental Science & Technology, 2012. **46**(11): p. 5963-5970.

65. Lee, J., et al., *Photochemical and Antimicrobial Properties of Novel C_{60} Derivatives in Aqueous Systems.* Environmental Science & Technology, 2009. **43**(17): p. 6604-6610.

66. Lu, Z.S., et al., *Photodynamic therapy with a cationic functionalized fullerene rescues mice from fatal wound infections.* Nanomedicine, 2010. **5**(10): p. 1525-1533.

67. Mashino, T., et al., *Antibacterial and antiproliferative activity of cationic fullerene derivatives.* Bioorganic & Medicinal Chemistry Letters, 2003. **13**(24): p. 4395-7.

68. Spesia, M.B., M.E. Milanesio, and E.N. Durantini, *Synthesis, properties and photodynamic inactivation of Escherichia coli by novel cationic fullerene C_{60} derivatives.* European Journal of Medicinal Chemistry, 2008. **43**(4): p. 853-61.

69. Burello, E. and A.P. Worth, *QSAR modeling of nanomaterials.* Wiley Interdiscip Rev Nanomed Nanobiotechnol, 2011. **3**(3): p. 298-306.

70. Vanoss, C.J., *Acid-Base Interfacial Interactions in Aqueous-Media.* Colloids and Surfaces a-Physicochemical and Engineering Aspects, 1993. **78**: p. 1-49.

71. Vanoss, C.J., *Long-range and short-range mechanisms of hydrophobic attraction and hydrophilic repulsion in specific and aspecific interactions.* J Mol Recognit, 2003. **16**(4): p. 177-90.

72. Hildebrand, J.H., *Is There a Hydrophobic Effect.* Proceedings of the National Academy of Sciences of the United States of America, 1979. **76**(1): p. 194-194.

73. Chen, K.L. and M. Elimelech, *Relating colloidal stability of fullerene (C_{60}) nanoparticles to nanoparticle charge and electrokinetic properties.* Environmental Science & Technology, 2009. **43**(19): p. 7270-6.

74. Jafvert, C.T. and P.P. Kulkarni, *Buckminsterfullerene's (C_{60}) octanol-water partition coefficient (K_{ow}) and aqueous solubility.* Environmental Science & Technology, 2008. **42**(16): p. 5945-5950.

75. Chae, S.R., et al., *Heterogeneities in Fullerene Nanoparticle Aggregates Affecting Reactivity, Bioactivity, and Transport.* Acs Nano, 2010. **4**(9): p. 5011-5018.

76. Cho, M., et al., *Escherichia coli Inactivation by Water-Soluble, Ozonated C_{60} Derivative: Kinetics and Mechanisms.* Environmental Science & Technology, 2009. **43**(19): p. 7410-7415.

77. Hou, W.C., et al., *Photochemistry of Aqueous C_{60} Clusters: Wavelength Dependency and Product Characterization.* Environmental Science & Technology, 2010. **44**(21): p. 8121-8127.

78. Labille, J., et al., *Hydration and dispersion of C_{60} in aqueous systems: the nature of water-fullerene interactions.* Langmuir, 2009. **25**(19): p. 11232-5.

79. Lee, J., et al., *Transformation of Aggregate C_{60} in the Aqueous Phase by UV Irradiation.* Environmental Science & Technology, 2009. **43**(13): p. 4878-4883.

80. Wang, L., et al., *Contaminant-mobilizing capability of fullerene nanoparticles (nC_{60}): Effect of solvent-exchange process in nC_{60} formation.* Environ Toxicol Chem, 2013. **32**(2): p. 329-36.

81. Wang, C., et al., *(Photo)chlorination-induced physicochemical transformation of aqueous fullerene nC_{60}.* Environmental Science & Technology, 2012. **46**(17): p. 9398-405.

82. Prilutski, Y.I., et al., *Theoretical predictions and experimental studies of self-organized C_{60} nanoparticles in water solution and on the support.* European Physical Journal D, 1999. **9**(1-4): p. 341-343.

83. Scharff, P., et al., *Structure of C_{60} fullerene in water: spectroscopic data.* Carbon, 2004. **42**(5-6): p. 1203-1206.

84. Choudhury, N., *A molecular dynamics simulation study of buckyballs in water: atomistic versus coarse-grained models of C_{60}.* Journal of Chemical Physics, 2006. **125**(3): p. 34502.

85. Choudhury, N., *Dynamics of water in solvation shells and intersolute regions of C_{60}: A molecular dynamics simulation study.* Journal of Physical Chemistry C, 2007. **111**(6): p. 2565-2572.

86. Hotta, T., A. Kimura, and M. Sasai, *Fluctuating hydration structure around nanometer-size hydrophobic solutes. I. Caging and drying around C_{60} and C60H60 spheres.* J Phys Chem B, 2005. **109**(39): p. 18600-8.

87. Ludwig, R. and A. Appelhagen, *Calculation of clathrate-like water clusters including H_2O-buckminsterfullerene.* Angewandte Chemie International Edition, 2005. **44**(5): p. 811-5.

88. Weiss, D.R., T.M. Raschke, and M. Levitt, *How hydrophobic buckminsterfullerene affects surrounding water structure.* The Journal of Physical Chemistry B, 2008. **112**(10): p. 2981-90.

89. Amer, M.S. and W.H. Wang, *Effect of Fullerene Nanospheres on Water Evaporation Kinetics and First-Order Thermal Transitions.* Journal of Physical Chemistry C, 2012. **116**(14): p. 8216-8222.

90. Hüffer, T., et al., *How Redox Conditions and Irradiation Affect Sorption of PAHs by Dispersed Fullerenes (nC_{60}).* Environmental Science & Technology, 2012.

91. Ma, X., B. Wigington, and D. Bouchard, *Fullerene C_{60}: surface energy and interfacial interactions in aqueous systems.* Langmuir, 2010. **26**(14): p. 11886-93.

92. Israelachvili, J. and H. Wennerstrom, *Role of hydration and water structure in biological and colloidal interactions.* Nature, 1996. **379**(6562): p. 219-25.

93. Rand, R.P., et al., *Variation in Hydration Forces between Neutral Phospholipid-Bilayers - Evidence for Hydration Attraction.* Biochemistry, 1988. **27**(20): p. 7711-7722.

94. Shi, L.M., et al., *QSAR models using a large diverse set of estrogens.* Journal of Chemical Information and Computer Sciences, 2001. **41**(1): p. 186-195.

95. Gramatica, P., M. Corradi, and V. Consonni, *Modelling and prediction of soil sorption coefficients of non-ionic organic pesticides by molecular descriptors.* Chemosphere, 2000. **41**(5): p. 763-77.

96. Tratnyek, P.G. and J. Holgne, *Oxidation of Substituted Phenols in the Environment - a Qsar Analysis of Rate Constants for Reaction with Singlet Oxygen.* Environmental Science & Technology, 1991. **25**(9): p. 1596-1604.

97. Cronin, M.T.D. and T.W. Schultz, *Pitfalls in QSAR.* Journal of Molecular Structure-Theochem, 2003. **622**(1-2): p. 39-51.

98. Hannah, W. and P.B. Thompson, *Nanotechnology, risk and the environment: a review.* J Environ Monit, 2008. **10**(3): p. 291-300.

99. Murata, H., et al., *Permanent, non-leaching antibacterial surface--2: how high density cationic surfaces kill bacterial cells.* Biomaterials, 2007. **28**(32): p. 4870-9.

100. Tegos, G.P., et al., *Cationic fullerenes are effective and selective antimicrobial photosensitizers.* Chemistry & Biology, 2005. **12**(10): p. 1127-35.

101. Lee, J., et al., *Photochemical and Antimicrobial Properties of Novel C_{60} Derivatives in Aqueous Systems.* Environmental Science & Technology, 2009. **43**(17): p. 6604-6610.

102. Li, Q., et al., *Antimicrobial nanomaterials for water disinfection and microbial control: potential applications and implications.* Water Res, 2008. **42**(18): p. 4591-602.

103. Zhang, D.Q., G.S. Li, and J.C. Yu, *Inorganic materials for photocatalytic water disinfection.* Journal of Materials Chemistry, 2010. **20**(22): p. 4529-4536.

104. Cattarin, S., et al., *Synthesis and photoelectrochemical properties of a fullerene-azothiophene dyad.* Journal of Materials Chemistry, 1999. **9**(11): p. 2743-2750.

105. Brabec, C.J., N.S. Sariciftci, and J.C. Hummelen, *Plastic Solar Cells.* Advanced Functional Materials, 2001. **11**(1): p. 15-26.

106. Huffman, D.R., *Solid C_{60}.* Physics Today, 1991. **44**(11): p. 22.

107. Harris, G.D., et al., *Potassium Ferrioxalate as Chemical Actinometer in Ultraviolet Reactors.* Journal of Environmental Engineering, 1987. **113**(3): p. 612-627.

108. Jagger, J., *Introduction to research in ultra-violet photobiology*. Prentice-Hall biological techniques series. 1967, Englewood Cliffs, N.J.: Prentice-Hall. 164.

109. Haag, W.R. and J. Hoigne, *Singlet Oxygen in Surface Waters .3. Photochemical Formation and Steady-State Concentrations in Various Types of Waters.* Environmental Science & Technology, 1986. **20**(4): p. 341-348.

110. Zodrow, K., et al., *Polysulfone ultrafiltration membranes impregnated with silver nanoparticles show improved biofouling resistance and virus remova.* Water Research, 2009. **43**: p. 715-723.

111. Lyon, D.Y., et al., *Antibacterial activity of fullerene water suspensions (nC_{60}) is not due to ROS-mediated damage.* Nano Letters, 2008. **8**(5): p. 1539-1543.

112. Lyon, D.Y., et al., *Antibacterial activity of fullerene water suspensions: Effects of preparation method and particle size.* Environmental Science & Technology, 2006. **40**(14): p. 4360-4366.

113. Brunet, L., et al., *Comparative photoactivity of fullerenes and titanium dioxide: mechanisms, implications on antimicrobial activity and applications.* Environmental Science & Technology: p. In press.

114. Cho, M., et al., *Escherichia coli Inactivation by Water Soluble Ozonated C_{60}: Kinetics and Mechanisms.* Environmental Science & Technology: p. In preparation.

115. Maurette, M.T., et al., *Singlet Oxygen and Superoxide - Experimental Differentiation and Analysis.* Helvetica Chimica Acta, 1983. **66**(2): p. 722-733.

116. Moor, K.J. and J.H. Kim, *Simple synthetic method toward solid supported c60 visible light-activated photocatalysts.* Environmental Science & Technology, 2014. **48**(5): p. 2785-91.

117. Sension, R.J., et al., *Ultrafast Photoinduced Electron-Transfer to C_{60}.* Chemical Physics Letters, 1991. **185**(3-4): p. 179-183.

118. Li, L.W., D. Bedrov, and G.D. Smith, *Repulsive solvent-induced interaction between C_{60} fullerenes in water.* Physical Review E, 2005. **71**(1).

119. Bedrov, D., G.D. Smith, and L. Li, *Molecular dynamics simulation study of the role of evenly spaced poly(ethylene oxide) tethers on the aggregation of C_{60} fullerenes in water.* Langmuir, 2005. **21**(12): p. 5251-5.

120. *LAMMPS Molecular Dynamics Simulator*. [cited 2014]; Available from: http://lammps.sandia.gov/.

121. Plimpton, S., *Fast Parallel Algorithms for Short-Range Molecular-Dynamics.* Journal of Computational Physics, 1995. **117**(1): p. 1-19.

122. Mayo, S.L., B.D. Olafson, and W.A. Goddard, *Dreiding - a Generic Force-Field for Molecular Simulations.* Journal of Physical Chemistry, 1990. **94**(26): p. 8897-8909.

123. Kaminski, G.A., et al., *Development of an accurate and robust polarizable molecular mechanics force field from ab initio quantum chemistry.* Journal of Physical Chemistry A, 2004. **108**(4): p. 621-627.

124. Getman, R.B., et al., *Metal Alkoxide Functionalization in Metal-Organic Frameworks for Enhanced Ambient-Temperature Hydrogen Storage.* Journal of Physical Chemistry C, 2011. **115**(5): p. 2066-2075.

125. Yu, D., P. Ghosh, and R.Q. Snurr, *Hierarchical modeling of ammonia adsorption in functionalized metal-organic frameworks.* Dalton Transactions, 2012. **41**(14): p. 3962-73.

126. Perdew, J.P., et al., *Atoms, molecules, solids, and surfaces: Applications of the generalized gradient approximation for exchange and correlation.* Physical Review B, 1992. **46**(11): p. 6671-6687.

127. Kresse, G. and J. Hafner, *Ab initio molecular dynamics for liquid metals.* Physical Review B, 1993. **47**(1): p. 558-561.

128. Kresse, G. and J. Furthmuller, *Efficient iterative schemes for ab initio total-energy calculations using a plane-wave basis set.* Physical Review B, 1996. **54**(16): p. 11169-11186.

129. Vanderbilt, D., *Soft self-consistent pseudopotentials in a generalized eigenvalue formalism.* Physical Review B, 1990. **41**(11): p. 7892-7895.

130. Kresse, G. and D. Joubert, *From ultrasoft pseudopotentials to the projector augmented-wave method.* Physical Review B, 1999. **59**(3): p. 1758-1775.

131. Leach, S., et al., *Electronic-Spectra and Transitions of the Fullerene C_{60}.* Chemical Physics, 1992. **160**(3): p. 451-466.

132. Bensasson, R.V., et al., *C_{60} in Model Biological-Systems - a Visible-Uv Absorption Study of Solvent-Dependent Parameters and Solute Aggregation.* Journal of Physical Chemistry, 1994. **98**(13): p. 3492-3500.

133. Woodward, R.B., *Structure and absorption spectra III Normal conjugated dienes.* Journal of the American Chemical Society, 1942. **64**: p. 72-75.

134. Silverstein, R.M., *Spectrometric Identification of Organic Compounds*. 5th ed. 1991: John Wiley & Sons, Inc.

135. Murdianti, B.S., et al., *C60 oxide as a key component of aqueous C_{60} colloidal suspensions.* Environmental Science & Technology, 2012. **46**(14): p. 7446-53.

136. Rodriguez-Zavala, J.G., et al., *Hydration behaviour of polyhydroxylated fullerenes.* Journal of Physics B-Atomic Molecular and Optical Physics, 2011. **44**(20).

137. Andrievsky, G.V., et al., *Comparative analysis of two aqueous-colloidal solutions of C_{60} fullerene with help of FTIR reflectance and UV-Vis spectroscopy.* Chemical Physics Letters, 2002. **364**(1-2): p. 8-17.

138. Hotze, E.M., et al., *Mechanisms of bacteriophage inactivation via singlet oxygen generation in UV illuminated fullerol suspensions.* Environmental Science & Technology, 2009. **43**(17): p. 6639-45.

139. Hwang, Y.S. and Q. Li, *Characterizing photochemical transformation of aqueous nC_{60} under environmentally relevant conditions.* Environmental Science & Technology, 2010. **44**(8): p. 3008-13.

140. Fortner, J.D., et al., *Reaction of Water-Stable C_{60} aggregates with ozone.* Environmental Science & Technology, 2007. **41**(21): p. 7497-7502.

141. Onoe, J., A. Nakao, and K. Takeuchi, *XPS study of a photopolymerized C_{60} film.* Physical Review B, 1997. **55**(15): p. 10051-10056.

142. Langley, L.A., D.E. Villanueva, and D.H. Fairbrother, *Quantification of surface oxides on carbonaceous materials.* Chemistry of Materials, 2006. **18**(1): p. 169-178.

143. Kratschmer, W., et al., *Solid C_{60} - a New Form of Carbon.* Nature, 1990. **347**(6291): p. 354-358.

144. Innocenzi, P., *Infrared spectroscopy of sol-gel derived silica-based films: a spectra-microstructure overview*. Journal of Non-Crystalline Solids, 2003. **316**(2-3): p. 309-319.

145. Gilbert, P. and L.E. Moore, *Cationic antiseptics: diversity of action under a common epithet.* Journal of Applied Microbiology, 2005. **99**(4): p. 703-15.

146. Kohn, T. and K.L. Nelson, *Sunlight-Mediated Inactivation of MS2 Coliphage via Exogenous Singlet Oxygen Produced by Sensitizers in Natural Waters.* Environmental Science & Technology, 2007. **41**(1): p. 192-197.

147. Kong, L., et al., *Quenching and Sensitizing Fullerene Photoreactions by Natural Organic Matter.* Environmental Science & Technology, 2013. **47**(12): p. 6189-6196.

148. Rosado-Lausell, S.L., et al., *Roles of singlet oxygen and triplet excited state of dissolved organic matter formed by different organic matters in bacteriophage MS2 inactivation.* Water Research, 2013. **47**(14): p. 4869-79.

149. Wilkinson, F., W.P. Helman, and A.B. Ross, *Rate Constants for the Decay and Reactions of the Lowest Electronically Excited Singlet-State of Molecular-Oxygen in Solution - an Expanded and Revised Compilation.* Journal of Physical and Chemical Reference Data, 1995. **24**(2): p. 663-1021.

150. Valegard, K., et al., *The three-dimensional structure of the bacterial virus MS2.* Nature, 1990. **345**(6270): p. 36-41.

151. Davies, M.J., *Singlet oxygen-mediated damage to proteins and its consequences.* Biochemical and Biophysical Research Communications, 2003. **305**(3): p. 761-70.

152. Wang, J., et al., *Long-lifetime and asymmetric singlet oxygen photoluminescence from aqueous fullerene suspensions.* Langmuir, 2013. **29**(29): p. 9051-6.

153. Hotze, E.M., J.Y. Bottero, and M.R. Wiesner, *Theoretical Framework for Nanoparticle Reactivity as a Function of Aggregation State.* Langmuir, 2010. **26**(13): p. 11170-11175.

154. Rice, S., *Conjectures on the structure of amorphous solid and liquid water*, in *Topics in Current Chemistry*. 1975, Springer Berlin Heidelberg. p. 109-200.

155. Deak, J.C., et al., *Vibrational energy relaxation and spectral diffusion in water and deuterated water.* Journal of Physical Chemistry A, 2000. **104**(21): p. 4866-4875.

156. Danilov, O.B., et al., *Generation of singlet oxygen with the use of optically excited fullerenes and fullerene-like nanoparticles.* Optics and Spectroscopy, 2003. **95**(6): p. 833-842.

157. Fukuzumi, S., et al., *Catalytic effects of dioxygen on intramolecular electron transfer in radical ion pairs of zinc porphyrin-linked fullerenes.* Journal of the American Chemical Society, 2001. **123**(11): p. 2571-5.

158. Dolotova, E., et al., *Lifetimes of partial charge transfer exciplexes of 9-cyanophenanthrene and 9-cyanoanthracene.* Chemical Physics Letters, 2003. **380**(5-6): p. 729-735.

159. Schmidt, R., *Photosensitized generation of singlet oxygen.* Photochemistry and Photobiology, 2006. **82**(5): p. 1161-1177.

160. Mcgarvey, D.J., P.G. Szekeres, and F. Wilkinson, *The Efficiency of Singlet Oxygen Generation by Substituted Naphthalenes in Benzene - Evidence for the Participation of Charge-Transfer Interactions.* Chemical Physics Letters, 1992. **199**(3-4): p. 314-319.

161. Wilkinson, F. and A.A. AbdelShafi, *Mechanism of quenching of triplet states by oxygen: Biphenyl derivatives in acetonitrile.* Journal of Physical Chemistry A, 1997. **101**(30): p. 5509-5516.

162. Abdel-Shafi, A.A. and F. Wilkinson, *Charge transfer effects on the efficiency of singlet oxygen production following oxygen quenching of excited singlet and triplet states of aromatic hydrocarbons in acetonitrile.* Journal of Physical Chemistry A, 2000. **104**(24): p. 5747-5757.

163. Abdel-Shafi, A.A. and F. Wilkinson, *Electronic to vibrational energy conversion and charge transfer contributions during quenching by molecular oxygen of electronically excited triplet states.* Physical Chemistry Chemical Physics, 2002. **4**(2): p. 248-254.

164. Schmidt, R., *The effect of solvent polarity on the balance between charge transfer and non-charge transfer pathways in the sensitization of singlet oxygen by pipi triplet states.* Journal of physical chemistry A, 2006. **110**(18): p. 5990-7.

165. Wilkinson, F., D.J. Mcgarvey, and A.F. Olea, *Factors Governing the Efficiency of Singlet Oxygen Production during Oxygen Quenching of Singlet and Triplet-States of Anthracene-Derivatives in Cyclohexane Solution.* Journal of the American Chemical Society, 1993. **115**(25): p. 12144-12151.

166. Schweitzer, C., et al., *Mechanism of photosensitized generation of singlet oxygen during oxygen quenching of triplet states and the general dependence of the rate constants and efficiencies of O_2((1)Sigma(+)(g)), O_2((1)Delta(g)), and O_2((3)Sigma(-)(g)) formation on sensitizer triplet state energy and oxidation potential.* Journal of Physical Chemistry A, 2003. **107**(13): p. 2192-2198.

167. Mehrdad, Z., et al., *Sensitization of singlet oxygen via encounter complexes and via exciplexes of pi pi* triplet excited sensitizers and oxygen.* Photochemical & Photobiological Sciences, 2002. **1**(4): p. 263-269.